Theoretical study of the many-body electronic states of defects in diamond : the case of the NV center under high pressure

Mariya Romanova

INSTITUT POLYTECHNIQUE DE PARIS

NNT : 2019IPPAX013

Thèse de doctorat

ÉCOLE POLYTECHNIQUE

IP PARIS

Theoretical study of the many-body electronic states of defects in diamond: the case of the NV center under high pressure

Thèse de doctorat de l'Institut Polytechnique de Paris
préparée à l'Ecole polytechnique

École doctorale n°ED 626 de l'Institut Polytechnique de Paris (ED IP Paris)
Spécialité de doctorat: Physique

Thèse présentée et soutenue à Palaiseau, le 17.10.2019, par

MARIYA ROMANOVA

Composition du Jury :

Jean-François Roch Professeur, ENS Paris-Saclay (Laboratoire Aimé Cotton)	Président
Chris Van de Walle Professeur, Université de California Santa Barbara (Materials Department)	Rapporteur
Vincent Robert Professeur, Université de Strasbourg (Laboratoire de Chimie Quantique)	Rapporteur
Anaïs Dréau Chargé de recherche, CNRS, Université Montpellier (Laboratoire Charles Coulomb)	Examinateur
Michele Casula Chargé de recherche, CNRS, Sorbonne Université (Institut de Minéralogie, de Physique des Matériaux et de Cosmochimie (IMPMC)	Examinateur
Nathalie Vast Chargé de recherche, Ecole Polytechnique, CEA/DRF/IRAMIS, CNRS UMR 7642, Institut Polytechnique de Paris (Laboratoire des Solides Irradiés)	Directeur de thèse
Jelena Sjakste Chargé de recherche, Ecole Polytechnique, CEA/DRF/IRAMIS, CNRS UMR 7642, Institut Polytechnique de Paris (Laboratoire des Solides Irradiés)	Co-directeur de thèse

Acknowledgements

I would like to express my gratitude at first place to my supervisors Nathalie Vast and Jelena Sjakste for have believed in me and for have designed for me the present project, for their guidance and patience.

I am very grateful to all members of the Jury and especially to reviewers Chris Van de Walle and Vincent Robert for have accepted to read the present manuscript, for their valuable comments and suggestions for the improvement of the present manuscript.

I would like to thank my collaborators for have enriched this project. I would like to thank Jean-François Roch, Vincent Vindolet, Margarita Lesik, Thomas Plisson for the numerous appealing discussions about experimental details of the magnetic sensing with the NV center under high pressure. I would like to thank Michele Casula for the fruitful discussions about the Hubbard model and the DFT calculations. I am grateful to Jean-Jacques Girerd for introducing me to a quantum chemistry point of view on the molecular model of the NV center.

I would like to acknowledge the efforts of the administration of the Laboratoire des Solides Irradiés for assisting me in every administrative aspect and for being always there for me.

Last but not least, I would like to thank all members of the TSM group for our daily interactions, discussions and a friendly environment that you have created during my PhD: Oleksandr Motornyi, Giuliana Barbarino, Amrita Chakraborti, Romuald Bejaud, Maksim Markov and Olivier Hadrouin Duparc. Finally, I would like to thank every person at the Laboratoire des Solides Irradiés.

Résumé

Ce travail de doctorat a pour objet l'étude, dans le diamant, de l'influence de la pression sur les transitions optiques entres l'état fondamental et les états excités du centre « azote-lacune de carbone » NV, sans paramètre ajustable. Le centre neutre NV^0 et le centre chargé négativement NV^- ont chacun été étudiés. L'étude a nécessité le développement d'un modèle de Hubbard où les valeurs des interactions sont obtenues sans ajustement sur l'expérience, par une méthode de calcul à partir des principes premiers.

Le centre NV est un défaut à niveaux profonds, ses propriétés optiques et magnétiques sont liées aux niveaux sans dispersion dans la bande interdite électronique associés à des états électroniques fortement localisés. Ces niveaux proviennent de combinaisons linéaires d'orbitales localisées correspondant aux quatre liaisons pendantes pointant vers le centre de la lacune et issues des corrélations électroniques fortes. C'est pourquoi un traitement rigoureux, à l'échelle quantique, est nécessaire. La DFT est une approche puissante pour les calculs des propriétés de l'état fondamental des défauts ponctuels. Cependant, les états électroniques en DFT ont un caractère mono-déterminantal : un seul déterminant de Slater intervient, auquel il manque les corrélations non dynamiques. La DFT seule ne permet pas de calculer certains états électroniques à N- corps qui caractérisent les défauts profonds. De plus, les fonctionnelles d'échange et corrélation (FXC) utilisées en DFT ont une précision limitée.

C'est pourquoi j'ai d'abord développé une approche combinée modèle d'Hubbard + DFT. La transition triplet-triplet entre l'état fondamental et le premier état triplet excité est étudié à la fois avec la FXC standard GGA-PBE, et la FXC hybride HSE06. Il est montré que l'utilisation de cette dernière améliore la description des corrélations au-delà de la DFT-PBE, et permet la prédiction des transitions optiques plus précise. De plus, les interactions à longue portée ont un effet crucial dans la modélisation des défauts profonds: premièrement, les déformations élastiques, dues à la présence d'un atome de nature différente (N) de ceux de la matrice (C), sont à longue portée et doivent être prises en compte; ensuite, quand le défaut est chargé, il est important d'éviter l'interaction non-physique charge-charge entre supermailles voisines, causée par l'utilisation des conditions périodiques aux limites. Par conséquent, j'ai étudié la structure atomique d'un défaut dans de grandes supermailles. La diagonalisation exacte soit, en termes de chimie quantique, le calcul d'interaction de configurations, du Hamiltonian de Hubbard dans la base à plusieurs électrons, construite à partir des niveaux localisé dans la bande interdite, permet d'accéder aux états fondamental et excités multi-configurationels. Cette technique a été comparée aux méthodes récentes de l'état de l'art.

La méthode développée est appliquée à l'étude de l'effet de la pression hydrostatique sur les niveaux triplets et singulets du centre NV^-, et sur les niveaux doublets et quadruplets du centre NV^0. Parmi les nombreux résultats, j'ai découvert un effet très intéressant lié à la

transition singulet-singulet sous pression hydrostatique dans le centre NV^-. Les résultats obtenus dans ce travail n'ont jamais été ni calculé ni mesurés expérimentalement.

En perspective, j'ai développé un nouveau code de calcul qui peut être utilisé pour étudier d'autres défauts d'interêt dans les technologies quantiques.

Mots clefs : Défauts ponctuels; Diamant; centre NV; Théorie de la fonctionnelle de la densité; Théorie des groups; Modèle d'Hubbard; Magnétometrie; Pression hydrostatique;

Abstract

The aim of this doctoral thesis is to study the influence of the pressure on the optical transitions between multi-determinant ground state and excited states of the NV center from the first-principles.

In this work, I study both the neutral NV^0 and negatively charged NV^- centers. This study needed the development of the Hubbard model where the interaction parameters were not fitted to the experiment but were calculated from the first-principles.

The NV center is a deep-center defect, its optical and magnetic properties are related with localized levels in the electronic band-gap. These levels are believed to be built out of the localized orbitals of dangling bonds pointing towards the vacancy, providing strongly correlated electronic states. Thus, an accurate quantum mechanical treatment is needed. DFT is a powerful approach for the calculation of the ground state properties of defects. However, the single Slater determinant nature of the DFT wave function lacks the non-dynamical correlations, that characterize such defects, and does not allow for the calculation of many-body levels. Moreover, exchange and correlation (XC) functionals used in DFT add have a limited accuracy.

Therefore, in this PhD work, I first develop a combined DFT + Hubbard model technique. I study the triplet-triplet transition both with the PBE XC functional and the HSE06 one. I confirm that the use of the hybrid XC functional HSE06 improves the description of correlations beyond DFT-PBE and allows for more accurate prediction of optical transitions. Long-range interactions have a crucial effect in such defects: first, elastic deformations have a long range and need to be accounted for; second, when the defect has a charge, it is important to avoid spurious charge-charge interactions between neighboring supercells caused by the use of periodic boundary conditions. Thus, I study the atomic structure of defect with large supercells by the density functional theory (DFT).

An exact diagonalization (or in quantum chemistry language full Configuration Interaction calculations) of the Hubbard Hamiltonian in the many-electron basis constructed of in-gap localized levels, allows to get access to multi-determinant ground and excited states. I benchmark this technique comparing it to the recent state of the art methods.

Finally, I apply the developed technique in order to study the effect of the hydrostatic pressure on NV^- and NV^0 centers. Among many results of my work, I discovered a very interesting effect related to the singlet-singlet transition in the NV^- center under hydrostatic pressure.

As a perspective, I developed a new code that can be applied to study other defect systems of interest in the quantum technologies.

Key words: Point defects; Diamond; NV center; Density Functional Theory; Hubbard

model; Group Theory; Magnetometry; Hydrostatic pressure;

Contents

CHAPTER 1

Introduction

The subject of deep center defects in semiconductors and insulators is of special interest in the area of quantum technologies and a challenging topic. The typical example of a deep-center defect is the nitrogen-vacancy (NV) center in diamond. Isolated defect-related electronic levels are localized in the bandgap of the insulator. Photoexcited transitions between these levels produce a photoluminescence which, for the NV center in diamond is perfectly stable even at room temperature. Thus this quantum system can be used as an efficient and practical single-photon source for quantum cryptography applications [1, 2]. Also, the spin states of this defect possess a long spin coherence time and can be optically manipulated at room temperature, which makes them attractive candidates for quantum computer applications [3–7]. Moreover, the NV center interacts with an external magnetic field in a way similar to that of a real atom, in the sense that the Zeeman coupling of this atom-like system can be used to measure the projection of the magnetic field along the intrinsic quantization axis that is defined by the NV pair direction [8–11].

In addition, of concern in the present work, the atomic size of the NV center and the long coherence time of its electron spin at room temperature provide a unique combination of sensitivity and spatial resolution compared to other magnetometry techniques: a single NV center can detect a magnetic field in the mT range with a μT uncertainty and a nm resolution [12]. During the past years, this property was applied to image magnetic thin films and to determine their magnetization texture [13, 14]. As described in the first part of the present manuscript, this property has a special interest when used under extreme conditions. Indeed, high pressure applied in a solid may generate metallic and superconducting states in insulators or semiconductors because of the closure of the electronic band gap, and the detection of the superconducting states requires magnetometry in order to detect the Meissner effect.

In more details, pressures above 100 GPa are routinely obtained in diamond cells (DAC) but the tiny sample volume is almost incompatible with any non-optical detection scheme. Thus, the use of NV diamond color centers as *in-situ* magnetic sensors integrated in the DAC can enable scientists to address in table-top experiments open questions such as the close-to-room temperature superconductivity of hydride compounds, or the exploration of complex quantum phase diagrams when magnetic materials are pushed to high pressures. This is the expertise of the Jean-François Roch's experimental group with which I have been discussing during the PhD work, in particular with Baptiste Vindolet and Margarita Lesik, Laboratoire Aimé Cotton, ENS Paris-Saclay, Université Paris-Sud, and in collaboration with Paul Loubeyre's group, particularly with Thomas Plisson, CEA-DAM, Bruyères-le-

Châtel. A very recent advance of my collaborators in this technique allowed to see the Meissner effect associated to the superconductivity of MgB_2 at 7 GPa [15]. An application of this technique at pressures higher than 7 GPa, however, demands an attentive study of the behavior of the NV center itself at such pressures and I point out that a better understanding of the behavior of the many-body states of the NV center under pressure is important in order to learn the sources of the limitations of the NV center application as a magnetic sensor at high pressures. Despite some recent studies of the behavior of the NV center under pressure [16–18] some effects are still not understood, which has motivated the present theoretical work. In fact, to face the challenge of probing the magnetic field at ultra-high pressure, I aim of predicting the spectroscopic properties of the NV center at very high pressure. This implies the calculation of the manifold of the low-lying many-body states of the NV center. This also rises the question of electronic correlations, their behavior under pressure, and their treatment with theoretical methods. Indeed, the many-body states of the NV center arise from combinations of occupations of the localized defect dangling bonds, and thus are strongly correlated states that have a multi-determinant nature. Thus, their evaluation requires an accurate quantum mechanical treatment.

The complexity of the present work is twofold. The first challenge is related to the requirement of the development and utilization of the advanced methods to treat the strongly correlated states. The second one, is related to the requirement of a balanced compromise between the use of a method of moderate computational cost and the accuracy to treat the electronic correlations. In fact, the theoretical treatment of defects in solids with periodic boundary conditions, in general, requires the use of supercell techniques. This allows to reduce the spurious interactions in neigboring supercells caused by the long-range interactions, such as the elastic deformation induced by the presence of the defect and the charge-charge interactions in the case of a charged defect like NV^-. However, the supercell method is computationally cumbersome.

Moreover, today, there is no method that is able to simultaneously provide an accurate description of the weak and strong correlations at low computational cost. Therefore, in the present work I develop and use a combination of the density functional method (DFT) with the Hubbard model. The work is performed in the Materials Science Theory group, in the Laboratoire Solides Irradiés, and this allowed me to benefit of the expertise on DFT-based methods on the treatment of point defects in boron carbide and electron-phonon coupling. The theoretical development was also done in collaboration with Michele Casula, IMPMC, Sorbonne Unversité, and this collaboration gave rise to fruitful discussions.

More specifically, I aim at understanding the influence of pressure on the vertical transition and zero phonon line between the two triplet states and between two singlet states of the NV center, that have been observed experimentally and are being used for magnetometry. As I will show, the hydrostatic pressure behavior of the triplet-triplet transition has been well established both experimentally and theoretically, and I will use this fact to validate my method. Moreover, very little is known about the singlet-singlet transition under pressure. Finally, I will also study the NV^0 center for which even the ordering of the many-body states is uncertain and for which there is a lack of the advanced theoretical studies about the influence of the pressure.

The outline of the manuscript reads as follows. In chapter 2 and chapter 3, I will provide the background knowledge on the NV center physics including its properties and applications to the magnetic sensing.

The chapter 4 contains a careful discussion on the treatment of electronic correlations in different methods, as well as a review of the recent advances of theoretical methods in application to the NV center. Finally, I will define the method that I will use in the present work.

The part II is devoted to the results I have obtained during my PhD. In chapter 5, I will present the results of the DFT calculations for the mono-determinant states of the NV center. I will conclude on the validity of the DFT calculations for their use as references for the Hubard model.

In chapter 6, I will introduce two Hubbard models and the code developed in the present work. I will apply the 3-site and 4-site models to the negatively charged NV^- center and neutral NV^0 center at ambient pressure. I will benchmark my models by comparing my results with the experimental data and the previous theoretical works.

Finally, in chapter 7, I will present my results of the pressure effect on the many-body states of the NV^- and of the NV^0 centers. One of the main outcomes of my results concerns the behavior of the singlet-singlet transition, which to the best of my knowledge has never been measured nor calculated before.

Finally, in chapter 8 I will draw conclusions and will discuss some perspective and possible extentions of my model. The appendix 8 contains the details of the development of the pseudopotential that have been used in the present work.

This work has required intensive computations in a high performance computing evironment with the Quantum ESPRESSO package and I would like to acknowledge the computing time provided by the local LLR-LSI cluster (92 000 CPU hours has been spent during my PhD), the computing time provided by French national centers GENCI-CINES (1 710 742 CPU hours), GENCI-TGCC (238 745 CPU hours) and GENCI-IDRIS (120 279 CPU hours), also the computing time provided by PRACE project on JUWELS machine.

This work has been supported by the LabEx PALM, by the Paris Île-de-France Région in the framework of DIM SIRTEQ, and by the 3-year fellowship of the Interfaces Doctoral School which has started in October 2016.

Part I

State of the art

CHAPTER 2

Physics of NV^- center in diamond

The nitrogen-vacancy NV center defect in diamond is considered nowadays as the most studied deep-center defect [19–22]. The discovery of the NV center has taken a long time from the first classification of the two types of diamond in 1934 [23] till 25 years later the connection has been established between the spectroscopic properties of the type I of diamond and the concentration of nitrogen atoms [24]. And finally, in 1965 the formation of the NV^- optical band has been observed after the radiation damage and annealing by du Preez [25]. The NV has been a system of interest in the scientific community for decades since then and gained even more interest when the fluorescence of the individual NV center defect has been detected [26]. This played a crucial role in the emergence of the new quantum technologies. Even though many of the NV center properties have been understood, some of them are still the object of debates and are still unexplained. In this chapter we will discuss the properties of the NV center that are the most relevant for the understanding of this manuscript.

2.1 The NV^- center

2.1.1 Defect structure

The NV center is a point defect in diamond that consists of a nitrogen atom in substitution of a carbon atom and located next to a carbon vacancy, the pair axis being oriented along the [111] crystal direction. In 1965 du Preez [25] has observed the formation of an optical band in in diamond after the radiation damage and annealing of the sample. He proposed that the optical band is related to the nitrogen-vacancy pairs. He explained the formation of a pair as follows: diamond naturally contains nitrogen and the radiation creates vacant sites which become mobile under the annealing and can be trapped by nitrogen impurities. Later, the structure of the NV center, its trigonal symmetry C_{3v} and the A- to -E character of the optical transition were supported by studies of the polarization of the photoluminescence in ref. [27] and by the study of the uniaxial stress in ref. [28]. Further studies of the electron paramagnetic resonance (EPR) in 1982 [29] allowed to identify the spin multiplicity of the ground state as a triplet ^3A, consequently a negative charge has been attributed to the NV^- center and this attribution was supported by a molecular model. According to the molecular model, the NV^- center defect contributes to the electronic structure of the diamond with the localized molecular orbitals $a_1^N a_1 e_x e_y$, formed of the carbon dangling bonds σ_i and nitrogen lone pair σ_4 pointing towards the

vacant site as depicted in Fig. 2.1.1. The molecular orbitals are occupied by 6 electrons: 5 electrons are given by the dangling bonds and 1 electron is trapped from the neighboring donor.

The described model is so called 4-site model which will be the basis of one of the two Hubbard models studied in the present work. I will show later that an even simpler 3-site model can be defined in order to describe the optical properties of the NV center. In the 3-site model, the nitrogen atom will be included in the screening environment and not directly in the molecular model. In that case molecular orbitals will consist of $a_1 e_x e_y$ with a screening modified by a_1^N.

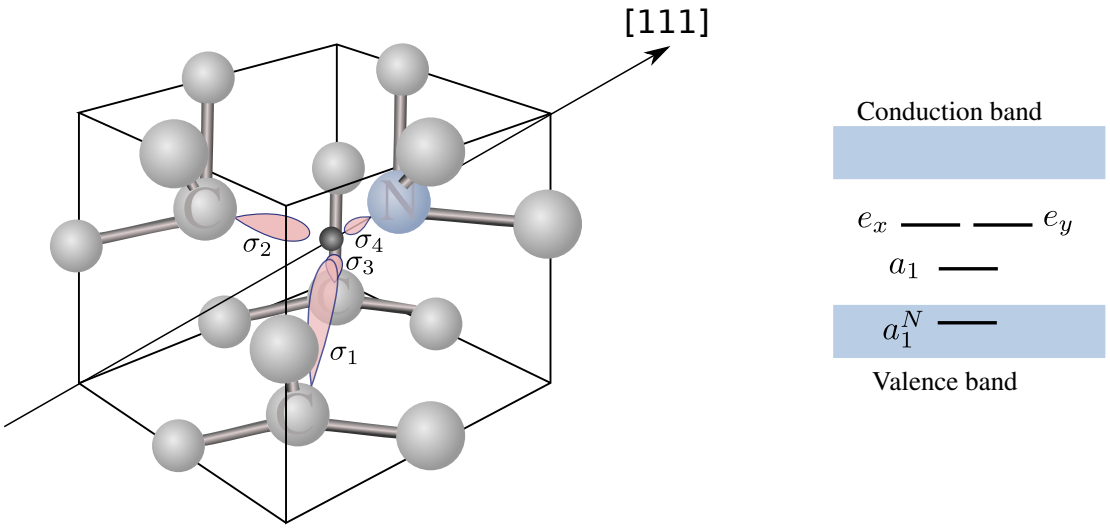

Figure 2.1.1: 4-site model. (a) Schematic representation of the dangling bonds pointing towards the vacancy. Figure is adapted from ref. [22]. (b) Schematic representation of the molecular defect orbitals in the band gap of diamond. Figure is adapted from ref. [30]

2.1.2 Electronic structure

The electronic excitations between the molecular orbitals of the NV center defect $a_1^N a_1 e_x e_y$ create a structure of many-body excited states. The currently accepted electronic structure of the many-body states is shown in Fig. 2.1.2. It consists of the triplet $^3A_2$ ground state with the molecular orbitals configuration $a_1^N(2)a_1(2)e(2)$. Optically excited triplet ^3E state can be obtained by promoting one electron from the a_1 orbital to the e degenerate orbital, resulting in the $a_1^N(2)a_1(1)e(3)$ configuration.

There are also two singlet excited states between the two triplet states []. They arise from configuration interaction of the molecular occupations $a_1^N(2)a_1(2)e(2)$. There were many contentions concerning the ordering of the singlet states. Also, in the early model

of the electronic structure of the NV^- center, the existence of only one $^1A_1$ singlet has often been considered [31, 32]. According to the currently accepted model the ^1E state is lower than the $^1A_1$ state [33]. These highly correlated electronic states play a crucial role in the optical dynamics of the NV^- center. It is also important to mention that the relative positions of the triplet ground state with respect to the first excited singlet $^3A \leftrightarrow^1 E$ and first excited triplet with respect to the second excited singlet $^3E \leftrightarrow^1 A_1$ are unknown experimentally. The state of the art theoretical works predict that the $^3E \leftrightarrow^1 A_1$ transition energy is around 0.4 eV and the $^3A \leftrightarrow^1 E$ one is also around 0.4 eV [22, 34, 35].

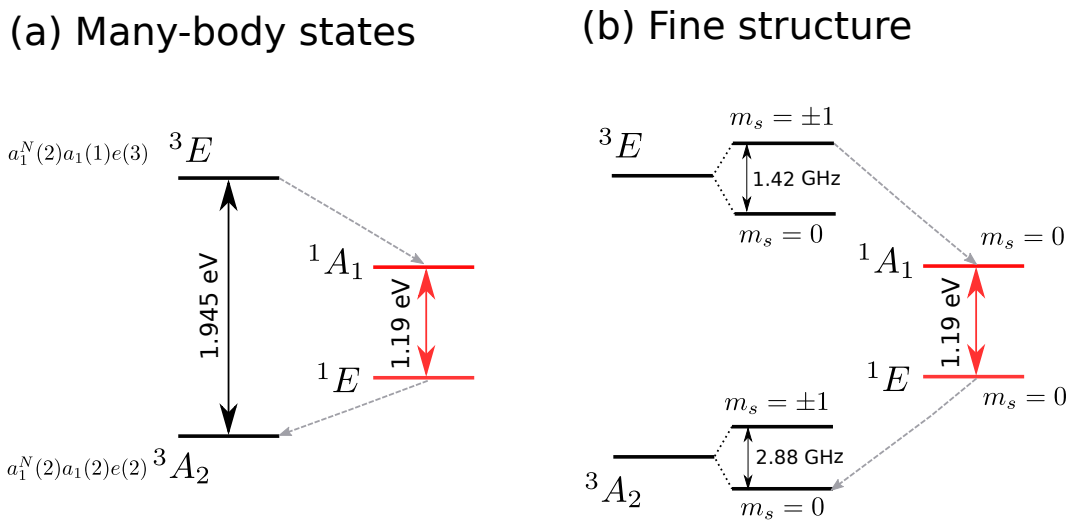

Figure 2.1.2: NV^- center. (a) Schematic representation of the electronic structure of the many-body states. (b) Schematic representation of the electronic fine structure at room temperature. Figures are adapted from ref. [20]

2.1.3 Fine structure

We briefly remind the definitions of quantities entering the spin Hamiltonian in order to discuss the fine structure of the NV center.

a. Orbital angular moment

The orbital angular momentum $\hat{L}$ is a relativistic effect due to the relative motion between electron and nuclei and is at the origin of the orbital magnetic momentum $\hat{\mu}_l = g_l \mu_B \hat{L}$. Where g_l=1 is a Landé factor, μ_B Bohr magneton - a basic unit of atomic magnetism.

b. Spin angular moment

The spin angular momentum $\hat{S}$ of an electron is at the origin of the spin magnetic momentum $\hat{\mu}_s = g_s \mu_B \hat{S}$, where Landé factor g_s=2.

c. Spin-orbit coupling

The internal spin-orbit coupling is the magnetic coupling of the electron spin $\hat{S}$ to the orbital magnetic moment $\hat{L}$. The contribution of the spin-orbit coupling to the spin Hamiltonian is $H_{SO} = \lambda \hat{L}\hat{S}$.

d. Spin-spin coupling

The magnetic coupling of the electron spin moment μ_1 to the magnetic moment of another electron spin, μ_2 is called the spin-spin dipolar interaction and its contribution to the spin Hamiltonian is $H_{SS} = \frac{\mu_0}{4\pi r^3}(\hat{\mu}_1\hat{\mu}_2 - \frac{3}{r^2}(\hat{\mu}_1\hat{r})(\hat{\mu}_2\hat{r}))$, with μ_0 - magnetic permeability.

e. Fine structure of the ground state (GS)

In the NV center ground state the spin-spin Hamiltonian results in $H_{SS} = D_{gs}(\hat{S}_z^2 - S(S+1)/3)$. Thus, due to the dipolar interaction between spins, there is a splitting D_{gs} between the $m_s = 0$ and the $m_s = \pm 1$ states of the triplet $^3A_2$ ground state at zero magnetic field (Fig. 2.1.2 (b)). This splitting is called the zero-field splitting. The fine structure of the $^3A_2$ ground state is represented only by the zero-field splitting because the spin-orbit interaction in weak in the ground state [20]. The zero-field splitting constant D_{gs} is of the value 2.88 GHz, it has been observed very early in ref. in the ground state [29] in 1982.

f. Fine structure of the excited state (ES)

The fine structure of the first excite ^3E state depends on temperature [20]. Thus, we discuss both low temperature and room temperature cases.

f1. Low temperature

In contrast to the ground state, for the first excited triplet ^3E it is only until ref.[36] in 2009 that the fine structure has been directly observed at low temperature and the D_{es} constant has been attributed to a value of 1.42 GHz [36]. The complexity of the direct observation of the fine structure of the ^3E state was due to the mixing of the spin sublevels in the lower fine structure branch E_y by the local strain (Fig. 2.1.3) at the low temperature. This mixing ensured that the lower branch did not have adequate fluorescence to be visible without the application of microwave radiation. In ref. [36], the optical excitation at low temperature was combined with a microwave excitation tuned to the ground state magnetic resonance. That induced an increase of the fluorescence of the lower branch fine structure levels for them to be observed. Also, in ref. [36], the effect of the strain on ^3E state was studied (Fig. 2.1.3 (b)). They have found that at some specific strains, identified by circles in Fig. 2.1.3 (b), the additional optical spin-flip transitions occur. The first area surrounded by circle corresponds to the case where the spin mixing induced by the local strain provoke avoiding crossing. In the second area at higher strain the spin sublevels are crossing. Due

to these investigations it was found that the ^3E level's fine structure is more complicated than the one of the $^3A_2$ as depicted in Fig. 2.1.3.

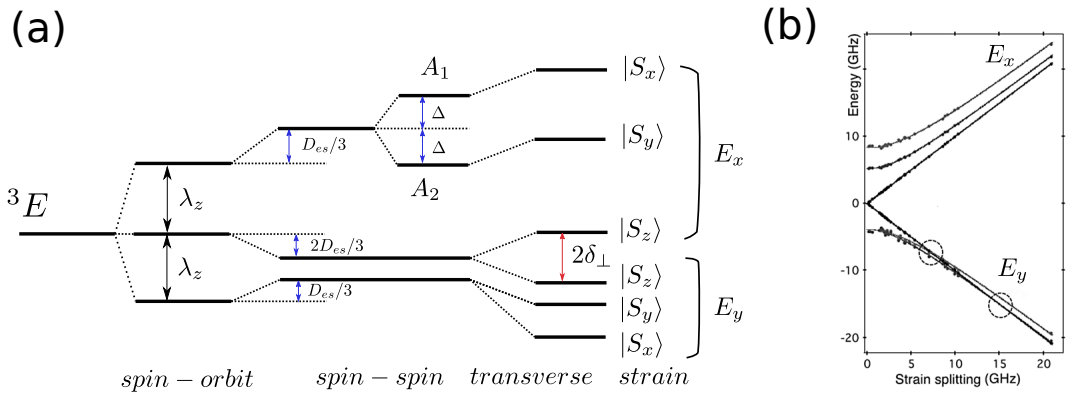

Figure 2.1.3: ^3E state of the NV^- center. (a) Schematic representation of the electronic fine structure at low temperature. Figure is adapted from ref. [33] (b) Fine structure observed at low temperature (4 K) as a function of transverse strain $\delta_\perp$ [36]. Figure is taken from [20]

Indeed, the fine structure of the ^3E state at low temperature affected both by the spin-orbit and spin-spin interactions. The Hamiltonian of the ^3E excited state can be written as $H = H_{SO} + H_{SS} + H_{str}$, where H_{SO} is a spin-orbit coupling presented by its diagonal component $\lambda_z \hat{L}_z \hat{S}_z$, because the transverse component $\lambda_{x,y}(\hat{L}_x \hat{S}_x + \hat{L}_y \hat{S}_y)$ is weak. H_{S0} splits the ^3E state into three equally separated orbital doublets. The spin-spin interaction $H_{SS} = D_{es}(\hat{S}_z - 2/3)$ shifts these three levels and also lifts the degeneracy of A_1 and A_2 levels by splitting $\pm\Delta$ (Fig. 2.1.3 (a)). Thus at zero strain the splitting of the fine structure of the ^3E state is characterized by parameters: $\lambda_z = 5.5$ GHz, $D_{es} = 1.42$ GHz, $\Delta = 3.1$ GHz and $\lambda_{x,y} = 0.2$ GHz [37].

Also, the local strain can perturb the fine structure. More precisely, the local strain can be described by the Hamiltonian: $H_{str} = \delta_x \hat{V}_x + \delta_y \hat{V}_y + \delta_z \hat{V}_z$, where δ is the strain parameter and $\hat{V}_i$ is a orbital operator along the i direction. The axial strain is along the quantization axis z which is along the trigonal symmetry axis of the NV pair. Since the E is a doubly degenerate level, under a non-axial strain (transverse to the trigonal axis) the ^3E level is separated into two branches, E_x and E_y, each containing S_x, S_y and S_z spin projections. The transverse strain is described by δ_x and δ_y and the splitting is proportional to $\delta_\perp = (\delta_x^2 + \delta_y^2)^{1/2}$. The effects of the spin-orbit, spin-spin and strain interactions are shown in Fig. 2.1.3 (a) and (b).

f2. Room temperature

The fine structure of the ^3E state at room temperature was first observed by [38] and then confirmed by refs. [39, 40]. However, it was Rogers et al. [37] who correctly explained the temperature dependence of the fine structure. Rogers et al. attributed the change of the fine structure behavior with temperature to a phonon-mediated averaging process.

Due to the averaging the contribution of spin–orbit interaction λ_z and spin-spin interaction Δ are effectively quenched. Thus, the averaging process results in an average state with only a zero field splitting determined by the spin–spin interaction D_{es}. So, finally, at room temperature, the fine structure of the excited ^3E state can be described by the same Hamiltonian as the ground $^3A_2$ state.

Interestingly, because of this averaging process, stronger spin polarization, which will be discussed in next section, is obtained at room temperature than at low temperature [37], which makes the NV center more attractive for the quantum application at room temperature.

2.1.4 Optical properties

An important feature of the NV^- center is linked to its bright and stable photoluminescence as shown in Fig. 2.1.5 (a).

a. Optical transitions: internal transitions and capture processes

In general, optical emission of defects can be divided into two categories: due to *internal* transitions and due to the *capture* process, also called the photoconversion process [21]. An internal transition occurs between two many-body states of the defect and the charge of the defect is conserved. In contrast, during the capture process, an electron can be emitted from the valence band and captured by one of the defect state, with the consequence that the charge state of the defect changes. In this manuscript I mainly consider the *internal* transitions.

b. Zero phonon line (ZPL)

When talking about the photoluminescence spectrum, the NV^- spectrum contains an optical fingerprint which helps identifying the existence of the defect center in the diamond structure. The fingerprint is a bright zero-phonon line at 1.945 eV (637 nm) [25]. The zero phonon line is an electron transition from the lowest vibronic state of the electronic excited state to the electron ground state via photoemission. It results in a sharp bright peak in the photoluminescence spectrum (Fig. 2.1.5 (b)).

c. Vertical excitation (VE)

We remind the reader that according to the Franck–Condon principle, the electron excitation occurs on a much faster time scale than the vibronic relaxations. When an electron is excited from the ground state, the transition is referred to as a vertical transition. In ref. [28] the vertical transition was assigned to be 2.2 eV by measuring an absorption spectrum.

The vertical transition and zero phonon line are schematically represented in Figure. 2.1.4

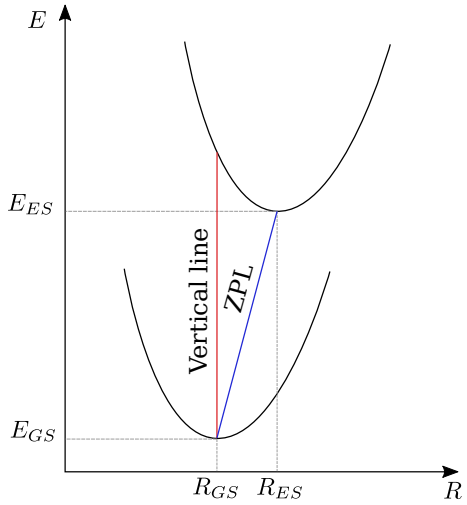

Figure 2.1.4: Schematic representation of the energy as a function of the configurational coordinate during the excitation process. The excitation occurs with a vertical transition. However, shortly after the electron excitation, nuclei around the defect relax finding a new equilibrium atomic configuration. This relaxation occurs through interaction with phonons. The emission from the lowest vibronic state is a zero phono line.

d. Phonon side-band

The photoluminescence spectrum contains also the broad part of phonon-assisted transitions. This broad part of the spectrum is called the phonon side-band. It occurs due to the interaction of the ^3E excited state with totally symmetric, quasilocalized vibrational modes that involve the displacement of the nitrogen atom and the carbon atoms surrounding the vacancy [41]. A schematic photoluminescence spectrum is shown in Fig. 2.1.5 (b).

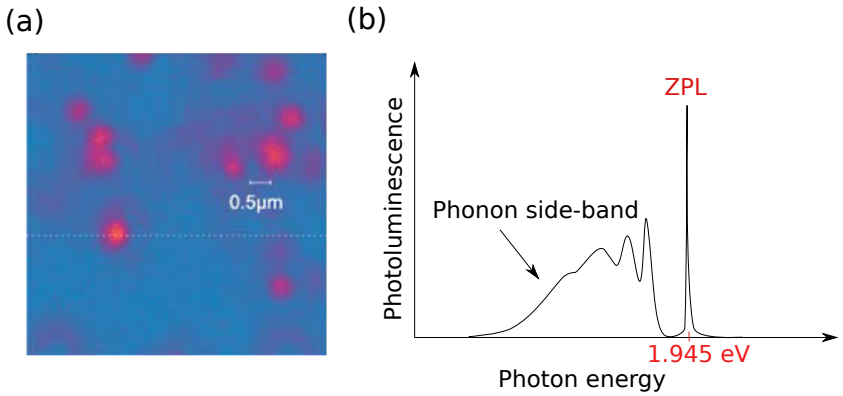

Figure 2.1.5: NV^- center. (a) Room temperature confocal image observed in ref. [19]. (b) Schematic representation of the photoluminescence spectrum of the. Figure is adapted from ref. [21].

The bright zero-phonon line at 1.945 eV occurs due to the triplet-triplet $^3E -^3 A_2$ transition. Another zero-phonon line of the NV^- center was observed in the infrared region of the spectrum, at 1.19 eV [42]. In the ref.[42] Rogers et al. have identified the symmetry of the transition as $E - A_1$ by the uniaxial stress investigation. They have also found that the transition corresponds to the singlet-singlet transition because of the absence of the Zeeman splitting or of the broadening of the infrared zero-phonon line. The presence of two singlet states between the ground state triplet $^3A_2$ and excited triplet ^3E plays an important role in the non-radiative decay. The presence of two singlet states plays also an important role in the optical spin polarization of the NV^- center as will be discussed in the section 2.1.5.

2.1.5 Optical dynamics

Another important property of the NV^- center is the spin selective fluorescence that enables the magnetic resonance measurements. We have seen in section 2.1.3 that the NV^- center has a fine structure of the excited state similar to the fine structure ground state at the room temperature. The optical transitions of the NV^- center obey the selection rules $\Delta m_s = 0$, so the allowed optical transitions occur between the levels of the same spin projection [4, 43]. Moreover, it was observed that the fluorescence between the corresponding $m_s = 0$ ground and excited states is stronger than the the fluorescence between the $m_s = \pm 1$ ground and excited states because of the non-radiative decay from ^3E $m_s = \pm 1$ to the $^1A_1$ level [26, 44]. This spin selective behavior was observed with the help of the optically detected magnetic resonance experiments (ODMR) in the ref. [26].

The spin selective fluorescence can be explained as follows. During an ODMR experiment, the optical pumping is accompanied with a microwave excitation. When the microwave frequency coincides with the frequency of the magnetic resonance of the ground state, the $m_s = 0$ level is depopulated and the subsequent optical excitation occurs from the $m_s = \pm 1$ level. When the electron is excited to the ^3E $m_s = \pm 1$ state, two paths of the relaxation are possible: the direct decay to the ground state or the non-radiative decay to the intermediate singlet levels. The non-radiative decay is possible due to the spin-orbit interaction which couples the triplet and singlet state as in this case $\Delta m_s \neq 0$. This process is called the intersystem crossing (ISC). Also it is believed that this process is phonon-assisted [45]. Since the non-radiative decay rate of the $m_s = \pm 1$ excited state is much larger than that of the $m_s = 0$ excited state, the resulting fluorescence of the $m_s = \pm 1$ state is lower. Thus, we observe a notch in the ODMR spectrum with the minimum fluorescence at the ground state resonant frequency as depicted in Fig. 2.1.6 (b). This ODMR spectrum peak is also called the ODMR contrast [36]. This technique is routinely applied for single-spin state optical readout [40].

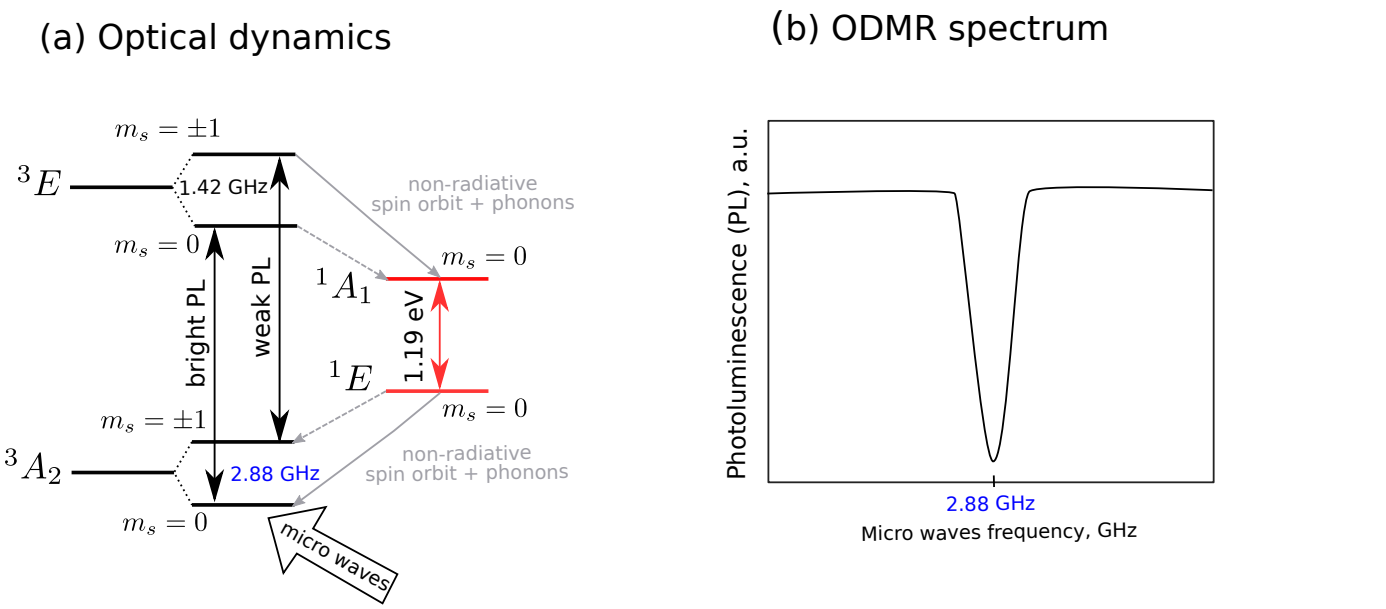

Figure 2.1.6: (a) Schematic representation of the photoluminescence excitation and decay path. The grey solid lines represent strong non-radiative decay. Grey dashed lines represent weak non-radiative decay. (b) Schematic representation of the optically detected magnetic resonance spectrum of the NV^- center.

Another important property during the optical excitation is a spin polarization of the NV^- center. The spin polarization occurs in a following way. After the non-radiative decay of the electron to the $^1A_1$ state and a 100 ps electronic lifetime in the $^1A_1$ state [46], a fast optical emission to the ^1E state follows, as evidenced by the presence of the ZPL at 1.19 eV. The ^1E state has a longer lifetime than the $^1A_1$ state and vary between about 371 ns and 165 ns depending on temperature [47]. Then, from the ^1E state the system preferably decays towards the ground state $m_s = 0$ sublevel through the ISC, which is still not completely understood [40, 48] (Fig. 2.1.6 (a)). As the consequence, after a few optical excitation–emission cycles the $m_s = 0$ ground state sublevel is populated and the $m_s = \pm 1$ depopulated. Thus, the ground state of the NV^- center is spin polarized [49].

To conclude, we have seen that the ground state of the NV^- center can be optically manipulated. The ground state spin can be optically prepared to the $m_s = 0$ state at the room temperature. Moreover, the current state of the NV^- center can be optically read out due to the spin selective fluorescence. These properties enable the use of the NV^- within the wide domain of the applications in quantum technologies. In this work I will concentrate on the magnetic sensing with the NV^- center.

2.2 Magnetic sensing

2.2.1 The Meissner effect

The Meissner effect is the signature of superconductivity. The Meissner effect is defined as the expulsion of the external magnetic field from a superconducting sample as the sample undergoes a superconducting transition under the cooling. Thus, in order to unambiguously prove the onset of a superconducting state, one must observe the Meissner effect. One of the possibilities to observe the Meissner effect is through the magnetic measurements.

2.2.2 Magnetic sensing at ambient pressure

In the section 2.1.3 it was shown, that the spin selective photoluminescence of the NV^- center exhibits a resonant ODMR peak at 2.88 GHZ when a continuous micro wave excitation is applied. The application of an external magnetic field splits the ODMR peak into two peaks: the $m_s = 1$ and the $m_s = -1$ projections. This splitting occurs due to the Zeeman effect. Indeed, the spin Hamiltonian of the defect with C_{3v} symmetry and with the applied external magnetic field $\mathbf{B}$ is following:

$$H = D(S_z^2 - S(S+1)/3) + g\mu_B \mathbf{B}\cdot \mathbf{S} = H^z + H^\perp \tag{2.1}$$

where D is the zero-field splitting constant, the z coordinate axis coincides with the center trigonal symmetry axis, g is a Landé factor and μ_B is Bohr magneton. One should mention that both the strain effect and the hyperfine interaction is neglected in this Hamiltonian for the sake of simplicity. The first term describes the zero-field splitting in the absence of the external magnetic field, as discussed earlier. The second term describes the Zeeman splitting. One can see that the Zeeman splitting of the ODMR peak is proportional to the magnetic field amplitude along the intrinsic quantization axis that is defined by the NV pair direction, as depicted in Fig. 2.2.1. Thus, the splitting of the NV^- center ODMR spectrum allows the direct measurement of the magnetic field amplitude, and enables the use of the NV^- centers for magnetometry applications. The advantage of the use of the NV^- centers as an *in-situ* magnetic sensors is its μT magnetic sensitivity along with the atomic-scale resolution [12].

The detection of the ODMR contrast under an applied external magnetic field, however, has some limitations. It was observed in ref. [50] that the ODMR contrast decreases when the condition $H^z >> H^\perp$ is not satisfied or, in other words, when a strong transverse magnetic field dominates. The decrease of the ODMR contrast occurs because of the spin mixing of the $m_s = 0$ and $m_s = \pm 1$ components. This effect was explained in ref. [50] by the fact that m_s is not a good magnetic number when the quantization axis is defined by the external magnetic field. Thus, the eigenenergies of the Hamiltonian 2.1 are the superposition of the $m_s = 0$ and $m_s = \pm 1$ components, so that the spin-selective photoluminescence and the optical spin polarization become inefficient.

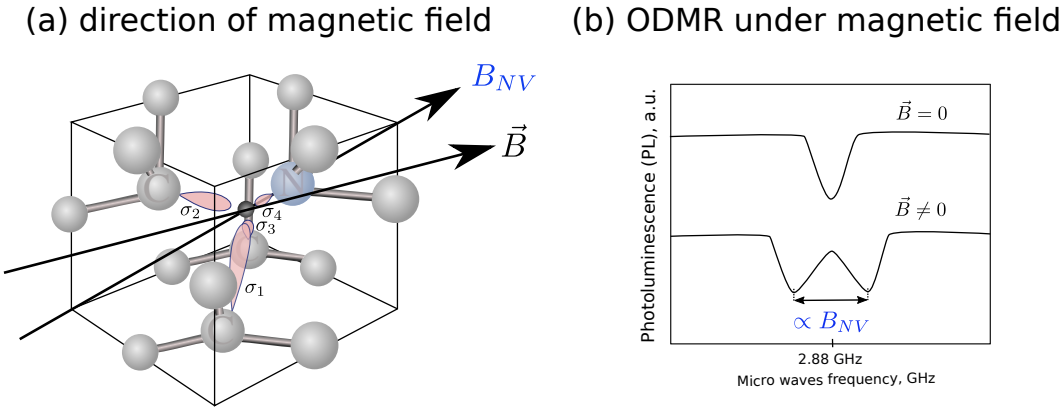

Figure 2.2.1: (a) Schematic representation of the direction of the magnetic field and the projection of the magnetic field on the axis along the NV center axis; (b) Schematic representation of the optically detected magnetic resonance spectrum of the NV^- center with applied magnetic field.

2.2.3 Magnetic sensing under high pressure

a. Purpose

High pressure applied on a semiconducting or insulating solid may lead to the closure of its electronic band gap and eventually may generate metallic and superconducting states. For instance, the sulfur hybrid H_3S has been recently shown to exhibit the superconductivity at the temperature of 203 K at 150 GPa pressure applied [51]. This temperature is the highest superconductivity transition temperature ever measured. Pressures above 100 GPa are routinely obtained in a diamond anvil cells (DAC) but the tiny sample volume available in such a cell is almost incompatible with most of non-optical detection state of the art schemes. The measurement of the superconductivity under high pressure add the additional complexity to the problem since the experimental setups have to be adapted in order to be operational with the DAC. In order to appreciate the elegance of the NV center based method to measure magnetic and superconducting properties one should briefly explain the challenges of the state of the art techniques.

b. State of the art techniques

The state of the art techniques consist primarily of two methods: the SQUID [52] and the use of the synchrotron radiation [53–55] to detect either the Mössbauer effect or the magnetic circular dichroism.

b1. Transport measurements

The superconducting material exhibits a number of extraordinary properties. We have already discussed the Meissner effect, another property inherent to the superconductor is the zero electric resistance. Thus, the onset of superconductivity can be observed through

a transport measurement [56]. Nevertheless, this method is hardly convincing once implemented in DAC. Due to the constraints of the DAC environment, a measurement of resistivity is difficult to reproduce and is doomed to errors due to: (i) the averaging, implicit in a transport measurement; (ii) the difficulty of contacting the sample once compressed by the two diamond anvil; (iii) the pressure-induced deformation of the leads. Thus, other methods have been used to measure the onset of superconductivity in a DAC.

b2. The SQUID

The use of a superconductivity quantum interference device (SQUID) enables to measure the small response to a magnetic field induced in diamagnetic materials [52], as is the case in the Meissner effect at the superconducting transition. In its principle, a SQUID consists of two Josephson junctions connected in parallel in the superconducting loop, that allows to detect the variation of the flux of the magnetic field inside the superconducting loop, where the sample is located. At the superconducting transition the magnetic field is expelled from the sample and the drop of the magnetic field is detected by the SQUID.

Working at high pressure, however, requires adapting the DAC to the SQUID [57]. Moreover, the protocol requires to repeatedly increase the pressure outside the SQUID and then to insert the DAC back into the SQUID to measure the magnetic moment. At ambient pressure the measurement takes approximately one hour. Thus, measuring the Meissner effect at high pressure with this technique is a long process.

b3. Magnetic Circular Dichroism (MCD)

MCD is a differential optical spectroscopic technique that determines the difference of left and right circularly polarized light in the presence of an axial magnetic field [58]. For instance, in ref. [53] the x-ray MCD has been applied in order to investigate the change of the magnetization of Ni under the compression. XMCD signal was obtained by taking the difference between x-ray absorption spectra measured using parallel and antiparallel orientations of the sample magnetization relative to the incident photon helicity. If a sample present a net ferromagnetic or ferrimagnetic moment. The XMCD signal is then directly proportional to the magnetic moment on the absorber atom [54]. However, since this technique mainly addressing nuclear or electronic transitions and not the Meissner effect directly, it is difficult to extract absolute quantitative information on the magnetic moment.

b4. The Mössbauer spectroscopy

Mössbauer spectroscopy is based on the Mössbauer effect. The Mössbauer nucleus with its nuclear magnetic moment acts as a local probe in the solid. The nuclear and atomic (electronic) magnetic moments are coupled by the magnetic hyperfine interaction. This provides that the nuclear magnetic moment senses a local magnetic field produced by the electrons [59].

For instance, in ref. [60] to detect the expulsion of the magnetic field in the hydrogen sulfide (H_2S), the foil of tin enriched with the ^{119}Sn Mössbauer-active isotope was used as the sensor. The screening of the external magnetic field during the superconducting transition of the H_2S was monitored with the nuclear resonant scattering of synchrotron radiation that interacted with the spin 1/2 of ^{119}Sn nuclei. The main problem of Mössbauer spectroscopy is the small number of Mössbauer isotopes, which limits a number of magnetic materials that can be studied with this technique [54].

c. The NV^- as a magnetic sensor at high pressure

As we have seen, synchrotron based methods are widely used for the characterization of the magnetic state under high pressure, however, these techniques encounter a number of drawbacks such as (i) the non-unambiguous interpretation of signals; (ii) requirement of specific isotopes or conditions to be implemented and (iii) access to a dedicated synchrotron beam-line.

Thus the use of NV diamond color centers as *in-situ* magnetic sensors integrated in the DAC can enable scientists to address in table-top experiments open questions such as the close to room temperature superconductivity or the exploration of complex quantum phase diagrams when magnetic materials are pushed to high pressures. A very recent advance of the technique using NV centers allowed to observe the pressure evolution of the magnetization of an iron bead up to 30 GPa showing the iron ferromagnetic collapse and to see a Meissner effect associated to the superconductivity of MgB_2 at 7 GPa [15]. Indeed, in ref. [15] NV center defects were directly implanted 20 nm below the surface of the diamond anvil culet by a focused ion beam [61]. The excitation of the NV centers and the measurement of their photoluminescence was performed with a green 532 nm laser through the diamond anvil. The ODMR spectrum was then measured by applying the microwaves with a turn coil that was attached to the rhenium gasket which confined the sample. The scheme of the experimental setup is shown in Fig. 2.2.2. In ref. [15] the sample was either an iron bead or MgB_2 crystal placed into the DAC, and a ruby crystal was used to calibrate the pressure inside the DAC. The DAC was filled with a pressure transmitting medium (nitrogen or argon) which provided the hydrostatic pressure inside the chamber during the experiment.

The optical magnetometry method based on NV center developed in ref. [15] as discussed in previous section, is an elegant technique which beats with its easiness, non-invasiveness and possibility to map a stray magnetic field with a micrometer spatial resolution. Although the results of this method are very promising, in order to exploit this technique at higher pressures, an attentive study of the behavior of the NV center itself at high pressures is of a key importance and one of the main objectives of the present work.

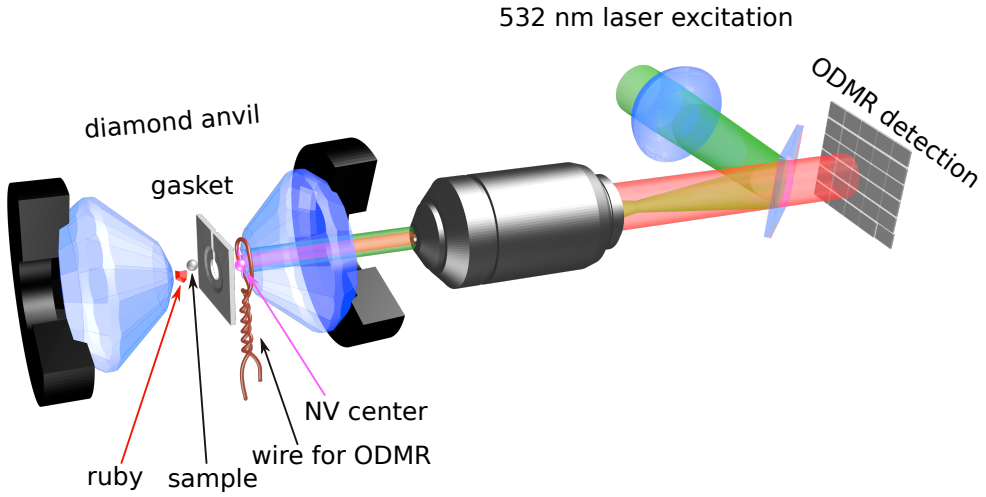

Figure 2.2.2: Magnetometry in diamond anvil cell with NV center. Scheme of the setup for the optical magnetometry based on measurements with NV centers. The figure is taken from ref. [15].

2.3 Behavior under hydrostatic pressure of the NV^- center

At the beginning of this work two experiments had been reported that studied the behavior of the NV^- center under pressure: Kobayashi and Nisida [16] and Doherty ar al. [17]. During the course of my PhD work, Lyapin eta al (2018). [62], B. Vindolet et al. (my collaborators) and Hsieh et al. [63] reported new experimental results. The results of Vindolet et al. and Hsieh et al. showed, however, that implanted NV centers were submitted to uniaxial pressures rather than the quasi-hydrostatic ones. The behavior of two distinct quantities has been reported.

2.3.1 Experiments

Doherty et al. [17] in their experimental study observed and measured the shift of the ground state optically detected magnetic resonance (ODMR) and of the optical ZPL of NV^- under the quasi-hydrostatic conditions.

a. Shift of the fine structure of the GS

Doherty et al. observed, from their ODMR spectra, that the shift of the splitting parameter D is mainly linear with pressure P and has a gradient $dD(P)/dP$=14.58 MHz/GPa.

An explanation of the pressure shift that has been proposed by Doherty et al. [17] in order to explain the shift of the ODMR splitting was the following. The contraction of the lattice under pressure leads to the shortening of distances between atomic orbitals. This

induces a change in defect orbitals, as they are linear combinations of atomic orbitals. The change of the defect orbitals corresponds to the compression of the unpaired spin density of the ground state, that provokes an increase of the spin-spin interaction.

b. Shift of the ZPL

In ref. [17] the shift of the optical ZPL transition energy between ^3E and $^3A_2$ states was linear with a gradient dZPL(P)/dP=5.75 meV/GPa at 296 K, which was in a good agreement with an earlier observed at low temperature of 77 K gradient 5.5 meV/GPa in the work of Kobayashi et al. [16].

In the recent work of Lyapin et al. (2018) [62] also studied the NV^- center under the hydrostatic pressure. In their experiment micro- and nanoscale diamonds, were placed in a diamond-anvil cell (DAC) along with ruby crystal for the pressure measurements. The sample chamber was filled with the He pressure transmitting media. In order to record the photoluminescence the excitation was induced with the 499 nm Ar^+ laser.

Lyapin et al. have found dZPL(P)/dP=5.81 meV/GPa at 296 K and dZPL(P)/dP=5.57 meV/GPa at 80K. The ZPL measured in their experiment was in a good agreement with the previous works [16, 17]. They, however, noticed that the photoluminescence pressure gradient is 5.81 meV/GPa and deviates slightly from the linear behavior.

In Table 2.1 we summarize available experimental results. The pressure behavior of the photoluminescence of the NV^- center

Table 2.1: Comparison of the experimental shift of the ZPL in the NV^- center. PTM stays for pressure transmitting medium. The hydrostatic pressure limits are taken from [64] for gases and from [65] for NaCl. NaCl-type (B1) structure undergoes a phase transition to the CsCl-type (B2) structure at around 30 GPa

	PTM	hydrostatic until P_{max} (GPa)	T (K)	dZPL(P)/dP (meV/GPa)
Kobayashi [16] (1993)	N_2	2.4	77	5.5
Doherty [17] (2014)	NaCl/Ne	30/4.8	296	5.75
Lyapin [62] (2018)	He	12.1	80 296	5.57 5.81

c. The loss of the optically detected magnetic resonance (ODMR) contrast

Also, in the ref. [17] Doherty et al. have found that the ODMR contrast (see definition in section 2.1.5) disappears at pressures above 17.9 GPa in the NaCl pressure medium as shown in Fig. 2.3.1. In the Ne pressure medium the contrast disappeared at 60 GPa. This effect is not yet explained, and of the objectives of the present work is to provide more understanding of this contrast loss.

The possibility to record the ODMR spectrum comes from the dark intersystem crossings (ISCs) between the excited triplet ^3E and the singlet $^1A_1$. There could be several explanations of the loss of the ODMR spectrum contrast.

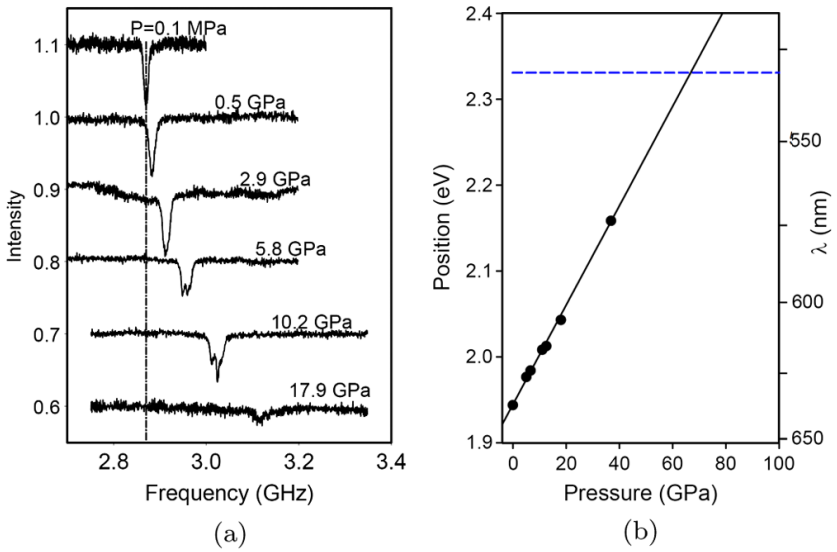

Figure 2.3.1: Optically detected magnetic resonance (ODMR) experience under high pressure. (a) NV^- ODMR spectra. NaCl remains a good transmitting medium below 30 GPa [66] which guarantee quasi-hydrostatic pressure conditions. The dashed line indicates the position of the resonance at ambient pressure. (b) Pressure shift of the ZPL of the NV^- center. The solid line is a linear fit extrapolated to the position of the 532 nm excitation laser. Figures are taken from [17].

The first hypothesis is connected to the purely technical problem. Since we have seen that there is a shift of the optical triplet-triplet ZPL emission, and since the absorption spectrum usually obeys the mirror law and is symmetric to the emission spectrum, one can imagine that there could be a shift of the absorption peak. Taking into account that in the experimental setup of ref. [17] the excitation of the NV^- center was performed with the help of a green laser at the fixed 532 nm wavelength, one can propose that the NV^- center excitation maximum was shifted under the influence of the pressure, so the laser excitation was not efficient anymore to induce the polarization process.

Another hypothesis may be linked to the fact that the singlet $^1A_1$ state behaves differently under pressure than the ^3E, so at the end the intersystem crossing decreases, directly providing the loss of the ODMR contrast. The process of the intersystem crossing is believed to be mediated by spin-orbit and electron-phonon coupling. Study of the spin-orbit coupling and electron-phonon coupling is beyond of the scope of this work. However, the behavior of the related excited many-body states under the pressure is of key importance for understanding of this process and will be studied in this work.

2.3.2 Theoretical works

There are a few works that studied the behavior of the NV center under hydrostatic pressure. In 2014 Deng et al. [18] have studied NV^- center under hydrostatic pressure with constrained occupation density functional theory (CDFT). This methodology to calculate excited states of defects will be discussed in chapter 4. Deng et al. have studied the triplet-triplet $^3E - ^3A_2$ ZPL transition and found the gradient $d\text{ZPL}/dP$=5.75 meV/GPa.

In the course of my PhD, Lyapin et al. (2018) [67] reported another ab initio study, the negative NV^- center have been studied with DFT. Lyapin et al. have reported the calculated pressure coefficient of the NV^- center of 6.5 meV/GPa with respect to his experimental value 5.75 meV/GPa. In these calculations only redistribution of electron density with pressure increase was taken into account. However, no details available about the method that has been used for these calculations. Though the calculated pressure coefficient is in good agreement with the experimental results for the NV^- we will see in chapter 3 that there were some discrepancies between calculations and experiment in the case of the NV^0 center.

2.3.3 Conclusion

Till now, only the behavior of the triplet-triplet $^3E - ^3A_2$ transition under hydrostatic pressure was studied theoretically and no studies are available for the singlet-singlet transition. I aim to study the behavior of the whole set of the low lying excited states of the NV center under hydrostatic pressure and to understand the loss of the ODMR contrast. This points will be discussed in part II, chapter 6. The pressure coefficients of the ZPLs will be discussed in part II, chapter 4.

2.4 Behavior under a uniaxial pressure of the NV^- center

2.4.1 Experiments

a. Introduction

In fact, semiconductors have been intensively studied under various strain/stress conditions in order to determine their optical constants under strain as well as deformation potentials due to the electronic interaction with strains or with acoustic phonons [68, 69]. The pressure applied in these cases is, however, much smaller than the one applied in DAC in order to study the superconductivity. Indeed, these quantities (optical constants under strain, deformation potentials) have been usually determined with strains introduced as a small perturbation (in the vicinity of P=0).

The application of the strain/stress has also been widely used to study the fine structure of defects in semiconductors and to determine the symmetry of their ground and excited

states [70]. One of such experiments has been described in section 2.1.3, due to this study the new insights about the fine structure of the excited state ^3E were provided [36].

b. Measured quantities

In another experimental work [33] Rogers et al. performed series of experiments where external stress is applied to the diamond along well-defined crystal axes while the displacement and splitting of the ZPL were measured. Their study allowed to measure stress parameters and to unambiguously identify the ordering of the singlet levels.

In general, stress along the symmetry axis results in shifts of the energy levels while transverse stress lifts the degeneracy of the E state. Rogers et al. studied NV center with application of stress along [001], [111] and [110] directions by means of a pneumatic driven rod. Stress along these directions is always in a reflection plane or at right angles to a reflection plane, and consequently the defect symmetry is always lowered to C_s, which may lead to the different effect with respect to the hydrostatic pressure.

Rogers. et al. have measured the ZPL shift and splitting of both triplet-triplet $^3E - ^3A_2$ transition and singlet-singlet $^1A_1 - ^1E$ transition. They have found that the interaction giving rise to the shift and splitting of the singlet-singlet ZPL is different from that giving rise to the shifts and splittings of the triplet-triplet ZPL. Summarizing their results, they have found that the shift parameters due to the uniaxial stresses were smaller for the singlet-singlet transition than for the triplet-triplet transition. Contrary, the splitting stress parameters for the singlet-singlet transition were larger than for the triplet-triplet transitions.

2.4.2 The Hamiltonian under a uniaxial strain/stress

The theory for uniaxial stress applied to an $A-E$ transition at a defect of trigonal symmetry been developed by Davies and Hamer [28, 71]. The stress perturbation at the NV center whose axis is along [111] direction, defined as Z axis is given by the Hamiltonian

$$\begin{aligned}\hat{H}^s = &\hat{A}_1(s_{xx}+s_{yy}+s_{zz}) + \hat{A}'_1(s_{yz}+szx+s_{xy})\\ &+\hat{E_X}(s_{xx}+s_{yy}+2s_{zz}) + \hat{E_Y}\sqrt{3}(s_{xx}-s_{yy})\\ &+\hat{E'_X}(s_{yz}+szx+2s_{xy}) + \hat{E'_Y}\sqrt{3}(s_{yz}-s_{zx})\end{aligned} \tag{2.2}$$

where the stresses s_{ij} defined with respect to the crystal axes x, y, z. The operators A_1, A'_1 are symmetry adapted electronic operators transforming as A_1 irreducible representations and E_X, E_Y, E'_X, E'_Y are operators transforming as components of E irreducible representations.

Davies and Hamer have defined stress coupling coefficients in terms of the reduced matrix elements of the operators A_X,A,E_X, E_Y, E'_X, E'_Y between the $|A\rangle$, $|E_X\rangle$ and $|E_Y\rangle$ states of the center as follows:

$$\begin{gathered}A_1 = \langle E||\hat{A}_1||E\rangle - \langle A||\hat{A}_1||A\rangle, \quad 2A_2 = \langle E||\hat{A}'_1||E\rangle - \langle A||\hat{A}'_1||A\rangle\\ B = \tfrac{1}{2}\langle E||\hat{E}||E\rangle, \quad C = \tfrac{1}{2}\langle E||\hat{E}'||E\rangle\end{gathered} \tag{2.3}$$

where A_1, A_2, B and C are the stress parameters that describe the shifts and splitting that have been observed under different uniaxial stresses discussed in previous section 2.4.1 (a).

2.5 The molecular model predictions for the hydrostatic pressure

Though, Rogers et al. have not studied the effect of the hydrostatic pressure on the triplet and singlet transitions, they have proposed the following statement using their molecular model that has been already discussed in section 2.1.1. If the symmetry is not changed by the applied stress (as it is a case for the hydrostatic pressure), it will only alter the $a_1 - e$ energy separation. This will result in a change of the energy separation between configurations but cause no change within each configuration.

Rogers et al. have considered as example the interaction in relation to the singlet transition. The $^1A_1$ $(a(2)e(2))$ - ^1E $(a(2)e(2))$ transition is between levels within the same $a(2)e(2)$ configuration and so the transition energy cannot be shifted by the hydrostatic strain.

2.6 Conclusions

In the present work, since I will study the behavior of the singlet and triplet transitions under hydrostatic pressure, I will be able to check the theory of Rogers et al.

CHAPTER 3

Physics of NV^0 center in diamond

3.1 Introduction

During the fabrication of NV center defect, diamond which naturally contains some concentration of substitutional nitrogen is exposed to irradiations in order to create vacancies [28]. The annealing at 600 °C enables the migration of vacancies, so vacancies can be trapped by nitrogen atoms, creating the NV centers. NV centers can exist in both the neutral and negative charge states. In the case of the negative NV^- center, the neutral NV^0 defect traps an additional electron from the diamond environment. Presumably, the electron is donated by the substitutional nitrogen atom which is left in diamond after the formations of NV centers. We have already discussed the most important properties of the negative NV^- center in chapter 2. In this chapter I discuss the neutral NV^0 center.

As we have seen from the previous chapter, the negative NV^- center is a unique defect whose spin dependent fluorescence and spin polarization make it attractive for numerous applications in quantum technologies. Contrarily to the NV^- center, the neutral NV^0 center has not been observed to manifest the analogous optical properties and thus was not studied as intensively as the negative NV^- center. Consequently, too little is understood till now about the neutral NV^0 center. In particular, there are no many theoretical works that study the NV^0 center under high pressure. The study the NV^0 center under high pressure is the second main objective of the present work.

3.2 The NV^0 center at ambient pressure

3.2.1 Defect structure and charge state

The atomic structure of NV^0 defect is the same as that of the negative NV^- center with exception of the charge state. Mita [72] has shown that the NV^0 optical band observed at 2.156 eV (575 nm) corresponds to the neutral charge state of the NV center. Thus, the molecular model of the NV^0 center represents 3 dangling bonds from carbon atoms and one lone pair from the nitrogen atom, with 5 electrons distributed between them. Linear combinations of these dangling bonds yield the same four defect levels as for NV^- center. These defect levels $a_1^N a_1 e$ are situated in the valence band and in the gap of diamond. However, since they are occupied with 5 electrons, the electronic structure of the NV^0 center is different from the one of the NV^- center.

3.2.2 Optical properties

The NV^0 center main optical feature consists of the bright and sharp ZPL at 2.156 eV (575 nm). This photoluminescence has been associated to optical transitions between the ground and excited states with the orbital symmetry E and A respectively [28]. The definition of the orbital symmetry of the NV^0 center states involved in optical transition was established by photoluminescence polarization and uniaxial stress studies at the same time as for the NV^- [71] (see sections 2.1.1 and 2.4).

3.2.3 Spin state

The definition of the spin multiplicities of the optical transition of the NV^0, however, has been a difficult task. Notably, because the NV^0 center does not have a detectable electron paramagnetic resonance (EPR) signal related to it ground state nor to the first excited state [20]. This absence was proposed to be linked with the dynamic Jahn-Teller effect characteristic to the partially occupied double degenerate state of the E symmetry, so that the NV^0 center ground state was proposed to be a ^2E doublet [73]. At the same time, it was found that the NV^0 center exhibited an EPR signal under a continuous excitation [73]. This signal corresponded to an intermediate quartet $^4A_2$ excited state. The presence of the quartet state in the NV^0 center confirmed once more the assignment of the neutral charge because it confirmed the 5 electron model.

3.2.4 Symmetry of the ground state and excited state

The exact A_1 or A_2 symmetry of the optically excited A state s been a source of contentions for a long time. Because of the absence of an EPR signal, and because the strain experiments cannot distinguish between A_1 and A_2 symmetries [71], for a long time the excited state has been erroneously assigned to the $^2A_1$ symmetry [74, 75]. Indeed, the group theory analysis of the molecular model predicts three different doublet states (^2E, $^2A_1$, $^2A_2$) associated to the excited state configuration $a_1^N(2)a_1(1)e(2)$, the ordering of these doublets is unknown experimentally. It was presumed that the optical transition is more likely to occur between the lowest lying doublet and ground state doublet. It is only since the recent study of ref. [76] that the 2.156 eV transition in NV^0 has been assigned to $^2E - ^2A_2$ transitions. In order to reach this conclusion Manson et al. [76] have measured the time-averaged emission spectrum of one single NV defect in diamond. This allowed for the simultaneous detection of the ZPLs of the NV^0 and NV^- centers. They have found that due to strain in diamond the ZPLs of both charge states were split and it was found that the splitting and polarization of the two ZPLs were identical. The strain splitting was observed for the NV^- center excited state ^3E and for the NV^0 center's ground state ^2E, because both states have the doubly degenerate E symmetry. Taking in account that selection rules imply that the strain split ZPLs of NV^0 and NV^- can only have identical polarization if the other levels involved in the transitions have identical orbital symmetry, and since in the NV^- center another level involved in the optical transition is A_2 symmetry.

It was concluded that in the NV^0 center the optical transition should also occur between the levels with the E(GS) and A_2(ES) symmetries.

a. The $NV^0 - NV^-$ photoconversion process

The symmetry assignment of optical transitions at 2.156 eV in the NV^0 center has been achieved due to the possibility of recording simultaneously the ZPL signals of both NV^- and NV^0 centers. One should mention that this possibility itself is due to another important property of the NV center - the photoconversion process. The photoconversion process relies on the capture process discussed in section 2.1.4.

The observation of the photoconversion process was done by Manson et al. [77]. The photoconversion process belongs to the external transition type, accompanied by the change of the charge state of the NV center during the excitation. Indeed, when exciting a single center at a wavelength that coincides with the sidebands of both charge states, the one center is converted back and forth between the two charge states. This process is yet to be fully understood.

Some recent works explain this process with the help of a combination of two photon absorption process and Auger effect [22, 78–80]. According to the currently available explanation, first, the simultaneous absorption of two photons by a NV^- center promotes an electron from the a_1 orbital in the band gap to the conduction band via the e level in the gap. When the electron is above the conduction band edge, it can fall back to the a_1 orbital by kicking out another electron at e orbital and thus converting NV^- in its neutral ground state. Next, in order to convert the NV^0 back to its negative charge, another two-photon absorption is needed to promote an electron from the a_1 orbital to the e orbital and then, to promote an electron from the valence band into the empty a_1 orbital in the gap.

This process has been confirmed with the ab initio calculations [22, 79] by the calculation of the Auger-recombination rate. The Auger-recombination rate was written as a Coulomb interaction between the initial exciton state and all the possible final exciton states in ref. [79]. Initial and final exciton state have been approximated by the electron-hole Kohn Sham wave functions. In order to obtain the rate of transition, sum over all possible final states was performed: the degenerate $e_{x,y}$ level and the electron in the conduction band minimum. Their calculated Auger-recombination rate was 800 ps. In order to prove that the second photon can be captured by electron on e orbital before the radiative recombination, they have also calculated the radiative recombination lifetime, which resulted in 0.5 μs implying that the Auger-recombination is a faster process, and indeed can take a place before the radiative recombination.

b. Fine structure

Finally, only in 2019, during the course of my PhD work the fine structure of the NV^0 has been determined by magnetic circular dichroism (MCD) spectroscopy [81] (see section 2.2.3 (c)). According to this study, the ground state ^2E has a twofold orbital degeneracy that gives rise to the spin-orbit fine structure as shown in panel (b) of Fig. 3.2.1. The optically

excited $^2A_2$ has no orbital degeneracy and exhibits no zero field fine structure. In ref. [81] Barson et al. have also proposed that the absence of an EPR signal for the ground state of the NV^0 center is likely due to the strain-broadening.

3.2.5 Conclusion

Summarizing all the experimental findings the currently accepted electronic structure of excited state of the NV^0 has been determined very recently and is shown in Fig. 3.2.1. The electronic structure of the NV^0 center consists of the doublet ^2E ground state (S=1/2), the optically excited doublet $^2A_2$ (S=1/2) and an intermediate meta-stable quartet $^4A_2$ (S=3/2). The relative position $^4A_2 - ^2E$ or $^2A_2 - ^4A_2$ is unknown experimentally, however the Hund's rule predicts the $^4A_2$ to be lower than the excited doublets [76].

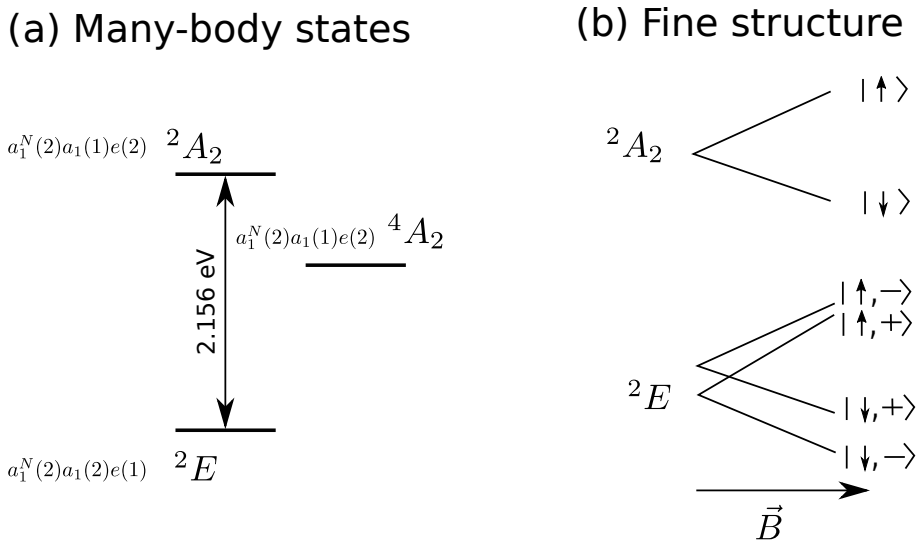

Figure 3.2.1: The NV^0 center (a) Many-body states. (b) Fine structure of the ground state ^2E and excited state $^2A_2$. The arrows represent spin state, $\pm$ represent orbital state The original figure can be found in ref. [81].

In Fig. 3.2.2 I summarize the details of the electronic structure of both NV^- and NV^0 centers known at the beginning of the present work. I show in blue color new details that have been experimentaly observed very recently, during the course of my PhD work. Notably, the fine structure of the NV^0 was finally directly observed in 2019 [81]. Also, the symmetry of the optically excited state $^2A_2$ was determined in 2013 [76]. The elements denoted in red color are the quantities that are unknown experimentally, i.e. the relative energy positioning of the singlet levels with respect to the triplet levels of the NV^- center, or the relative positioning of the metastable $^4A_2$ level with resect to the ground state and excited state doublets in the NV^0 center.

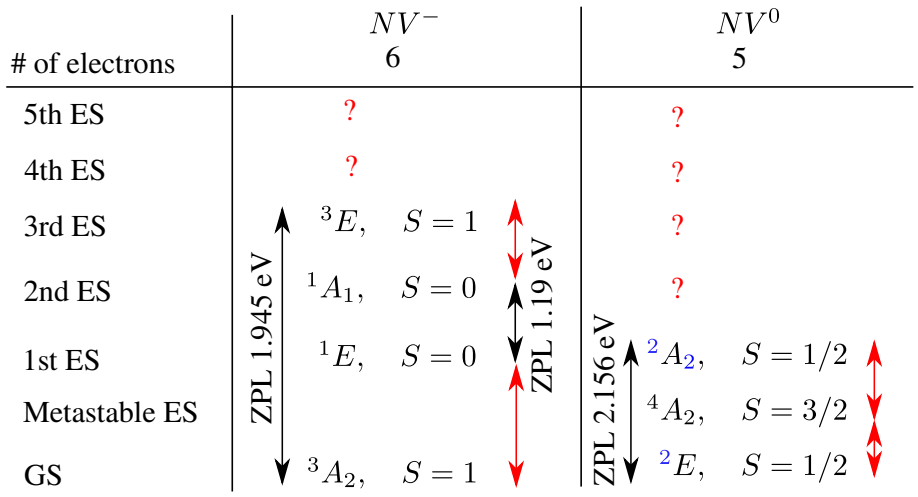

Figure 3.2.2: Electronic structure of the NV center from the experimental point of view at the beginning of the present PhD work. ^3E and $^3A_2$ triplet states are the mono-determinantal states of NV^- center that can be studied in DFT. The $^1A_1$ and ^1E are the singlet states are the many-body states of the NV^-. The ^2E and $^2A_2$ are the many-body doublets of the NV^0 and the $^4A_2$ is a mono-determinantal state of the NV^0. Elements highlighted in blue color have been determined experimentally during the course of the present PhD work [81]. Quantities highlighted in red color are yet to be determined (relative energies of levels).

3.3 Behavior under quasi-hydrostatic pressure of the NV^0 center

3.3.1 Experiments

In a recent study [62] Lyapin et al. have reported a hydrostatic pressure effect study on NV^0 in nano- and micro- diamonds under hydrostatic pressure up to 50 GPa. The pressure gradient of the photoluminescence has been found to be dZPL/dP=2.14 meV/GPa with a linear behavior, which is very different from the pressure gradient of the NV^- center (5.81 meV/GPa, see section 2.3.1). The difference in the pressure behavior of the NV^- and NV^0 centers may be a reason of the decrease of the ODMR contrast of the NV^- center under the pressure, discussed in the section 2.3.1. Since under the excitation there can be a photoconversion process between NV^- and NV^0, under the pressure all the NV^- centers may have been converted into their neutral counterparts and are blocked in this state.

3.3.2 Theoretical works

In the later ref. [67] Lyapin et al. have compared the DFT calculations of the pressure gradient of the NV^- center and the NV^0 with their measurements. One should mention that in DFT calculations only redistribution of electron density with pressure increase was

taken into account. The DFT calculated pressure coefficient 6.5 meV/GPa was in a good agreement with the measured one 5.8 meV/GPa in the case of the negative NV^- center. However, their calculated pressure coefficient for the NV^0 center 5.3 meV/GPa was very different from the measured one 2.14 meV/GPa. Lyapin et al. argumented that the strong correlations have been not taken into account in their calculations. Indeed, the optical transition in NV^0 center occurs between the doublet state, which are highly correlated states with the multi-determinantal nature and thus cannot be accurately treated within DFT.

3.3.3 Conclusion

In this work, additionally to the NV^- center we will study the effect of the hydrostatic pressure on the NV^0 center's many-body states. In order to study the optical transitions of the NV^0 center, we have to address the highly correlated doublet states. In the present work I developed and employed an advanced methodology of the treatment of the highly correlated levels with the Hubbard model as will be explained in the part II.

3.4 Behavior under a uniaxial pressure of the NV^0 center

3.4.1 Experiments

In ref. [71] Davies has measured the photoluminescence and absorption of the NV^0 under small [001], [111] and [110] uniaxial stresses. Similar study has been performed recently on NV^- center in ref. [33] as discussed in section 2.4.1. In both works, the stress shift and splitting parameter A_1, A_2, B and C have been found (see section 2.4.2). In ref. [33] these parameters were compared for both NV^- and NV^0 centers. It was found that the shift and splitting stress parameters of the NV^0 and NV^- centers are very similar and very different from those of the singlet-singlet ZPL transition of the NV^- center. At the moment of the work in ref. [71] the ZPL transition of the neutral NV^0 center has been attributed to the transition between levels with E and A symmetry. The precise symmetry has been determined only very recently by Manson et al. [76] as discussed in section 3.2.4.

CHAPTER 4

Methods

4.1 Some definitions about electronic correlations

In the real many-body system each electron interacts with another electron through the instantaneous Coulomb repulsion. The Hamiltonian contains the sum of the pairwise Coulomb interactions, the ground state wave function depends on all of the electronic positions. Changing the position of one electron has an effect on all of the other positions. In other words, the behavior of electrons is correlated. However, a realistic treatment of many-body problem is very complicated, as it would require to find the exact solution of the many-body Hamiltonian. One way to solve the problem is to map the many-body problem of instantaneously interacting particles to single particle interacting with a average potential due to the presence of other particles. This is the way followed in the Hartee-Fock approximation. Thus, historically, as defined by Löwdin, the electron correlation energy is the difference between the exact energy and Hartree-Fock energy, since Hartree-Fock energy contains exact exchange energy but no correlation energy [82, 83].

In quantum chemistry it is usually comfortable to divide correlation energy into two contributions: the dynamic one and nondynamic, or static, one, a division was first proposed by Sinanoğlu [84]. The *Dynamical* correlation energy is a short range effect, related to the tight pair of electrons. The repulsion energy rises when two electrons approach [83].

The *Non-dynamic* correlation effect is related to the energy lowering of the ground state because of the interaction of the HF configuration with low-lying excited states. To be accurately accounted for, it requires multi-determinantal reference wave functions. Non-dynamic correlations have a long range effect [83].

The term strong correlation is used when non-dynamic correlations become dominant [85]. Non-dynamic correlations are essential in the description of such strongly correlated systems like molecules to describe bond dissociation limits; in various transition-metal compounds; diradicals; molecular magnets [85]; and to describe the localized levels of deep-center defects [35].

The multiplet splitting of states that are equivalent by symmetry and thus, degenerate, in the one-electron approximation, is an archetypal example of static correlations. Finally, non-dynamic correlation is considered as a system-specific contribution, whereas dynamic electron correlation is agreed to be a universal contribution [86].

Last but not least, one should be careful about the terminology since the word correlations can be used in a more general sense. These are various correlation functions: a dynamic correlation function describes the correlation between events at different times; a

static correlation function yield a physical property measured or computed with snapshots (in space) of the system [82].

4.2 Treatment of electron correlations with wave function methods

Today, there is no method that is able to simultaneously provide weak (or dynamic) and strong (or static) correlations at low computational cost. Many quantum chemistry wave function based methods have been developed for directly solving the Schrödinger equation. Among them, one can cite the configuration interaction (CI) that is a multi-configurational variational method, the Møller-Plesset second order perturbation correction to the HF energy (MRPT2), the coupled-cluster expansion (CC), the complete active space self-consistent field (CASSCF) that includes static correlations, the complete active space perturbation theory (CASPT2), where the dynamic correlation is a small perturbation of the CASSCF, and the quantum Monte Carlo (MC) method [87]. In principle, it is almost impossible to make a clear cut between dynamic and non-dynamic correlations. However, it is believed that in quantum chemistry methods, a good account of dynamic correlations is insured by the inclusion of multiple configurations (or excitations) to the wave functions, by taking a sum of single Slater determinants, whereas inclusion of multiple references (the reference to which excitations are generated) introduces static correlations [86]. Moreover, these methods are believed to have a straightforward scaling of accuracy, in the sense that inclusion of more excitations or more references will give results converging to the exact solution of the many-body electronic problem. However, because of the coupling between coordinates in the many-electron Schrödinger equation, the computational cost of such methods are usually significant and these techniques are mostly applied to the small molecules.

In the present work, I will compare my results obtained with beyond-DFT methods, as described below, with results obtained with some of the quantum chemistry wave function approach. In particular, I will compare my calculations to the CI, and to the CI combined with constrained RPA (cRPA) of ref. [35] published in the course of my PhD.

In the work [35] various flavors of the CI method have been applied to treat the NV^- center. The main outcome has been the necessity both to treat explicitly static correlations with CI [88] and to include the screening of the Coulomb interaction with the cRPA approach [89].

4.3 Treatment of electron correlations in DFT

The density functional theory (DFT) is a method that is able to account for some static and dynamic correlations via exchange and correlation (XC) functionals with a mean-field computational cost [90]. In principle, the exact exchange and correlation functional should

cover all non-dynamic and dynamic correlation contributions, however, the exact XC functional is not known and the DFT accuracy is based on the approximation used for chosen XC functional. The standard DFT functionals (LDA and GGA) are considered to describe only dynamic correlations [91]. Despite the general success of the local and semilocal approximations for exchange and correlation, limitations and failures of the density functional theory occur for (*i*) the description of systems with localized electrons [92]; (*ii*) the description of the binding energy, which shows up in particular in the evaluation of the band gap of semiconductors [93].

Both failures have been known for a long time and are attributed to the discontinuity of the exchange and correlation potential when the number of electrons in the system is modified [94, 95]. Both kind of limitations will be discussed in the following sections.

4.4 Treatment of electron correlations beyond DFT

4.4.1 The DFT LDA+U and DFT GGA+U approaches

One says that the system is strongly correlated when electrons in the system occupying localized orbitals are penalized with an additional on-site Coulomb repulsion energy term, which adds to the total energy of the system. In such systems the DFT+U method, which ca use both DFT-LDA+U and DFT-GGA+U functionals, can be used [96–99]. The on-site Coulomb interaction U, first introduced by Hubbard [100], has been a parameter that was system dependent, and was different in a bulk element and in its oxide, for instance. Nowadays, the calculation of the Hubbard U can be determined to be consistent with the occupation of the localized orbitals, thus rationalizing the choice of U [101], so that the method does not contain any *ad hoc* parameter.

The method has been well tested for bulk systems with localized d and f orbitals, transition metal (TM) oxides, TM metal silicates, and rare-earth correlated metals [102, 103]. The DFT-LDA+U and DFT-GGA+U are the methods of choice to include part of static correlations. For defects in diamond, however, the localized atomic-like orbitals do not come from the carbon atom, they are generated by the presence of the defect itself. Thus, the method of ref. [103] is not applicable to the NV^- center in diamond, and I had to rely on a different method.

4.4.2 Hybrid functionals

Alternatively, the development of new hybrid functionals is based on an empirical mixing of the orbital-dependent HF and of DFT exchange to obtain a more realistic account of the X energy. Such hybrid functionals contain a part of exact exchange, and thus, correct for the part of self interaction error (see section 4.5.2). Like in the Hartree-Fock method, hybrid functionals produce an increase of the value of the band gap. In diamond, my computed band gap is 4.75 eV too low in GGA, at the respective equilibrium values of the lattice parameter. With the HSE06 hybrid functional, the computed value of the band gap is 5.99

at the equilibrium lattice parameter, with respect to the experimental value of 5.47 eV [104]. Thus, hybrid functionals are known to partly cure the limitation (*ii*) of DFT-LDA and DFT-GGA (see section 4.3).I stress, however, that the HSE06 functional is not able to provide an XC discontinuity when changing the number of particles and thus, is not able to provide a complete remedy to the band gap problem [105].

The use of a hybrid functional has also the non intuitive virtue of providing some improvement of the dynamic correlations. One has to note that generally, there are two empirical parameters of a hybrid functional: the mixing coefficients of the exact exchange part with the exchange in PBE α, and the adjustable screening parameter governing the extent of short-range interactions ω as shown in eq. 4.1.

$$E_{XC}^{hybrid} = \alpha E_X^{HF,SR}(\omega) + (1-\alpha)E_X^{PBE,SR}(\omega) + E_X^{PBE,LR}(\omega) + E_C^{PBE} \tag{4.1}$$

where SR stands for short range, and LR stands for long range.

Many works have demonstrated in recent years that the hybrid functionals can include the screening effectively [92]. For, example, since the HSE06 [106, 107] contains a range-separated potential, it includes a part of the non-local exchange (see eq. 4.1). In this way, one can think that the HSE06 can mimic an effect of the screening of the exchange in the GW being at the same time less computationally expensive.

The use of two parameters can be seen as an approximate treatment of electronic correlations that weakens the direct exchange interaction. It is in this sense that the HSE06 will be used in the present work to improve the DFT-GGA treatment of deep-levels in defected diamond. I did not tune the HSE06 α nor ω parameters and used the standard value α=0.25 and ω=0.106 for the HF and and ω=0.189 for the PBE part [107]. In part II, the HSE06 functional will be used with the Hubbard model (see section 6.2.1).

(4.2)

4.4.3 The *GW* method

Another beyond-DFT method to study insulators with periodic boundary conditions is the *GW* approach [108]. This approach is based on the many-body perturbation theory. Nowadays, it is a most used technique to describe the excitation phenomena in solids. An advantage over the DFT is an accurate inclusion of the screening of the Coulomb interaction.

In particular, the *GW* method is one of the rare methods able to provide the XC discontinuity necessary when changing the number of particles, and is able to accurately predict band gap of semiconductors and insulators when electrons are not localized ones. So the use of the *GW* method could have provided me a good treatment of the band gap of diamond. However, the *GW* method lacks some of the dynamic correlations that are necessary to describe localized electrons, and in particular deep-center levels like those of the NV^- center in diamond. Nevertheless, in the present work, I will compare some of my results with results obtained with *GW* calculations combined with the Hubbard model [34].

4.4.4 Conclusion

A big advantage of the DFT with respect to the wave function theory is the possible extension to big systems with low computational cost. However, contrarily to the wave function theory (WFT), there is no systematic way of improvement of the XC functional, so the accuracy of the many-electron interactions cannot be achieved in a stepwise way [91]. This mostly comes from the different ways in the definitions of the total correlation energy at the DFT and WFT levels of theory.

In this work, I aim to study the manifold of the excited many-body levels of the NV center under pressure. The electronic structure of the NV center contains highly localized in-gap defect-related levels. This fact implies that we need to deal with strongly correlated electrons. At the same time, I seek for the computational cost efficiency because the study of charged defects requires a use of large supercells. In this context the Hamiltonian models have much value. The Hubbard model, developed by James Hubbard [100], is a simple model that addresses the problem of strongly correlated electrons in solids. Its simplicity, however, does not prevent it to predict the complex effects in some correlated systems. So, in this work I will introduce a combined DFT - Hubbard model technique. Special attention will be given to the application of the Hubbard model to the NV center. In the present work I will mainly use the DFT-GGA approach in combination with the Hubbard model. I will compare my results with those obtained with a hybrid functional (see section 4.4.2). By using HSE06 functional, I will improve the description of the dynamic electronic correlations, and the static ones by using the Hubbard model. In the following sections I will briefly discuss the methodology, that will be used in this work, also, I review the state of the art theoretical works.

4.5 Treatment of strongly correlated states of the NV^- defect

The optical properties of the NV center defect are important for its applications. As explained in chapter 2, as an example, the calibration of the pressure dependence of optical fingerprints may allow to use the NV center as a magnetic sensor under high pressure.

In the present section I review some of the recent advances that have been undertaken in the calculations of highly correlated many-body states of the NV^- center from the first principles. I only discuss methods that will be used in this manuscript, the complete reviews of the *ab initio* calculations for defects can be found in refs. [105] [21] and [109].

4.5.1 Caveats

In the present work several theoretical points have to be highlighted before proceeding to application. First, I want to describe all of the low lying many-body states of the NV center. This includes the ground states of NV^- and NV^0, and some of the excited states (see Fig. 3.2.2).

The GS of the NV^- being a triplet state, its $M_s = \pm 1$ projection is a closed-shell system, for which a treatment in DFT-GGA is in principle meaningful. The calculation of all other states requires a deepening of the theoretical arguments before applying a DFT-based method.

4.5.2 The ΔSCF method

a. Principles

The first method is the delta self consistent field method (ΔSCF), which enables one to treat an excitation energy as the difference in total energies of two atomic-like configurations. Indeed, the attempt to obtain excited state energies using time-independent DFT (rather than time-dependent DFT) can be traced back to the demonstration that stationary solutions of the GS functional represent excited states [110, 111]. The ΔSCF method has thus been developed by Ziegler [112] and von Barth [113] for the Hartree-Fock method and for the spin-local density approximation in DFT, respectively. The standard self consistent field is modified at each iteration by imposing the occupation numbers: molecular orbitals of high energy are occupied, while lower in energy orbitals are unoccupied. The ΔSCF method is known to produce reasonable results for excitation energies in atoms and molecules [95, 114].

b. Advantage with respect to the differences in eigenvalues

When one uses differences of Kohn Sham eigenvalues rather than of total energies, self-interaction correction (SIC) is required. Indeed, the main drawback of the DFT is the fact that the DFT Kohn-Sham eigenenergies do not have the physical meaning inherent to the Hartree-Fock eigenenergies. The Kohn-Sham eigenenergies do not correspond to the quasi-particle addition and removal energies. This drawback is coming from the fact that the traditional exchange and correlation functionals (LDA, GGA) suffer from the self-interaction error, i.e. the Hartree energy contains the interaction of the electronic density at $\mathbf{r}$ with itself. In the Hartree-Fock, the exact exchange term exactly cancels the self interaction present in the Hartree energy. This is not the case in DFT-LDA nor DFT-GGA. This is particularly the case for the calculation of ionization potentials obtained from GGA-HOMO Kohn Sham energies [115, 116]. I note that the inclusion of a part of exact-exchange in hybrid functionals corrects for part of the self-interaction error [116]. However, the self-interaction correction is hardly affordable for big systems as those that will be treated in part II of this manuscript.

c. Performance of the ΔSCF method

Finally, some results reported in the litterature have shown that ionization potentials obtained with the ΔSCF method and the HSE06 hybrid functional are superior to those obtained with the ΔSCF method and the PBE functional [116]. The ΔSCF method with

a hybrid functional has also been shown to be the best method for the calculation of ionization potentials with respect to experiment, and to perform even better than the GW method in the simplest one shot application G^0W^0. Therefore, the ΔSCF method with the HSE06 hybrid functional can be the method of choice in my PhD work. I stress, however, that even though, for atomic-like properties, the ΔSCF method is a method of choice, it is not the case for the calculation of band gaps. An approximate form of the ΔSCF method has been extended to compute band gap in solids [117]. However, the GW method remains the method of choice for such calculations.

d. Conclusion

In conclusion, I want to treat a system which demonstrates atomic-like properties in a bulk solid environment. The use of the ΔSCF method in the form of constrained DFT in conjunction with the HSE06 functional is a fair compromise between the accuracy of the description of atomic-like properties (for which the ΔSCF method is a method of choice) and the description of the screening environment (for which the GW method would be the method of choice).

Last but not least, I also stress that even though the ΔSCF method has been initially developed to obtain multi-determinant levels for some atomic configurations [112, 113], it was shown that for the case of strong correlations so they no longer can be described in terms of a reduction of the Slater integrals, the ΔSCF method does not apply [113]. Thus, in the case of my system, one cannot obtain the multi-determinant solutions. I have to combine the ΔSCF method with the Hubbard model to reach this aim. In the present work, the ΔSCF method is used in the form of constrained DFT to compute the mono-determinantal solutions with fixed spin configurations, i.e. the triplet states $^3A_2$ and ^3E of the NV^- center, or the closed-shell singlet state $^1A_1'$ of the NV^- center, lying at high energy.

4.5.3 Mono-determinantal states with constrained DFT

In order to calculate the defect internal optical transitions (see section 2.1.4), one can approximately calculate some excited states with the constrained DFT approach [118].

a. Principles

In this approach the total energy of the excited state is approximated by the total energy of the Kohn-Sham system, where some Kohn-Sham orbitals (KSO) unoccupied and some KSO with higher energy are occupied. These constrained occupations are kept fixed during the self-consistent solution of the Kohn-Sham equations. In this approach it is assumed the change of orbital occupations can mimic an excitation process. As discussed in section 4.5.2, it was shown recently that the self-interaction error can be corrected by the mixing of part of the nonlocal Hartree-Fock exchange with the traditional DFT functional. It was demonstrated that the HSE06 hybrid functional not only brings a significant improvement

in the band gap description of some semiconductors [106, 107], as discussed in section 4.4.2, but also that it enables a very accurate reproduction of the optical transition lines of some defects [119–121]. Therefore, I will use the constrained DFT to describe the excitation processes.

b. Limitations

The constrained DFT approach however has some limitations. Because of the single Slater determinant nature of the DFT it fails to accurately describe the total energies of the states that have a multiconfigurational nature. Thus, for example, one cannot calculate open-shell singlet states with constrained DFT, as they are cannot be represented as a single Slater determinant. In order to understand which states can be represented as a single Slater determinant the use of the group theory is helpful.

c. Group theory analysis

Group theory is a powerful mathematical tool to describe the symmetry properties of crystals. The introduction of a point defect into the crystal lattice produces a reduction of the symmetry. Subsequently, the symmetry of the defect impurity is represented by a subgroup of the original point group of the crystal. According to experimental data, the symmetry of the NV center is C_{3v} [27, 28]. The states near the point defect are localized. Each carbon has a dangling bond σ_i pointing towards the vacancy, and the nitrogen has a lone pair σ_4. These atomic orbitals can be used to construct the symmetry adapted set of molecular orbitals of the defect $\{\psi_r\}$, by the projection technique [122, 123]. In this technique the dangling bonds are projected onto each irreducible representation (IR) of the point group of the defect:

$$\psi_r = P^{(r)}\sigma_i = \frac{l_r}{h}\sum_e \chi_e^{(r)} R_e \sigma_i, \tag{4.3}$$

where $P^{(r)}$ is the projection operator of the IR of index r, $\chi_e^{(r)}$ is the character of the symmetry operation R_e, l_r is the dimension of the IR, h is the number of elements in the group. It has been shown using this technique in ref. [124] that there are 4 single-electron defect-related levels based on the symmetry-adapted linear combination of these dangling bonds. The results of ref. [124] are summarized in Fig. 4.5.3. However, I choose to work with the notations and conventions used in ref. [118]

(a) Atomic orbitals (b) Linear combinations of atomic orbitals (c) Defect molecular orbitals

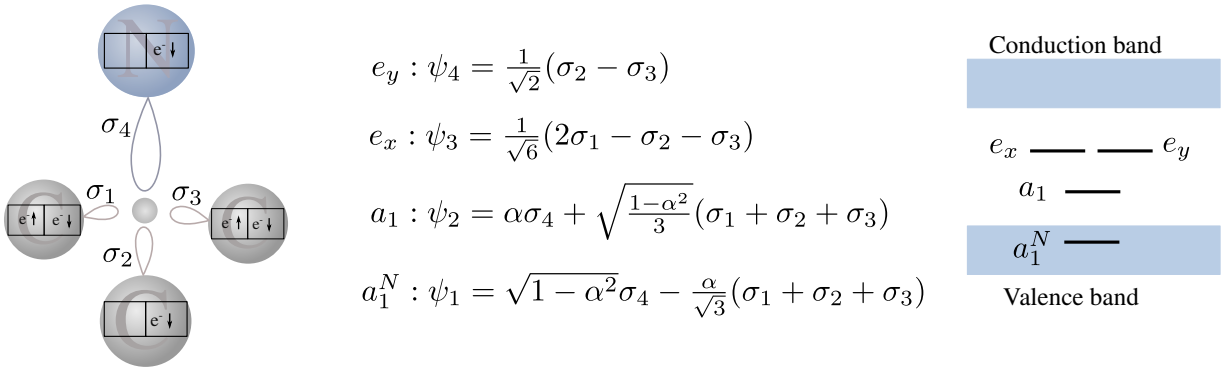

Figure 4.5.1: Molecular model of the NV center. (a) Schematic representation of the dangling bonds pointing towards the vacancy. (b) Symmetry-adapted wavefunctions describing the molecular defect orbitals, constructed as a linear combinations of the dangling bonds; α is a parameter of mixing between the nitrogen lone pair and the carbon dangling bonds. (c) Schematic representation of the molecular defect orbitals. Adapted from [75]

d. Wave function of the many-body states

The energy levels of the defect center are characterized by the number of electrons occupying the orbitals. There are two possible representations: the description of the electrons in the orbitals, or the description of the holes. Both representations are totally equivalent, it is useful to choose the representation with the asmallest number of particles. In the case of the NV^- center, the defect contains 6 electrons, two of them being in the a_1^N resonant state. Three electrons are coming from the carbon dangling bonds, two electrons come from the nitrogen atom, and one is due to the fact that the NV^- center is negatively charged. Finally, the representation of the total many-body wave function can be found by the direct product of the representation of each hole/electron Γ_{hn} and its spin function $D_{1/2}$:

$$\Gamma_\Psi = \prod_n (\Gamma_{hn} \otimes D_{1/2}) \tag{4.4}$$

We summarize the full set of 28 wave functions in table 4.1. With the help of this table I can immediately see which of the many-body states of the NV^- center can be represented as a single Slater determinant, and which states are mixed ones and require the sum of at least two Slater determinants. For example, as we can see from table 4.1, the $M_s = \pm 1$ total spin projections of the $^3A_2$ state are single Slater determinants and thus, can be calculated within the DFT approach by aligning two spin up electrons on the degenerated $e_x e_y$ level to reproduce the total spin $S = 1$. The first excited triplet ^3E can be obtained by promoting one spin down electron from the a_1 level to the $e_x e_y$ level while preserving the total spin, S=1.

Table 4.1: NV^- defect. The full symmetry adapted wave functions of the many-body states are written in the fifth column. Wave functions are written in the hole representation. We note the spin projections in the third column. In the fourth column I indicate which representation transforms as x or y, for the case of doubly degenerate E representations. From ref. [118] and [124].

Configuration	Symmetry	Spin	(x,y)	Wave function
$a_1^N(2)a_1(2)e(2)$	$^3A_2$	1		$\|e_x e_y\rangle$
		0		$\frac{1}{\sqrt{2}}(\|e_x e_y\rangle + \|e_x \bar{e_y}\rangle)$
		-1		$\|\bar{e_x}\bar{e_y}\rangle$
	^1E	0	y	$\frac{1}{\sqrt{2}}(\|\bar{e_x} e_y\rangle - \|e_x \bar{e_y}\rangle)$
		0	x	$\frac{1}{\sqrt{2}}(\|e_x \bar{e_x}\rangle - \|e_y \bar{e_y}\rangle)$
	$^1A_1$	0		$\frac{1}{\sqrt{2}}(\|e_x \bar{e_x}\rangle + \|e_y \bar{e_y}\rangle)$
$a_1^N(2)a_1(1)e(3)$	^3E	1	x	$\|a_1 e_x\rangle$
		1	y	$\|a_1 e_y\rangle$
		0	x	$\frac{1}{\sqrt{2}}(\|\bar{a_1} e_x\rangle + \|a_1 \bar{e_x}\rangle)$
		0	y	$\frac{1}{\sqrt{2}}(\|\bar{a_1} e_y\rangle + \|a_1 \bar{e_y}\rangle)$
		-1	x	$\|\bar{a_1}\bar{e_x}\rangle$
		-1	y	$\|\bar{a_1}\bar{e_y}\rangle$
	$^1E'$	0	x	$\frac{1}{\sqrt{2}}(\|a_1 \bar{e_x}\rangle - \|\bar{a_1} e_x\rangle)$
		0	y	$\frac{1}{\sqrt{2}}(\|a_1 \bar{e_y}\rangle - \|\bar{a_1} e_y\rangle)$
$a_1^N(2)a_1(0)e(4)$	$^1A_1'$	0		$\|a_1 \bar{a_1}\rangle$
$a_1^N(1)a_1(2)e(3)$	$^3E'^N$	1	x	$\|a_1^N e_x\rangle$
		1	y	$\|a_1^N e_y\rangle$
		0	x	$\frac{1}{\sqrt{2}}(\|\bar{a_1}^N e_x\rangle + \|a_1^N \bar{e_x}\rangle)$
		0	y	$\frac{1}{\sqrt{2}}(\|\bar{a_1}^N e_y\rangle + \|a_1^N \bar{e_y}\rangle)$
		-1	x	$\|\bar{a_1}^N \bar{e_x}\rangle$
		-1	y	$\|\bar{a_1}^N \bar{e_y}\rangle$
	$^1E'^N$	0	x	$\frac{1}{\sqrt{2}}(\|a_1^N \bar{e_x}\rangle - \|\bar{a_1}^N e_x\rangle)$
		0	y	$\frac{1}{\sqrt{2}}(\|a_1^N \bar{e_y}\rangle - \|\bar{a_1}^N e_y\rangle)$
$a_1^N(1)a_1(1)e(4)$	$^3A_1^N$	1		$\|a_1^N a_1\rangle$
		0		$\frac{1}{\sqrt{2}}(\|\bar{a_1}^N a_1\rangle + \|a_1^N \bar{a_1}\rangle)$
		-1		$\|\bar{a_1}^N \bar{a_1}\rangle$
	$^1A_1'^N$	0		$\frac{1}{\sqrt{2}}(\|\bar{a_1}^N a_1\rangle - \|a_1^N \bar{a_1}\rangle)$
$a_1^N(0)a_1(2)e(4)$	$^1A_1'^N$	0		$\|a_1^N \bar{a_1}^N\rangle$

4.5.4 Previous works for the mono-determinantal solutions

The constrained DFT (CDFT) method has been previously used to calculate the triplet-triplet $^3E - ^3A_2$ optical transition. Several works have employed CDFT with local and semi-local functionals [6, 118, 125–129], in all the works the $^3E - ^3A_2$ optical ZPL has been

found in the range 1.68-1.8 eV with respect to the experimental value of 1.945 eV [28]. In the refs. [125, 128] the ordering of the low lying many-body states of the NV^- center has been found using the von Barth technique [130] that allows to treat approximately the singlet states in the CDFT.

It has been shown that the most advanced results of the description of the optical transition in CDFT can be achieved by the use of the hybrid functional HSE06. Indeed, several works have shown the ability of the HSE06 functional to reproduce the experimental $^3E - ^3A_2$ optical transition of the NV^- with a great accuracy: 2.02 eV [6], 2.035 eV [129] and 1.955 eV [119].

4.5.5 Multi-determinantal many-body states with the Hubbard model

As we have seen from the previous section, the CDFT approach has an important limitation that does not allow to calculate highly correlated many-body states that have a multi-configurational nature. On the other hand, the CI calculations require a large computational power and are not affordable for large supercell calculations.

Therefore, in the present section I discuss an alternative approach which provides the multi-configurational many-body levels at an affordable computational cost. This approach implies the utilization of the extended Hubbard model. The Hamiltonian of the extended Hubbard model reads:

$$\hat{H} = \sum_{i\sigma} \varepsilon_i \hat{c}^\dagger_{i\sigma}\hat{c}_{i\sigma} - \sum_{i\neq j,\sigma} t_{ij}\hat{c}^\dagger_{i\sigma}\hat{c}_{j\sigma} + \sum_{i\sigma} U\hat{n}^\dagger_{i\uparrow}\hat{n}_{i\downarrow} + \sum_{i>j,\sigma,\sigma'} V\hat{n}^\dagger_{i\sigma}\hat{n}_{j\sigma'} + \sum_{i>j,l>m\sigma,\sigma'} X_{ijlm}\hat{c}^\dagger_{i\sigma}\hat{c}^\dagger_{j\sigma'}\hat{c}_{m\sigma'}\hat{c}_{l\sigma} \tag{4.5}$$

where $\hat{c}^\dagger_{i\sigma}$, $\hat{c}_{i,\sigma}$ are respectively creation and annihilation operators for the electrons, and $\hat{n}^\dagger_{i\sigma}$ is the particle number operator for the electrons. The parameters ε_i, t_{ij}, U, V are respectively on-site energy, hopping energy, on-site Coulomb repulsion term and nearest-neighbor Coulomb repulsion term. X is the exchange interaction term.

An exact diagonalization of this Hamiltonian, in the multi-configurational basis of the dangling bond occupations, allows to find the many-body states of the NV^- center, including the open-shell singlet levels such as ^1E and $^1A_1$.

4.5.6 Vertical excitation in the Hubbard model

In the Hubbard model, the calculated value is a vertical transition energy because in the Hubbard model the change of atomic positions after the excitation is not taken into account.

4.5.7 Previous works for the multi-determinantal solutions

In ref. [75] Ranjbar *et al.* have calculated the Hubbard model parameters by direct calculation of the interaction integrals in the local basis of the defect orbitals with the

BLYP hybrid XC functional, i.e. the t_{ij} was calculated as (in atomic units):

$$t_{ij} = \int \varphi *_i (r)[-\frac{1}{2} \bigtriangledown^2 + V(r)]\varphi_j(r) d^3r, \tag{4.6}$$

where $\varphi_i(r)$ and $\varphi_j(r)$ are the dangling orbitals of the NV from the single-electron DFT calculations. The Coulomb interaction parameters were obtained as (in atomic units):

$$X_{ijlm} = \int \varphi *_i (r)\varphi *_j (r') \frac{1}{|r - r'|} \varphi_l(r)\varphi_m(r') d^3r d^3r', \tag{4.7}$$

where X_{ijlm} with indices (X_{iiii}) was U_i, with indices $(Xiijj)$ was V_{ij} and the remaining part was the exchange part.

With the Hubbard parameters calculated in such a way, they have found a value of the $^3E - ^3A_2$ vertical transition of 2.38 eV, 0.18 eV higher than the experimental value of 2.20 eV [28]. As for the singlet-singlet $^1A_1 - ^1E$ vertical energy transition, they have found a value of 0.61 eV, the experimental value of the vertical excitation for $^1A_1 - ^1E$ transition is unknown. Their vertical transition can be tentatively compared to the $^1A_1 - ^1E$ ZPL of 1.19 eV [131].

In ref. [34] Choi *et al.* have studied the NV^- center with the extended Hubbard model, however, the exchange part X has been neglected in their work. Also, Choi *et al.* have used a different method to calculate the Hubbard model parameters. The tight-binding parameters in ref. [34] have been found by the construction of the maximally localized Wannier functions. Then, the interaction parameters U and V have been found by fitting the quasi-particle energies from the diagonalization of the Hubbard Hamiltonian to the quasi-particle energies found with a GW calculations. Choi *et al.* have found a value of the $^3E - ^3A_2$ vertical transition of 2.1 eV. Also, they have found a value of the $^1A_1 - ^1E$ vertical transition around 0.8-1.0 eV. There is no experimental data to compare with. I note that the experimental ZPL is 1.19 eV [131].

In the course of my PhD work, the results of Choi *et al.* have been compared to more advanced methods in ref. [35]. Bockstedte *et al.* have combined Configuration Interaction (CI) with constrained Random Phase Approximation (cRPA) in order to account for the screening of the interaction between highly correlated defect levels. The CI method alone turned out to be insufficient. The results will be discussed in the part II.

These results indicate that both static correlation effect of the localized dangling bonds and the dynamic screening effects must be taken into account in order to describe the open-shell singlet states of the NV^- point defect accurately. They also tend to prove that the Hubbard model is sufficient to account for static correlations.

4.5.8 Conclusion

In the present work I will address the highly correlated many-body states of the NV^- center with the Hubbard model. The multi-configurational basis set will enable me to treat the static correlation effects. Also, I will introduce a new approach to parameterize

the Hubbard model through the fitting to total energy differences calculated with the hybrid HSE06 functional in the framework of ΔSCF method. The use of the HSE06 functional will enable me to treat non-local screening effects, like in GW, and thus, to improve the description of the environment. It will also enable me to improve the dynamic correlations and to partly correct the self-interaction error of my atomic-like system, i.e. the deep levels in the gap introduced by the point defect.

4.6 Treatment of strongly correlated states of the NV^0 defect

Contrarily to the NV^- center case, there was only a small number of theoretical studies of the many-body states of the NV^0 center.

4.6.1 Mono-determinantal states with constrained DFT

To the best of my knowledge, there is only one work where the CDFT has been applied to the neutral NV^0 center. In ref. [74] Gali *et al.* have calculated the $^4A_2 - ^2E$ energy difference of the NV^0 center. Gali *et al.* have shown that the single Slater determinants $a_1^N(2)a_1(2)e_x(1)$ and $a_1^N(2)a_1(2)e_y(1)$ are the true orthonormal eigenstates of the ^2E ground state of the C_{3v} point group and thus can be calculated with CDFT. In order to calculate the $^4A_2$ state a single Slater determinant can be constructed by aligning all electrons with spin up in the configuration $a_1^N(2)a_1(1)e(2)$ to obtain $M_s = +3/2$. Their calculated energy difference $^4A_2 - ^2E$ was 0.86 eV.

In the present work, I are interested in the optical transitions of the NV^0 center. It has been found experimentally, that the optical transition in the neutral NV^0 center occurs between $^2A_2$ and ^2E doublet states [76]. However, the $^2A_2$ state is a highly correlated state that cannot be calculated in CDFT. Thus, more advanced techniques are needed.

4.6.2 Multi-determinantal many-body states with the Hubbard model

Using the 4-site Hubbard model, with parameters calculated through the direct calculation of interaction integrals in the local basis, Ranjbar *et al.* [75] have predicted the following ordering of the many-body states: $^2E^{GS}$, $^4A_2$, $^2A_1$, ^2E, $^2A_1$, ^2E. Their $^4A_2$ was situated 0.68 eV above the ground state, which is 0.22 eV lower than the value predicted with CDFT by Gali *et al.* [74]. The experimental value is, however, unknown. In the ref. [75] Ranjbar *et al.* have assigned the optical transition to the $^2A_1 - ^2E$ one, which is in a disagreement with the recent experimental results [76] where the optical transition has been assigned to the $^2A_2 - ^2E$. I will discuss this issue in part II.

4.7 Conclusion

The limited number of theoretical works does not allow to reflect on the many-body states ordering nor to make robust conclusions about the optical transition. In Fig. 4.7.1 I summarize the theoretical knowledge ath the beginning of my PhD work, as well the data that have been reported during the PhD. Indeed, the field is moving rapidly.

In the case of the NV^- center the theoretical works seem to agree with experimental data (see Fig 3.2.2) and one with another. However, in the case of the NV^0 center, some theoretical works contradict one another. For instance, Zyubin *et al.* [132] and Ranjbar *et al.* [75] do not agree about the symmetry of the first excited doublet state. Zyubin *et al.* have found the first excited doublet state of $^2A_2$ symmetry which is in a good agreement with the recent experimental assignment of the optical transition in the NV^0 [76]. However, the theoretical work of Zyubin *et al.* does not predict the existence of the intermediate quartet state $^4A_2$. While Ranjbar *et al.* predict the existence of the quartet state, however, the symmetry of their first excited doublet state $^2A_1$ seems to be in disagreement with the experimental assignment. Both works seem to be in agreement with each other for the three following states lying higher in energy. Since, those works are the two only theoretical works that have studied the neutral NV^0 center, it is difficult to draw a conclusion on the ordering of the low lying many-body states.

Moreover, my aim is to study the behavior of the many-body states of NV^0 under a hydrostatic pressure. Thus, more investigations are needed in the case of the neutral NV^0 center. As for the case of the NV^-, center I am going to use the Hubbard model parameterized by fitting it to the DFT-PBE or DFT-HSE06 total energies. However, as explained, there is only a small number of many-body states of the NV^0 center that can be calculated in DFT. One should mention, that in ref. [75] the Hubbard parameters for NV^- and NV^0 were very similar except for the exchange and the on-site Coulomb repulsion. In my model, I neglect the exchange interaction and I will make an approximation, using the same Hubbard model parameters for NV^- and NV^0. I will show in part II that this approximation is reasonable in order to study the pressure behavior of the many-body states.

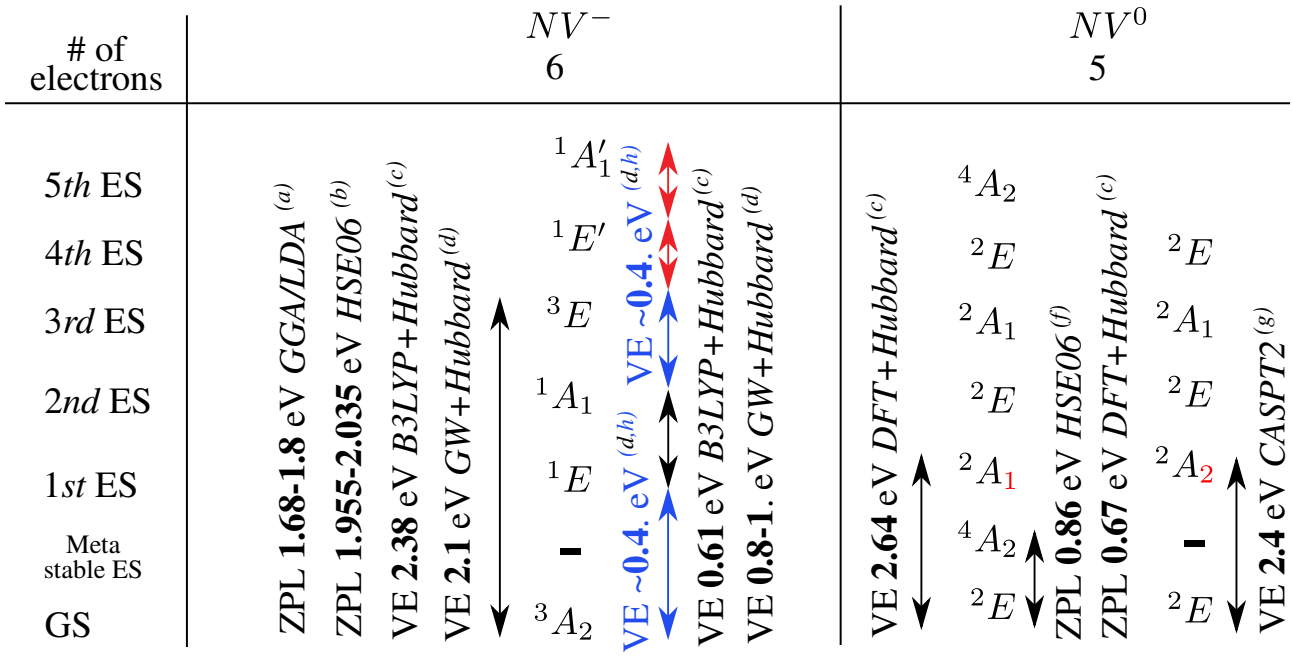

Figure 4.7.1: Electronic structure of the NV^- and NV^0 center from the theoretical point of view at the beginning of my PhD. Elements highlighted in blue color have been determined theoretically during the course of my PhD work. Quantities highlighted in red color are still to be determined. In particular, the discrepancy in the symmetry of excited doublet state of the NV^0 between the refs. [132] and [75] is highlighted in red color. The relative positioning of the singlet levels with respect to the triplet levels in the NV^- center is highlighted in blue color as calculated in ref. [34] and confirmed by a recent calculation in ref. [35] that has been performed in the course of my PhD. See Fig. 3.2.2 for analog from the experimental point of view. (a) Values are taken from refs. [6, 118, 125–129]. (b) Values are taken from refs. [6, 119, 129]. (c) Value is taken from ref. [75]. (d) Value is taken from ref. [34]. (f) Value is taken from ref. [74]. (g) Value is taken from ref. [132]. (h) Value is taken from ref. [35]

Part II

Theoretical results

CHAPTER 5

Treatment of correlations in DFT

In this chapter, I present the method with which I will calculate the difference $E_{TOT}(^3E) - E_{TOT}(^3A_2)$, where E_{TOT} is the total energy of the system in the ^3E and $^3A_2$ configurations of the NV^- center in diamond. I study both ZPL and VE transitions as defined in sections 2.1.4 (b) and 2.1.4 (c). I use the DFT calculations as defined in section 4.5.3 and I study the effect of the supercell size and functionals DFT-LDA, DFT-PBE and DFT-HSE06 on the $E_{TOT}(^3E) - E_{TOT}(^3A_2)$ ZPL. I discuss the importance of the correlations for the calculations of the ZPL. I discuss also some technical problems related to the open-shell configuration calculations in DFT. I then apply a hydrostatic pressure and study the behavior of the aforementioned ZPL and VE transitions. Finally, I compare my results with the experimental studies. Last but not least, I conclude on the validity of the DFT calculations used in the pressure dependence investigations and I conclude on the methodology that will be used for further investigations in the next chapter.

5.1 Computational details

If not mentioned otherwise the results obtained in this chapter have been performed with the QUANTUM ESPRESSO package [133, 134] in the 128-atom supercell (4×4×4 2-atom fcc cell, with a_{lat}=6.79 (a.u.)) with the 222 Monkhorst Pack [135] **k**-points sampling. The cutoff energy was 40 Ry. The normconserving pseudopotentials [136] used for the calculations have been developed in the present work (details about the pseudopotential can be found in the Appendix 8.1). The need of the development of the normconserving pseudopotentials has been linked with the issue of the utilization of the available in the database [137] ultrasoft pseudopotentials [138] with the HSE06 functional in the QUANTUM ESPRESSO package. The issue manifested into the huge computational load. The calculations have been performed with DFT-LDA, DFT-PBE and HSE06 functionals. In the case of HSE06 functional I have used the standard value of the parameters (see section 4.4.2) and the three-dimensional mesh for q-points (k_1-k_2) sampling of the Fock operator has been set to nq_{x1}=nq_{x2}=nq_{x3}=1. In the case of the charged cell in a periodic calculation a compensating jellium background is inserted to remove divergences. The atomic positions in the supercell containing the defect were relaxed for each functional with the convergence threshold of 0.001 (a.u.).

5.2 DFT modeling of the monodeterminantal states

Fig. 5.2.1 shows a schematic representation of the defect-related levels in the gap. $^3A_2$ is the ground state, ^3E is a low lying excited-state, for these levels their $M_s = \pm 1$ can be represented as a single Slater determinant and thus, can be calculated within the DFT approach as discussed in chapter 4. The understanding of whether the state can or cannot be represented as a single-Slater determinant can be obtained from the group theory by constructing the total wave function of the state. In the case of the NV^- a detailed analysis has been performed in ref. [124], as discussed in section 4.5.3.

In order to calculate the total energy corresponding to the $^3A_2$ ground state, and to the ^3E excited state of NV^-, we fill the levels in the gap with the electrons in the ways shown in figure 5.2.1. The ground state triplet is constructed by aligning two spin-up electrons in the degenerated $e_x e_y$ state to reproduce the total spin $S = 1$. The first excited triplet is obtained by promoting one spin-down electron from the a_1 state to the $e_x e_y$ state by preserving the total spin. In order to find the energy transition, I calculate the difference between the corresponding total energies $E_{TOT}(^3E) - E_{TOT}(^3A_2)$. When both total energies are computed at the equilibrium atomic positions of the $^3A_2$ configuration, I compare my result to the vertical excitation, as defined in section 2.1.4 (c). When the total energies are computed at their respective equilibrium atomic positions, I compare my result to the zero phonon line as defined in section 2.1.4 (b).

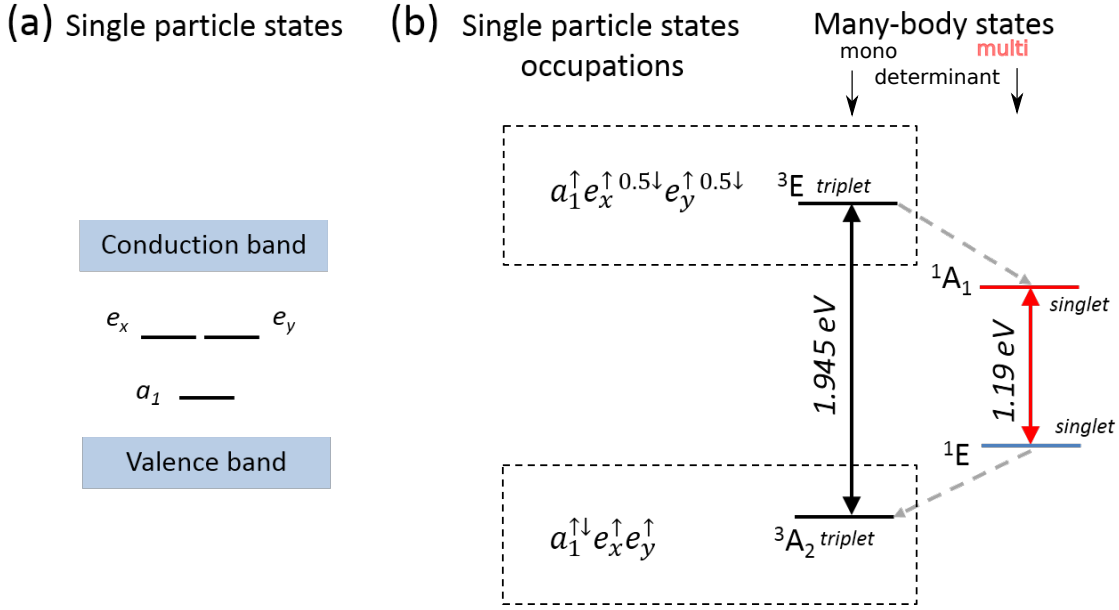

Figure 5.2.1: The NV^- center. (a) Schematic representation of the defect-related levels in the band gap, adapted from ref. [30], same as Fig. 2.1.1 (b). (b) Constrained occupations of the single particle levels in the gap in order to calculate the many-body ground state and excited state. The a_1^N level is occupied with 2 electrons, being a resonant state.

5.3 Open-shell calculation problem

In the case of the ^3E state, however, an additional problem arises. Indeed, since the $e_x e_y$ state is two-fold degenerated, spin-down electron occupies either the e_x or e_y orbital, and both cases should give the same energy of the many-body state. However, the treatment of the open-shell configurations with the orbital degeneracy is a complex case for the DFT calculations and is still an open methodological question. Many new methods have been developed in order to treat this problem, among them the ground state ensembles Kohn-Sham theory [139] or the multi-configurational DFT [140]. Because of this problem, in the DFT-PBE calculations, the convergence of the ^3E state is slow with respect to the calculation of the $^3A_2$ state. I observe in my calculations that the convergence of the state occurs with a spurious breaking of the degeneracy of the $e_x e_y$ level everywhere (except at the **k**-point $\frac{1}{4}\frac{1}{4}\frac{1}{4}$ of my calculation). An even greater problem occurs in the HSE06 functional calculations. The problem occurs since the HSE06 explicitly depends on the orbitals, the convergence of the ^3E state become impossible. To avoid the problem of the convergence, I have chosen a strategy to perform restricted calculations with fractional occupations [105, 141]. Therefore, in order to calculate the total energy of the ^3E state, I equally occupy e_x and e_y level by a half of the spin-down electron. This technique preserves the $e_x e_y$ degeneracy.

5.4 Calculation of the ZPL and VE

In this chapter, I investigate both the vertical excitation line between $^3E - ^3A_2$ and the zero-phonon line between $^3E - ^3A_2$. In order to describe the vertical excitation with our DFT method, I impose the electron occupations corresponding to the excited state and I fix the atomic coordinates to those that correspond to the ground state equilibrium configuration. Then, I calculate the energy difference between the total energy of the $^3A_2$ ground state and of the vertically excited one ^3E.

In order to calculate the zero phonon line, I impose the electronic occupations corresponding to the excited state and I allow atoms to relax inside a supercell. Then I calculate the energy difference between the total energy of the $^3A_2$ ground state in its equilibrium atomic configuration and the excited state total energy ^3E in the relaxed configuration.

5.5 Impact of the supercell size on the ZPL and VE

I first study the influence of the supercell size and functionals on the zero phonon line for the $^3E - ^3A_2$ transition. Fig. 5.5.1 shows the ZPL for the $^3E - ^3A_2$ transition as a function of the supercell size. As one can see, for the $^3E - ^3A_2$ transition within DFT-PBE the curve saturates for the supercell size of 512-atoms, which yields a ZPL value for the transition $^3E - ^3A_2$ transition equal to 1.728 eV, which is underestimated with respect to the experiment 1.945 eV. In Fig. 5.5.1 I also compare my PBE ZPL to other theoretical

calculations [18], [127] and [119], which were performed with the DFT-PBE. As one can see, my DFT-PBE results are in agreement with other theoretical works. I conclude that,

- first, there is a size effect on the ZPL which can be eliminated for sufficiently large supercells with the size starting from 216 - 512-atoms.
- second, there is a common trend of the PBE functional to underestimate an internal defect transition energy along with the band gap energy.

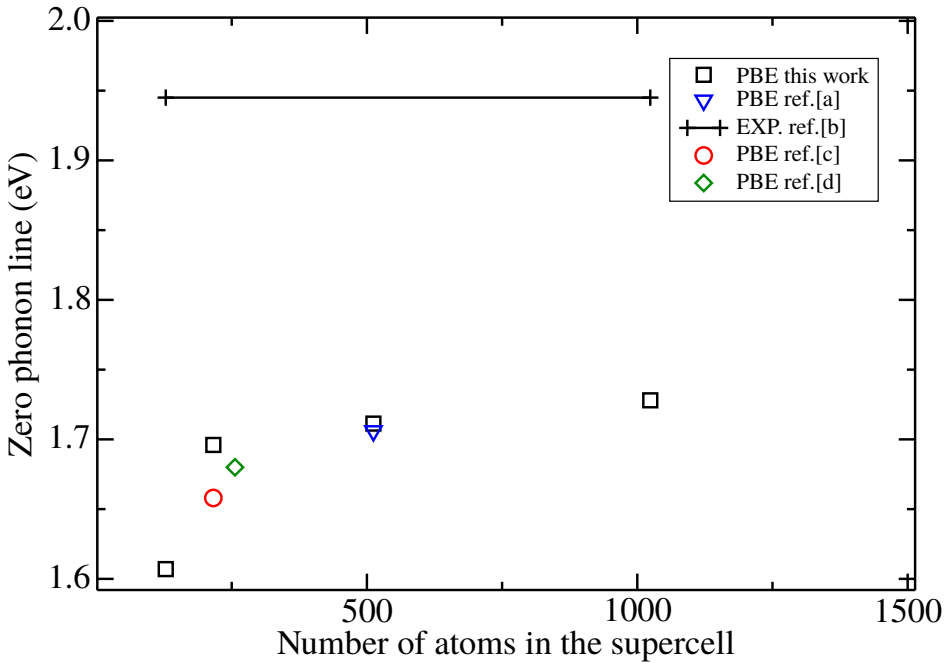

Figure 5.5.1: NV^- center. Experimental ${}^3E - {}^3A_2$ ZPL [17] and ZPL calculated within DFT-PBE as a function of the supercell size; ref a,b [119]; ref c [18]; ref d [127].

5.6 Impact of the functionals

Although the size effect is eliminated starting from the 512-atom cell, in order to limit the computational cost I consider the 128-atom supercell, which I found to be the only feasible one with HSE06 to perform repeated calculations at various pressures, and being also the one that is big enough to weaken the spurious interaction of the charge in the neighboring unit cells. Indeed, I checked that the defect-related bands in the gap are almost flat for the 128-atom fcc supercell.

I study the effect of the exchange-correlation functional on the behavior of the system under a hydrostatic pressure. I apply the hydrostatic pressure to the system by varying the lattice parameter of the cubic fcc supercell. In order to calculate the ZPL, the atomic coordinates are allowed to relax inside the supercell at each pressure. Fig. 5.6.1 shows a comparison of the experimental ZPL [17] between the triplet states as a function of the pressure with my calculated ZPL both with the DFT-LDA, DFT-PBE and DFT-HSE06 functionals. If we consider first the ambient pressure, one can see, that the DFT-PBE underestimates the absolute value of the photoluminescence line - 1.703 eV, whereas DFT-HSE06 overestimates the absolute value of the photoluminescence - 2.13 eV with respect to the experimental 1.945 eV. The discrepancy in my HSE06 result with respect to the experimental value might come from the supercell size effect. It has been recently shown, that the HSE06 hybrid functional provides not only a more accurate value of the band gap energy for some semiconductors [106, 107], but also the ZPL in the NV^- center in the 512-atom supercell [119] (the black triangle in Fig.5.6.1).

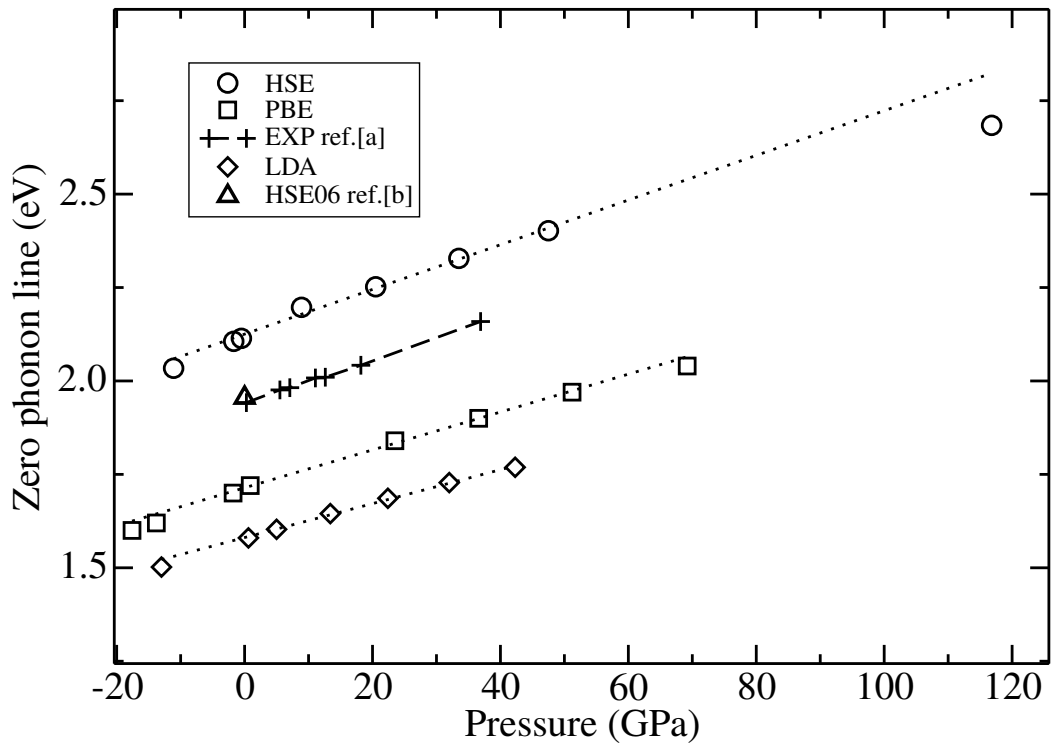

Figure 5.6.1: NV^- center. Experimental $E(^3E) - E(^3A_2)$ ZPL as a function of pressure, extracted from [17] and ZPL calculated within DFT-PBE, DFT-LDA and HSE06 in a 128-atom fcc supercell.

This is explained by the fact that the mixing of the PBE with the Hartree-Fock exact exchange improves the overall exchange and correlation. In particular, HSE06 allows to go beyond the standard DFT and to mimic the self-interaction correction (see sections 4.4.2 and 4.5.2 (b)).

5.7 Results: pressure effect on ZPL

As my goal is to study the effect of the hydrostatic pressure of the zero phonon line of the $E(^3E) - E(^3A_2)$ transition which implies the repeated calculations of the ground state and excited state total energies with the subsequent relaxation of atomic coordinates at each pressure. Such a task would demand an important computational power if done in the 512-atom supercell with the HSE06 functional. If we, however, concentrate only on the pressure behavior and not on the absolute value of the transition energy, I will show that the 128-atom cell is a reasonable compromise between the computational cost and the precision. Table 5.1 compares the pressure gradients of the ZPL calculated with different functionals with the experiment. I mention, however, that at high pressures (130 GPa), the behavior of the ZPL deviates from the linear one.

Table 5.1: NV^- center. Comparison of the pressure gradients (meV/GPa).

Exp. 1 [17]	**Exp. 2 [16]**	**LDA**	**PBE**	**HSE06**
5.75	5.5	4.5	5.0	5.9

As one can see, all functionals reproduce with a good agreement the experimental pressure gradient of the ZPL. The LDA functional reproduces the experimental pressure gradient within an error of 22%, PBE within 13% and HSE06 within a -2% error. One should mention that the fitting has been performed in the range 0-50 GPa, the range corresponding to the available experimental data. In such a way, I show that even though the 128 supercell calculations suffer from the size effect, the pressure coefficient is well reproduced.

5.8 Results: pressure effect on ZPL vs VE

I now investigate the behavior of the vertical excitation between $^3E - ^3A_2$ as a function of the applied pressure. The Fig. 5.8.1 illustrates the comparison of the vertical and the zero phonon lines calculated with the PBE and HSE06 functionals. I find that the vertical excitation is higher in energy than the ZPL, with the Stokes shift at zero pressure of 0.23 eV. I, also, get that the Stokes shift slightly increases as a function of the pressure as we can see that from the values of the pressure gradients in the Table 8.1. One can conclude, that the pressure behavior of the vertical excitation and ZPL has the same order of magnitude.

However, the ionic relaxations reduce the pressure coefficient by 0.9 meV/GPa, i.e. ~13-15 % for both PBE and HSE06 functionals.

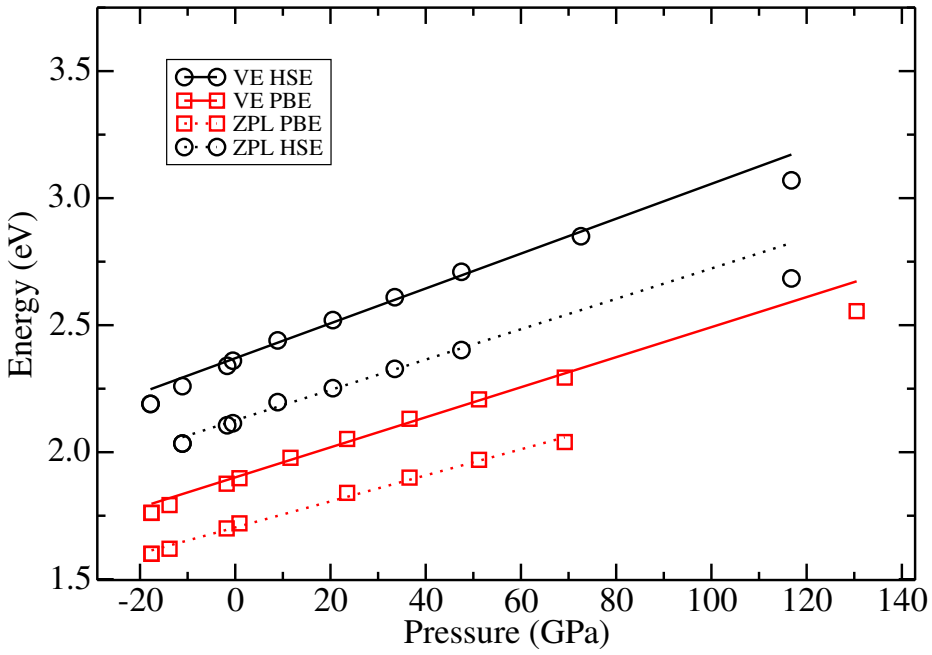

Figure 5.8.1: NV^- center. Comparison of the ZPL and vertical excitation within PBE and HSE06.

Table 5.2: NV^- center. Comparison of the pressure gradients of ZPL and VE(meV/GPa).

	Exp. 1 [17]	**Exp. 2 [16]**	**LDA**	**PBE**	**HSE06**
ZPL	5.75	5.5	4.5	5.0	5.9
VE	-	-	-	5.9	6.8

5.9 Conclusions

I would like to sum up some important conclusions of this chapter. First of all, I show that the DFT calculations, whatever the functional, reproduce the pressure gradient of the $E(^3E) - E(^3A_2)$ optical transition. The most accurate result is obtained using the HSE06 hybrid functional. However, in order to reproduce the absolute value of the energy

transition one should properly account for the electron correlations. The use of the HSE06 is crucial here. Even though the absolute value of the optical transition depends on the functional and is sensitive to the supercell size, I show that the DFT total energy method is a rather good reference to study the pressure behavior of the system. This is an important conclusion because in the next chapter I will show that the energy transitions calculated in the DFT can be used in order to parameterize the Hubbard model. I will show, that more mono-determinantal excited states higher in energy can be calculated in constrained DFT. This will give me enough references to fit the parameters of the Hubbard model. The Hubbard model will give me the possibility to study multi-determinantal excited states that are not accessible with the DFT calculation.

CHAPTER 6

Treatment of correlations with the Hubbard model: theoretical developments

In this chapter I apply the extended Hubbard model to the negatively charged NV^- and to the neutral NV^0 center, in order to model multi-determinant states, which cannot be obtained by the DFT modeling. I introduce the new 3-site model for the NV center and I compare it to the conventional 4-site model [34, 75]. I provide both analytical and numerical solutions for the two models. I demonstrate that the low-lying excited states of the NV center obtained with the two models are the same. The 3-site model contains less parameters than the 4-site model and thus requires less references to fit the parameters. I introduce the new technique to parameterize the Hubbard model using DFT total energies. Finally, I compare the many-body excited states obtained by my Hubbard model with the state-of-the art theoretical methods.

6.1 The Hubbard model and the *hubbardcode*

In this work, I aim to study the manifold of the excited many-body levels of the NV center. The electronic structure of the NV center contains highly localized in-gap defect-related levels. This fact implies I need to deal with strongly correlated electrons. The Hubbard model, developed by James Hubbard [100] is a simple model that addresses the problem of strongly correlated electrons in solids (see section 4.5.5). In order to model electron-electron and ion-electron interactions I employ the extended Hubbard model Hamiltonian:

$$\hat{H} = \sum_{i\sigma} \varepsilon_i \hat{c}^\dagger_{i\sigma}\hat{c}_{i\sigma} - \sum_{i\neq j,\sigma} t_{ij}\hat{c}^\dagger_{i\sigma}\hat{c}_{j\sigma} + \sum_{i\sigma} U\hat{n}^\dagger_{i\uparrow}\hat{n}_{i\downarrow} + \sum_{i>j,\sigma,\sigma'} V\hat{n}^\dagger_{i\sigma}\hat{n}_{j\sigma'}, \tag{6.1}$$

where $\hat{c}^\dagger_{i\sigma}$, $\hat{c}_{i,\sigma}$ are creation and annihilation operators, $\hat{n}^\dagger_{i\sigma}$ is a particle number operator. Parameters ε_i, t_{ij}, U, V are respectively on-site, hopping energies, on-site Coulomb repulsion and nearest-neighbor Coulomb repulsion. Fig. 6.2.2 schematically demonstrates the meaning of these parameters: the hopping parameter t_{CC} is the probability of the electron to transfer from one site to another with spin conservation, ε_C is the energy that an electron possesses when occupying the carbon site. On-site Coulomb repulsion occurs between the electrons of different spins. The nearest-neighbor Coulomb repulsion contains interactions

between all spins.

In this chapter I will consider 3- and 4-site Hubbard models in order to study the *NV* center. In order to construct the Hamiltonian of the considered system I use a fortran code that I have developed during my PHD work - the *hubbardcode*. The general algorithm of the code is the following. The python script constructs a multi-electron basis set for the chosen number of electrons and sites. The code constructs the Hamiltonian in the multi-electron basis by performing the action of the second quantization operators on the basis functions. When the Hamiltonian is constructed, the code writes as output the Hamiltonian in the matlab or python format, so the subsequent analytical diagonalization is possible with the python sympy library of in the Matlab software using symbolic tools. For the numeric diagonalization I use the ScaLAPACK linear algebra library. In the last part of the code, I perform the fit procedure for the parameterization of the Hamiltonian parameters, as will be explained in the next sections. The code also performs the symmetry analysis of the resulting eigenfunctions. Fig. 6.1.1 represents the workflow of the code.

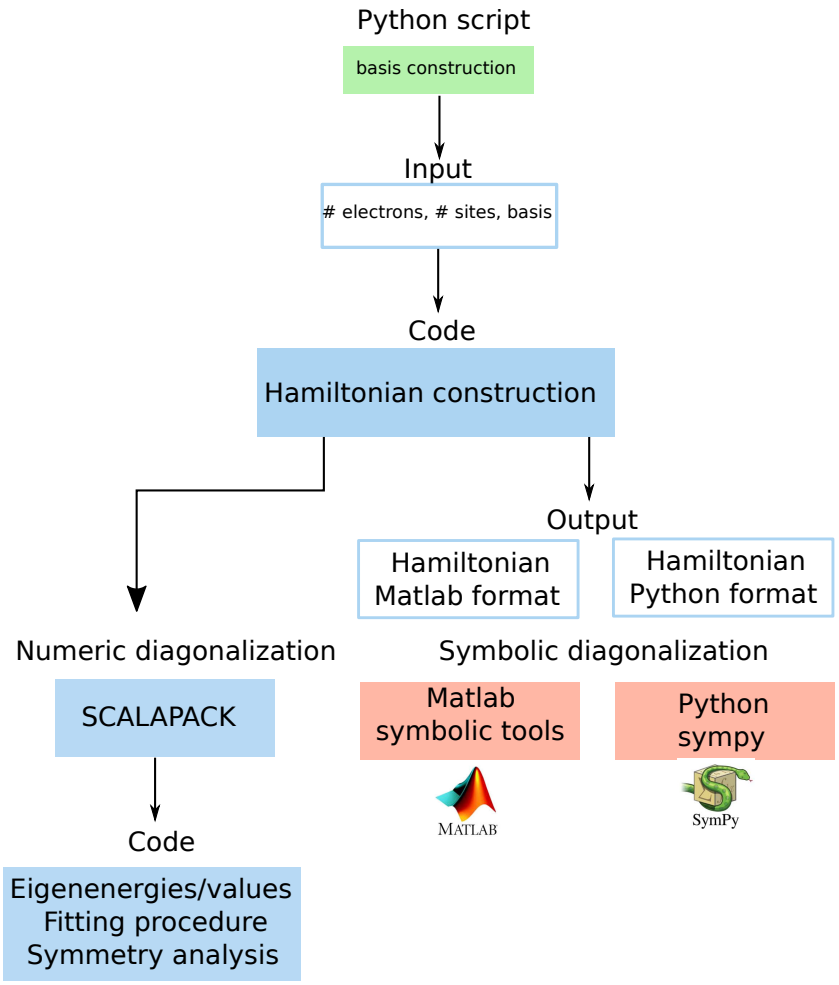

Figure 6.1.1: Workflow of the *hubbard* code.

6.2 The Hubbard model for the NV^- center

6.2.1 The 3-site Hubbard model

a. State of the art

In this work, I adopt a strategy to model the NV^- center as a defect molecule and to construct the Hubbard model to model the multi-determinant many-body states. This means that I consider only the nearest neighbors to the vacancy both in this section and in section 6.2.2. In the other works, where the NV center has been studied with the Hubbard model [34, 75], the 4 atoms around the vacancy have been taken into account: 3 carbons atoms and the nitrogen atom. This choice is dictated by the picture of the unsatisfied bonds. Each carbon has a dangling bond pointing towards the vacancy and the nitrogen has a lone pair (see section 4.5.3 (c)). Using the group theory projection technique [122, 123] it has been shown in ref. [124] that there are 4 single-electron defect-related levels based on the symmetry-adapted linear combination of these dangling bonds. It has also been shown in ref. [124] using symmetry and charge considerations that the nitrogen related single-electron level should be the lowest in energy among those 4 levels. The DFT calculations [118] have shown eventually that, indeed, there are 3 single-electron levels that are located in the electronic band gap, however, the nitrogen-related level is situated in the valence band. I confirm this result with my DFT calculations. It was also shown experimentally and with *ab initio* calculations that the greatest contribution to the defect orbitals comes from the nearest neighbor carbon atoms to the vacancy [49, 118, 126, 142]. I confirm these results by calculating the projections of the wave functions onto the atomic orbitals, indeed, I find that the nitrogen atomic wave functions have a very small projection onto the single-electron a_1 level located in the band gap. Fig. 6.2.1 illustrates the defect-related single-electron levels.

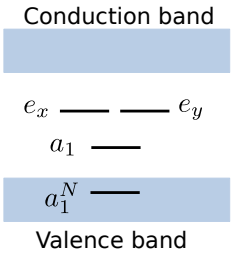

Figure 6.2.1: Schematic representation of the single-electron defect-related levels, which are the linear combinations of the atomic orbitals of the nearest neighboring atoms to the vacancy. Same as Fig. 2.1.1 (b).

b. Method

Based on these results I have decided to neglect the nitrogen and to use 3-site model. Thus, I will consider only 3 carbon atoms around the vacancy in the 3-site Hubbard model. One

should mention that the vacancy is modeled by the absence of a site, so the electrons are allowed to stay on carbon sites only. In the spirit of the original Hubbard model, there is one orbital per site, which can host two electrons of different spin by the Pauli principle. Fig. 6.2.2 schematically represents my system.

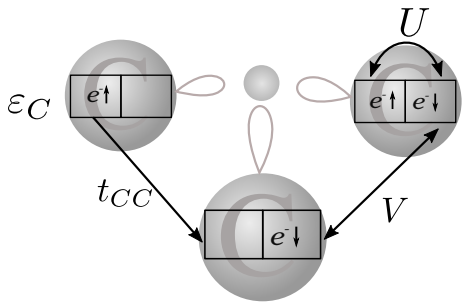

Figure 6.2.2: Schematic representation of the 3-site Hubbard model. Large grey balls are the sites which model carbon atoms. The small light grey ball is a vacant site. Each site can host spin-up and spin-down electron, this is indicated with the black squares.

According to the electron counting, we have to distribute 4 electrons among 3 sites. Three electrons are coming from the carbon dangling bonds and one is due to the fact that the NV^- center is negatively charged. Therefore, our multi-electron Fock space basis set contains 15 basis functions. They are constructed as all possible combinations for 4 electrons to occupy 6 spin orbital sites ($C_4^6 = 15$).

The multi-electron basis reads:

$$
\begin{aligned}
\phi_1 &= |0\ \uparrow\downarrow\ \uparrow\downarrow\rangle & S &= 0 \\
\phi_2 &= |\uparrow\ \uparrow\ \uparrow\downarrow\rangle & S &= 1 \\
\phi_3 &= |\uparrow\ \downarrow\ \uparrow\downarrow\rangle & S &= 0 \\
\phi_4 &= |\uparrow\ \uparrow\downarrow\ \uparrow\rangle & S &= 1 \\
\phi_5 &= |\uparrow\ \uparrow\downarrow\ \downarrow\rangle & S &= 0 \\
\phi_6 &= |\downarrow\ \uparrow\ \uparrow\downarrow\rangle & S &= 0 \\
\phi_7 &= |\downarrow\ \downarrow\ \uparrow\downarrow\rangle & S &= -1 \\
\phi_8 &= |\downarrow\ \uparrow\downarrow\ \uparrow\rangle & S &= 0 \\
\phi_9 &= |\downarrow\ \uparrow\downarrow\ \downarrow\rangle & S &= -1 \\
\phi_{10} &= |\uparrow\downarrow\ 0\ \uparrow\downarrow\rangle & S &= 0 \\
\phi_{11} &= |\uparrow\downarrow\ \uparrow\ \uparrow\rangle & S &= 1 \\
\phi_{12} &= |\uparrow\downarrow\ \uparrow\ \downarrow\rangle & S &= 0 \\
\phi_{13} &= |\uparrow\downarrow\ \downarrow\ \uparrow\rangle & S &= 0 \\
\phi_{14} &= |\uparrow\downarrow\ \downarrow\ \downarrow\rangle & S &= -1 \\
\phi_{15} &= |\uparrow\downarrow\ \uparrow\downarrow\ 0\rangle & S &= 0
\end{aligned}
\tag{6.2}
$$

where I indicate the total spin of the basis function in the right column. The same basis can be represented in the matrix form as it is implemented in the *hubbardcode*, that I have developed during my PhD work. In the matrix the columns correspond to sites. Two columns are reserved per site. Every first position per site is reserved for majority spins, every second - for minority spins.

$$\Phi = \begin{pmatrix} 0 & 0 & 1 & 1 & 1 & 1 \\ 1 & 0 & 1 & 0 & 1 & 1 \\ 1 & 0 & 0 & 1 & 1 & 1 \\ 1 & 0 & 1 & 1 & 1 & 0 \\ 1 & 0 & 1 & 1 & 0 & 1 \\ 0 & 1 & 1 & 0 & 1 & 1 \\ 0 & 1 & 0 & 1 & 1 & 1 \\ 0 & 1 & 1 & 1 & 1 & 0 \\ 0 & 1 & 1 & 1 & 0 & 1 \\ 1 & 1 & 0 & 0 & 1 & 1 \\ 1 & 1 & 1 & 0 & 1 & 0 \\ 1 & 1 & 1 & 0 & 0 & 1 \\ 1 & 1 & 0 & 1 & 1 & 0 \\ 1 & 1 & 0 & 1 & 0 & 1 \\ 1 & 1 & 1 & 1 & 0 & 0 \end{pmatrix} \tag{6.3}$$

I obtain the following Hubbard Hamiltonian for my 3-site system using the *hubbardcode*:

$$H = \begin{pmatrix} \mathscr{E}_1 & 0 & t & 0 & t & -t & 0 & -t & 0 & 0 & 0 & 0 & 0 & 0 & 0 \\ 0 & \mathscr{E}_2 & 0 & t & 0 & 0 & 0 & 0 & 0 & 0 & -t & 0 & 0 & 0 & 0 \\ t & 0 & \mathscr{E}_2 & 0 & t & 0 & 0 & 0 & 0 & t & 0 & 0 & -t & 0 & 0 \\ 0 & t & 0 & \mathscr{E}_2 & 0 & 0 & 0 & 0 & 0 & 0 & t & 0 & 0 & 0 & 0 \\ t & 0 & t & 0 & \mathscr{E}_2 & 0 & 0 & 0 & 0 & 0 & 0 & t & 0 & 0 & t \\ -t & 0 & 0 & 0 & 0 & \mathscr{E}_2 & 0 & t & 0 & -t & 0 & -t & 0 & 0 & 0 \\ 0 & 0 & 0 & 0 & 0 & 0 & \mathscr{E}_2 & 0 & t & 0 & 0 & 0 & 0 & -t & 0 \\ -t & 0 & 0 & 0 & 0 & t & 0 & \mathscr{E}_2 & 0 & 0 & 0 & 0 & t & 0 & -t \\ 0 & 0 & 0 & 0 & 0 & 0 & t & 0 & \mathscr{E}_2 & 0 & 0 & 0 & 0 & t & 0 \\ 0 & 0 & t & 0 & 0 & -t & 0 & 0 & 0 & \mathscr{E}_1 & 0 & t & -t & 0 & 0 \\ 0 & -t & 0 & t & 0 & 0 & 0 & 0 & 0 & 0 & \mathscr{E}_2 & 0 & 0 & 0 & 0 \\ 0 & 0 & 0 & 0 & t & -t & 0 & 0 & 0 & t & 0 & \mathscr{E}_2 & 0 & 0 & t \\ 0 & 0 & -t & 0 & 0 & 0 & 0 & t & 0 & -t & 0 & 0 & \mathscr{E}_2 & 0 & -t \\ 0 & 0 & 0 & 0 & 0 & 0 & -t & 0 & t & 0 & 0 & 0 & 0 & \mathscr{E}_2 & 0 \\ 0 & 0 & 0 & 0 & t & 0 & 0 & -t & 0 & 0 & 0 & t & -t & 0 & \mathscr{E}_1 \end{pmatrix} \tag{6.4}$$

where I replaced t_{CC} by t for simplicity and used the following conventions:

$$\begin{aligned} \mathscr{E}_1 &= 2U + 4V + 4\varepsilon_C \\ \mathscr{E}_2 &= U + 5V + 4\varepsilon_C \end{aligned} \tag{6.5}$$

I first present the analytical solution of this problem.

c. Analytical solution

Before we diagonalize the Hamiltonian 6.4, one can make some simplifications. The subtraction of a constant from the diagonal of the Hamiltonian can reduce the number of non-zero elements and parameters of the Hamiltonian and save the time of the symbolic diagonalization which is usually more time consuming than the numerical one. Also, this operation can give us an important insight about the model. In my case, I decide to subtract the value of $\mathscr{E}_2$ from the diagonal of the Hamiltonian: $H - \mathscr{E}_2 I$. One can easily see that this subtraction reduces the Hamiltonian to two non-zero parameters: t and $U - V$. This gives us the clue that the final eigenenergies will depend only on these quantities. One should mention that we should add the same constant afterwards to obtain the final eigenenergies. However, the addition of the constant will only shift the absolute values of the final eigenenergies. So, with this analysis one can already obtain some information about the behavior of our model. In fact, this tells us that my model has only 3 independent parameters: t, $U - V$ and ε_C , where ε_C only shifts the manifold of the many-body states.

The following simplification can be further undertaken. One can bring the Hamiltonian to the block-diagonal form due to its intrinsic symmetry. It can be shown that the Hamiltonian commutes with the total spin projection M_s, so it is a conserved quantity. Thus, only elements situated at the intersection of the same M_s projections will be non-zero. In order to bring my Hamiltonian to a block-diagonal form I employ the Cuthil-McKee technique to reduce the bandwidth of the sparse symmetric matrix [143] as implemented in the Matlab software. Fig. 6.2.3 shows a simplified form of the initial Hamiltonian. Non-zero terms are represented as colored points. I then rewrite the same Hamiltonian in the block-diagonal form as explained. The blocks represent spin projections respectively M_s: 0, 1, -1,

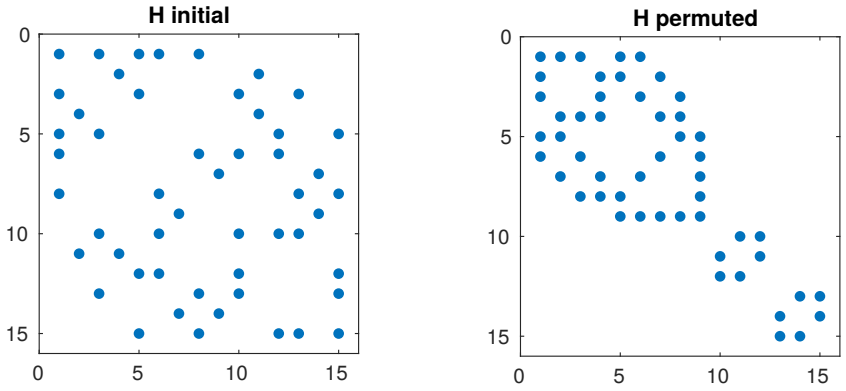

Figure 6.2.3: The 3-site Hubbard model. Schematic representation of the initial Hamiltonian and the same Hamiltonian in the block-diagonal form.

where two blocks corresponding to M_s=1,-1 are the same and equal to:

$$\begin{pmatrix} 0 & -t_{\rm CC} & t_{\rm CC} \\ -t_{\rm CC} & 0 & t_{\rm CC} \\ t_{\rm CC} & t_{\rm CC} & 0 \end{pmatrix} \tag{6.6}$$

and the sub-block with M_s=0 is:

$$\begin{pmatrix} ({\rm U}-{\rm V}) & -t_{\rm CC} & t_{\rm CC} & 0 & -t_{\rm CC} & t_{\rm CC} & 0 & 0 & 0 \\ -t_{\rm CC} & 0 & 0 & -t_{\rm CC} & t_{\rm CC} & 0 & t_{\rm CC} & 0 & 0 \\ t_{\rm CC} & 0 & 0 & t_{\rm CC} & 0 & t_{\rm CC} & 0 & t_{\rm CC} & 0 \\ 0 & -t_{\rm CC} & t_{\rm CC} & ({\rm U}-{\rm V}) & 0 & 0 & -t_{\rm CC} & t_{\rm CC} & 0 \\ -t_{\rm CC} & t_{\rm CC} & 0 & 0 & 0 & 0 & 0 & -t_{\rm CC} & -t_{\rm CC} \\ t_{\rm CC} & 0 & t_{\rm CC} & 0 & 0 & 0 & -t_{\rm CC} & 0 & t_{\rm CC} \\ 0 & t_{\rm CC} & 0 & -t_{\rm CC} & 0 & -t_{\rm CC} & 0 & 0 & -t_{\rm CC} \\ 0 & 0 & t_{\rm CC} & t_{\rm CC} & -t_{\rm CC} & 0 & 0 & 0 & t_{\rm CC} \\ 0 & 0 & 0 & 0 & -t_{\rm CC} & t_{\rm CC} & -t_{\rm CC} & t_{\rm CC} & ({\rm U}-{\rm V}) \end{pmatrix} \tag{6.7}$$

The eigen function coefficient matrix is (for the sake of simplicity, the eigenvectors are *not* normalized, but they are orthogonal)

$$C = \begin{pmatrix} 0 & 0 & 0 & 0 & 0 & 0 & 0 & 0 & 0 & 1 & 1 & -\frac{f}{2t} & 0 & -\frac{g}{2t} & 0 \\ 1 & 0 & 0 & 1 & 0 & 0 & -1 & 0 & 0 & 0 & 0 & 0 & 0 & 0 & 0 \\ 0 & 1 & 0 & 0 & 1 & 0 & 0 & -1 & 0 & \frac{b}{8t} & -\frac{c}{8t} & 0 & -\frac{g}{4t} & 0 & -\frac{f}{4t} \\ -1 & 0 & 0 & 1 & 0 & 0 & 0 & 0 & 0 & 0 & 0 & 0 & 0 & 0 & 0 \\ 0 & -1 & 0 & 0 & 1 & 0 & 0 & 0 & 0 & \frac{b}{8t} & -\frac{c}{8t} & 1 & \frac{g}{4t} & 1 & \frac{f}{4t} \\ 0 & 1 & 0 & 0 & 1 & 0 & 0 & -1 & 0 & -\frac{b}{8t} & \frac{c}{8t} & 0 & \frac{g}{4t} & 0 & \frac{f}{4t} \\ 0 & 0 & 1 & 0 & 0 & 1 & 0 & 0 & -1 & 0 & 0 & 0 & 0 & 0 & 0 \\ 0 & -1 & 0 & 0 & 1 & 0 & 0 & 0 & 0 & -\frac{b}{8t} & \frac{c}{8t} & -1 & -\frac{g}{4t} & -1 & -\frac{f}{4t} \\ 0 & 0 & -1 & 0 & 0 & 1 & 0 & 0 & 0 & 0 & 0 & 0 & 0 & 0 & 0 \\ 0 & 0 & 0 & 0 & 0 & 0 & 0 & 0 & 0 & 1 & 1 & \frac{f}{2t} & -1 & \frac{g}{2t} & -1 \\ 1 & 0 & 0 & 0 & 0 & 0 & 1 & 0 & 0 & 0 & 0 & 0 & 0 & 0 & 0 \\ 0 & 1 & 0 & 0 & 0 & 0 & 0 & 1 & 0 & \frac{b}{8t} & -\frac{c}{8t} & -1 & 0 & -1 & 0 \\ 0 & 1 & 0 & 0 & 0 & 0 & 0 & 1 & 0 & -\frac{b}{8t} & \frac{c}{8t} & 1 & 0 & 1 & 0 \\ 0 & 0 & 1 & 0 & 0 & 0 & 0 & 0 & 1 & 0 & 0 & 0 & 0 & 0 & 0 \\ 0 & 0 & 0 & 0 & 0 & 0 & 0 & 0 & 0 & 1 & 1 & 0 & 1 & 0 & 1 \end{pmatrix} \tag{6.8}$$

Here I have used the following notations

$$\begin{aligned} a &= (U-V)^2 - 4(U-V)t + 36t^2 \\ b &= U - V - 2\,t + \sqrt{a} \\ c &= -(U-V) + 2\,t + \sqrt{a} \\ d &= (U-V)^2 + 2(U-V)t + 9t^2 \\ f &= U - V + t - \sqrt{d} \\ g &= U - V + t + \sqrt{d} \end{aligned} \tag{6.9}$$

The total spin of the system in a state i can be found as

$$S_i = S_{basis}^T |C|^2, \tag{6.10}$$

where S_{basis} is a matrix which contains the spins of the *basis* states and $|C|^2$ is the coefficient matrix C in which all the element are squared (not to confuse with $C \times C$). This $|C|^2$ matrix contains the weight of each state in each site.

The eigenenergies (where I added $\mathscr{E}_2$ that was subtracted in the beginning) and total spins of states are

Total spin	Total energy	Total energy if $U = V = 0$
$S_1 = 1$	$E_1 = U + 5\,V + 4\,\varepsilon - 2\,t$	$4\varepsilon - 2t$
$S_2 = 0$	$E_2 = U + 5\,V + 4\,\varepsilon - 2\,t$	$4\varepsilon - 2t$
$S_3 = -1$	$E_3 = U + 5\,V + 4\,\varepsilon - 2\,t$	$4\varepsilon - 2t$
$S_4 = 1$	$E_4 = U + 5\,V + 4\,\varepsilon + t$	$4\varepsilon + t$
$S_5 = 0$	$E_5 = U + 5\,V + 4\,\varepsilon + t$	$4\varepsilon + t$
$S_6 = -1$	$E_6 = U + 5\,V + 4\,\varepsilon + t$	$4\varepsilon + t$
$S_7 = 1$	$E_7 = U + 5\,V + 4\,\varepsilon + t$	$4\varepsilon + t$
$S_8 = 0$	$E_8 = U + 5\,V + 4\,\varepsilon + t$	$4\varepsilon + t$
$S_9 = -1$	$E_9 = U + 5\,V + 4\,\varepsilon + t$	$4\varepsilon + t$
$S_{10} = 0$	$E_{10} = \frac{3\,U}{2} + \frac{9\,V}{2} + 4\,\varepsilon + t - \frac{\sqrt{a}}{2}$	$4\varepsilon - 2t$
$S_{11} = 0$	$E_{11} = \frac{3\,U}{2} + \frac{9\,V}{2} + 4\,\varepsilon + t + \frac{\sqrt{a}}{2}$	$4\varepsilon + 4t$
$S_{12} = 0$	$E_{12} = \frac{3\,U}{2} + \frac{9\,V}{2} + 4\,\varepsilon - \frac{t}{2} - \frac{\sqrt{d}}{2}$	$4\varepsilon - 2t$
$S_{13} = 0$	$E_{13} = \frac{3\,U}{2} + \frac{9\,V}{2} + 4\,\varepsilon - \frac{t}{2} - \frac{\sqrt{d}}{2}$	$4\varepsilon - 2t$
$S_{14} = 0$	$E_{14} = \frac{3\,U}{2} + \frac{9\,V}{2} + 4\,\varepsilon - \frac{t}{2} + \frac{\sqrt{d}}{2}$	$4\varepsilon + t$
$S_{15} = 0$	$E_{15} = \frac{3\,U}{2} + \frac{9\,V}{2} + 4\,\varepsilon - \frac{t}{2} + \frac{\sqrt{d}}{2}$	$4\varepsilon + t$

(6.11)

The differences of eigenenergies with respect to the ground state energy are

Energy	Degeneracy	Symmetry
$\Delta E_1 = 0$	$(g = 3)$	${}^3A_2$
$\Delta E_2 = 3\,t$	$(g = 6)$	${}^3E$
$\Delta E_3 = \frac{1}{2}(U - V) + 3\,t - \frac{\sqrt{a}}{2}$	$(g = 1)$	${}^1A_1$
$\Delta E_4 = \frac{1}{2}(U - V) + 3\,t + \frac{\sqrt{a}}{2}$	$(g = 1)$	${}^1A_1$
$\Delta E_5 = \frac{1}{2}(U - V) + \frac{3\,t}{2} - \frac{\sqrt{d}}{2}$	$(g = 2)$	${}^1E$
$\Delta E_6 = \frac{1}{2}(U - V) + \frac{3\,t}{2} + \frac{\sqrt{d}}{2}$	$(g = 2)$	${}^1E$

(6.12)

The analysis of the analytical solution brings us to the following important conclusions:

- The *difference* between the triplet levels (from 1 to 9) in eq. (6.11) does not depend on U nor V, but the absolute value does.
- The *difference* between the singlet levels depends on $(U - V)$ and t.
- All the levels contain the ε parameter in the form 4ε. So, changing ε will just *shift* all the levels in the same manner.
- None of the model parameters (ε, t, U, V) changes the triplet eigenstates (the columns of the C matrix: C_{ij}, where $1 < j < 9$), which is not the case for the triplet energies.

We have seen that all the variables in the C matrix and the eigenenergies depend only on the difference $U - V$. This could be initially seen from the form of the Hamiltonian as has been discussed in the beginning of section 6.2.2 (b). If we take the difference of the diagonal terms of the Hamiltonian, we will get: $\mathscr{E}_1 - \mathscr{E}_2 = U - V$. This provides a huge time saving of the exact diagonalization of the Hamiltonian because we reduce the number of variables from four (ε, U, V, t) to two $(U - V, t)$. This is especially important in the case where we want to perform a symbolic diagonalization for large systems. One should remember, however, that using this procedure implies we are only interested in the differences of eigenenergies. One can find the absolute eigenenergies to adding back the term $\mathscr{E}_2$ that we subtracted out of the diagonal of the Hamiltonian.

In eq. (6.11) in the case when we put $U = V = 0$ in the resulting many-body eigenenergies we have the following degeneracies g of levels:

$$\begin{aligned} g(4\varepsilon - 2t) &= 6 \\ g(4\varepsilon + t) &= 8 \\ g(4\varepsilon + 4t) &= 1 \end{aligned} \tag{6.13}$$

In fact, when we neglect electron-electron interactions we obtain the limit case of a non-interacting system with many electrons. One can see, that degeneracies are increased with respect to the interacting system, so at the end we have only three levels. One can say that we have downfolded the many-electron system to an effective non-interacting system. The same connection might be done starting from "bottom-up", from the single-electron system, described in the next section.

d. The single electron case

In the single electron case, we simply have only one electron hosted by 3 carbon sites. Thus, the single electron basis is:

$$\begin{aligned}
\phi_1^{(1)} &= |\uparrow\ 0\ 0\rangle & S &= 1/2 \\
\phi_2^{(1)} &= |0\ \uparrow\ 0\rangle & S &= 1/2 \\
\phi_3^{(1)} &= |0\ 0\ \uparrow\rangle & S &= 1/2 \\
\phi_4^{(1)} &= |\downarrow\ 0\ 0\rangle & S &= -1/2 \\
\phi_5^{(1)} &= |0\ \downarrow\ 0\rangle & S &= -1/2 \\
\phi_6^{(1)} &= |0\ 0\ \downarrow\rangle & S &= -1/2
\end{aligned} \tag{6.14}$$

Or, in the matrix form,

$$\Phi^{(1)} = \begin{pmatrix} 1 & 0 & 0 & 0 & 0 & 0 \\ 0 & 0 & 1 & 0 & 0 & 0 \\ 0 & 0 & 0 & 0 & 1 & 0 \\ 0 & 1 & 0 & 0 & 0 & 0 \\ 0 & 0 & 0 & 1 & 0 & 0 \\ 0 & 0 & 0 & 0 & 0 & 1 \end{pmatrix} \tag{6.15}$$

The single electron Hamiltonian in this system is

$$H^{(1)} = \begin{pmatrix} \varepsilon & -t & -t & 0 & 0 & 0 \\ -t & \varepsilon & -t & 0 & 0 & 0 \\ -t & -t & \varepsilon & 0 & 0 & 0 \\ 0 & 0 & 0 & \varepsilon & -t & -t \\ 0 & 0 & 0 & -t & \varepsilon & -t \\ 0 & 0 & 0 & -t & -t & \varepsilon \end{pmatrix} \tag{6.16}$$

We obtain eigenfunctions coefficient matrix by the diagonalization (since this system is much simpler than the multielectron one, we can write the *normalized* and orthogonal eigenvectors)

$$C^{(1)} = \begin{pmatrix} -\frac{\sqrt{2}}{2} & -\frac{\sqrt{2}}{2} & 0 & 0 & \frac{\sqrt{3}}{3} & 0 \\ \frac{\sqrt{2}}{2} & 0 & 0 & 0 & \frac{\sqrt{3}}{3} & 0 \\ 0 & \frac{\sqrt{2}}{2} & 0 & 0 & \frac{\sqrt{3}}{3} & 0 \\ 0 & 0 & -\frac{\sqrt{2}}{2} & -\frac{\sqrt{2}}{2} & 0 & \frac{\sqrt{3}}{3} \\ 0 & 0 & \frac{\sqrt{2}}{2} & 0 & 0 & \frac{\sqrt{3}}{3} \\ 0 & 0 & 0 & \frac{\sqrt{2}}{2} & 0 & \frac{\sqrt{3}}{3} \end{pmatrix} \tag{6.17}$$

The single electron eigenenergies are:

$$\begin{array}{ll} \text{Total spin} & \text{Total energy} \\ S_1^{(1)} = 1/2 & E_1^{(1)} = \varepsilon + t \\ S_2^{(1)} = 1/2 & E_2^{(1)} = \varepsilon + t \\ S_3^{(1)} = -1/2 & E_3^{(1)} = \varepsilon + t \\ S_4^{(1)} = -1/2 & E_4^{(1)} = \varepsilon + t \\ S_5^{(1)} = 1/2 & E_5^{(1)} = \varepsilon - 2\,t \\ S_6^{(1)} = -1/2 & E_6^{(1)} = \varepsilon - 2\,t \end{array} \tag{6.18}$$

which can be represented with the following schema:

$$(\uparrow)E_1^{(1)}, (\uparrow)E_2^{(1)}, (\downarrow)E_3^{(1)}, (\downarrow)E_4^{(1)} \text{—} \quad \text{—}$$

$$(\uparrow)E_5^{(1)}, (\downarrow)E_6^{(1)} \qquad \text{—}$$

As denoted in 6.18 spin-up and down projection energies $E_5^{(1)}$ and $E_6^{(1)}$ correspond to the lowest defect-related single-electron level as shown in the schema above, whereas the $E_{1-4}^{(1)}$ eigenenergies correspond to the two-fold degenerate single-electron state which is higher in energy. So, in order to obtain a non-interacting many-body energy using single-electron energies of eq. (6.18) one should sum these energies as many times as the number of electrons we want to put in the corresponding state of the schema. Now we can "build" the multielectron states *in the framework* of the single-electron states. So, we have six electron levels (or three if we incorporate the spin) and we need to place four electrons on these six levels. The total energy of a state will be just the sum of single electron energies. In the following table I show all 15 non-interacting many-electron states constructed in this way. One can see that at the end we obtain the same three levels, with the same degeneracies and the same energies as in the case where we started from the many-electron system 6.11.

N	Configuration	Energy	Total spin
1	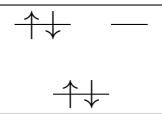	$E_5^{(1)} + E_6^{(1)} + E_1^{(1)} + E_3^{(1)} = 4\varepsilon - 2t$	S=0
2	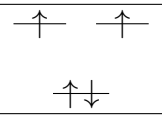	$E_5^{(1)} + E_6^{(1)} + E_1^{(1)} + E_2^{(1)} = 4\varepsilon - 2t$	S=1
3	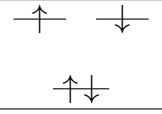	$E_5^{(1)} + E_6^{(1)} + E_1^{(1)} + E_4^{(1)} = 4\varepsilon - 2t$	S=0
4	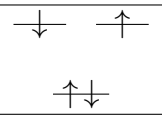	$E_5^{(1)} + E_6^{(1)} + E_3^{(1)} + E_2^{(1)} = 4\varepsilon - 2t$	S=0
5	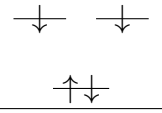	$E_5^{(1)} + E_6^{(1)} + E_3^{(1)} + E_4^{(1)} = 4\varepsilon - 2t$	S=-1
6	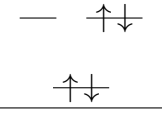	$E_5^{(1)} + E_6^{(1)} + E_2^{(1)} + E_4^{(1)} = 4\varepsilon - 2t$	S=0
7	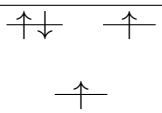	$E_5^{(1)} + E_1^{(1)} + E_3^{(1)} + E_2^{(1)} = 4\varepsilon + t$	S=1
8	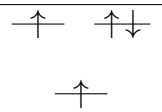	$E_5^{(1)} + E_1^{(1)} + E_2^{(1)} + E_4^{(1)} = 4\varepsilon + t$	S=1
9	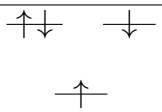	$E_5^{(1)} + E_1^{(1)} + E_3^{(1)} + E_4^{(1)} = 4\varepsilon + t$	S=0
10	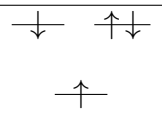	$E_5^{(1)} + E_3^{(1)} + E_2^{(1)} + E_4^{(1)} = 4\varepsilon + t$	S=0
11	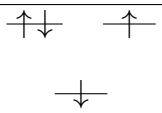	$E_6^{(1)} + E_1^{(1)} + E_3^{(1)} + E_2^{(1)} = 4\varepsilon + t$	S=0
12	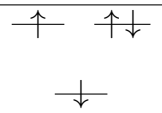	$E_6^{(1)} + E_1^{(1)} + E_2^{(1)} + E_4^{(1)} = 4\varepsilon + t$	S=0
13	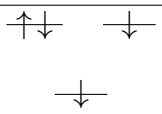	$E_6^{(1)} + E_1^{(1)} + E_3^{(1)} + E_4^{(1)} = 4\varepsilon + t$	S=-1
14	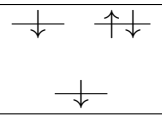	$E_6^{(1)} + E_3^{(1)} + E_2^{(1)} + E_4^{(1)} = 4\varepsilon + t$	S=-1
15	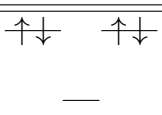	$E_1^{(1)} + E_3^{(1)} + E_2^{(1)} + E_4^{(1)} = 4\varepsilon + 4t$	S=0

e. Analytical parameterization

In the present work I am interested in studying the energy transitions between low-lying many-body states of the NV center, notably $E(^3E)-E(^3A_2)$, $E(^1A_1)-E(^1E)$, and compare them to the experimental findings. Since I am interested only in energy differences, as I have shown earlier, my 3-site model is reduced to two parameters: t and $U-V$. Since the 3-site model is a relatively simple model, I have an analytical solution of the energy differences 6.12.

On the other hand, in the previous chapter 5, I have shown that some of these energy transitions can be calculated from the DFT. These are energy transitions between states that can be represented as a single Slater determinant. /degenar

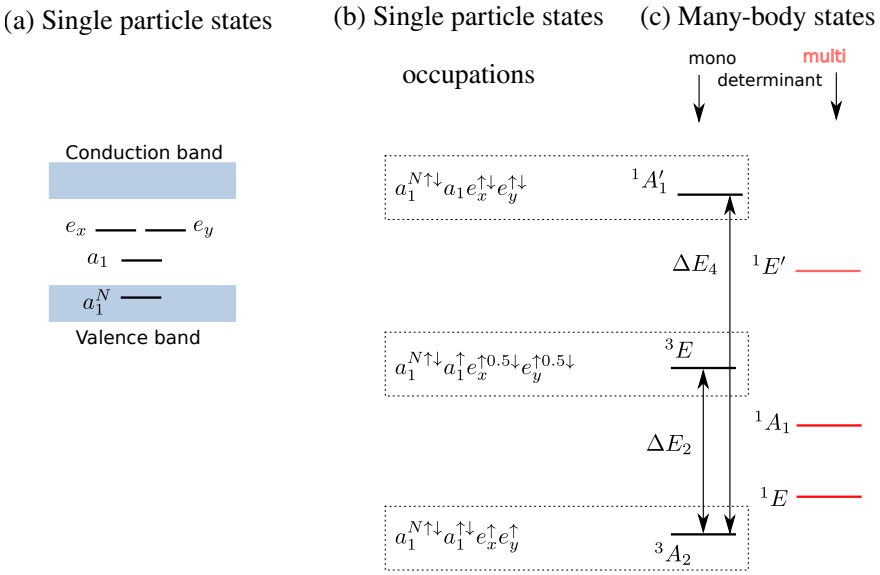

Figure 6.2.4: (a) Schema of the single-electron levels of the NV center in the band gap. Same as Fig. 2.1.1 (b). (b) Occupations of the single-electron levels of panel (a) corresponding to the many-body state in panel (c). (c) Many-body levels of the NV^- center that can be found from 3-site model. Levels that can be represented as a single Slater determinant are in the left column, the multi-determinant ones are in the right column.

The 3-site model results in 15 eigenstates. Taking into account their degeneracies, it gives us 6 many-body states of the following symmetries: $^3A_2$, ^1E, $^1A_1$, ^3E, $^1E'$, $^1A_1'$. I note that the prime symbol in the symmetry notation is just to distinguish the levels of the same symmetry, but those with the prime are of higher energy. Among these 6 levels, only 3 can be calculated with the DFT. They are the $^3A_2$ and the ^3E $M_s=\pm 1$ projections, as discussed in the previous chapter. Another level is a closed-shell singlet $^1A_1'$. This state is calculated by promoting all electrons from the lowest in-gap a_1 level to the e_xe_y levels. Fig. 6.2.4 (b) shows the constrained occupations that have to be imposed in order to calculate these levels in DFT.

So, the idea of my approach is to calculate two reference energy transitions from DFT and to associate them with the corresponding energy transition in the Hubbard model. This gives us two equations with two unknown variables t and $U - V$. In this way I associate the Hubbard energy transitions ΔE_2 and ΔE_4 from 6.12 to the DFT total energy differencies:

$$\Delta E_2 = E_{TOT}(^3E) - E_{TOT}(^3A_2) \tag{6.19}$$
$$\Delta E_4 = E_{TOT}(^1A_1') - E_{TOT}(^3A_2) \tag{6.20}$$

Substituting the energy values from 6.11, we get

$$\Delta E_2 = 3t \tag{6.21}$$
$$\Delta E_4 = \frac{(U-V)}{2} + 3\,t + \frac{\sqrt{(U-V)^2 - 4\,(U-V)\,t + 36\,t^2}}{2}. \tag{6.22}$$

It is seen that the ΔE_2 triplet-triplet transition depends only on the t parameter and the ΔE_4 triplet-singlet transition depends on t and on $(U - V)$. Since I can find only one parameter among U and V, I put V artificially to zero. Then I find the parameters t and U from the DFT energies ΔE_2 and ΔE_4 in the following way:

$$t = \frac{1}{3}\Delta E_2 \tag{6.23}$$
$$U - V = \frac{{\Delta E_4}^2 - 6\,\Delta E_4\,t}{\Delta E_4 - 4\,t} \tag{6.24}$$

f. Numerical parameterization

One should mention that it is not always possible to obtain the full analytical expressions of the parameters as a function of the DFT energies. As I will show, it is not possible in the case of the 4-site model. Another way to parameterize the Hamiltonian is to perform a numeric fit of t and $U - V$ to the DFT transitions. Such a fit procedure has been implemented in the *hubbardcode*. The strategy is the standard one, I start with some guess parameters and I fit the Hubbard levels to the corresponding DFT transitions until they coincide within e.g. 1 meV error. In the fit procedure, as an error ctriterion, I have taken a root-mean square error:

$$RMSE = \sqrt{\tfrac{1}{2}[(\Delta^3E^{DFT} - \Delta^3E^{Hub.})^2 + (\Delta^1A_1'^{DFT} - \Delta^1A_1'^{Hub.})^2]} \tag{6.25}$$

where Δ stands for the energy difference between corresponding states ^3E or $^1A_1'$ and the ground state $^3A_2$, for example $\Delta^3E = ^3E - ^3A_2$.

g. My results of the 3-site model: many-body states of NV^- at ambient pressure

In this section I apply the method presented in the first part of this chapter in order to find the many-body states of the NV^- center at ambient pressure using the 3-site model. I present only the results obtained using analytical expressions as my numerical fit procedure yields the same result. In my model, the calculated value is a vertical transition energy because in the Hubbard model the change of atomic positions after the excitation is not taken into account. Table 6.1 contains a comparison between the DFT energy transitions calculated in the present work and used as references and those calculated from the 3-site Hubbard model. The transition are energies calculated with respect to the ground state energy. I show both my PBE and HSE06 calculations.

Table 6.1: The 3-site Hubbard model for the NV^- center. Vertical energy transition between many-body excited states and the $^3A_2$ ground state.

Symmetry	DFT-PBE (eV)	Hub.+PBE (eV)	DFT HSE06 (eV)	Hub.+HSE06 (eV)
$^1A_1'$	4.28	4.28	5.27	5.27
$^1E'$		2.84		3.42
^3E	1.89	1.89	2.36	2.36
$^1A_1$		0.71		0.82
^1E		0.27		0.32
$^3A_2$	0.0	0.0	0.0	0.0

The parameters I have found using PBE references are: $t_{CC} = 0.630$ eV, $U - V = 1.216$ eV, I have chosen $\varepsilon_C = 0$. In principle, it can be any value, because it does not influence the energy differences but rather their absolute position and I am only interested in the energy differences. In the case of the HSE06 references I have found $t_{CC} = 0.787$ eV and $U - V = 1.365$ eV.

g1. Comparison with the experiments

As one can see from the table 6.1 the states $^3A_2$, ^3E and $^1A_1'$ coincide with my DFT calculations since the model has been fit in a way to reproduce my DFT calculations. The additional knowledge we obtain from the 3-site Hubbard model consists in the multi-determinant states ^1E, $^1A_1$ and $^1E'$. I am mostly interested in the transition energies that have been observed in the experiments, in particular, the ^3E - $^3A_2$ and $^1A_1$ - ^1E transitions.

I find the value of the vertical transition ^3E - $^3A_2 = 1.89$ eV in PBE and 2.36 eV in HSE06 as compared to the experimental vertical transition of 2.2 eV [28].

As for the singlet-singlet transition, the $^1A_1$ - $^1E = 0.44$ eV in PBE and 0.51 eV in HSE06. Even though, my $^1A_1$ - ^1E energy of a vertical transition cannot be directly compared to the experimental zero phonon line, I remind here that the measured ZPL value is 1.19 eV [131] and that the ZPL value provide a lower bound for the VE value (see

Fig. 2.1.4). Thus, my singlet-singlet transition comes out to be underestimated by a factor of two.

g2. Comparison with the recent previous works

Finally, I find the order of the multiplet levels that is in complete agreement with the previous works that are shown in Fig. 6.2.5.

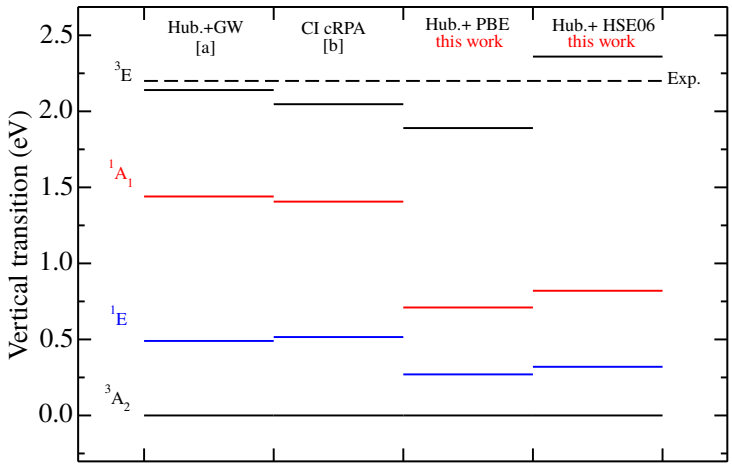

Figure 6.2.5: NV^- center. Comparison of the low-lying many-body states obtained with different methods. [a] ref. [34], [b] ref. [35]. I indicate as Hub.+PBE and Hub.+HSE06 my results where the many-body states have been obtained using my DFT-PBE and HSE06 calculations as references for the 3-site Hubbard model.

Fig.6.2.5 shows the comparison of the low-lying excited states, as calculated in the present work with the 3-site Hubbard model, with the experimental vertical transition and the most recent theoretical works. One should mention that the relative positions of the triplet ground state with respect to the first excited singlet $^3A_2 \leftrightarrow^1 E$ and first excited triplet with respect to the second excited singlet $^3E \leftrightarrow^1 A_1$ are not known experimentally. Also, these relative positions calculated with different methods are rather scattered (see next section). The most complete comparison of all theoretical findings is summarized in the ref. [35].

Among the theoretical works which have considered the problem of the NV^- center, I single out the recent works of [34, 35], in which state of the art techniques have been applied and which yield results which agree with each other and reproduce best the experimental data. I represented the data of ref. [34] and [35] in Fig. 6.2.5. In ref.[34], Choi *et al.* have used quasiparticle energies calculated with the GW method, in order to fit U and V parameters in their 4-site model. I will show in Fig. 6.2.14 that my 3-site and 4-site models yield results that are consistent with each other, so the difference between my results and Choi's results does not come from the model. In the GW method the

screening of the Coulomb interaction is taken into account by the W term using the random phase approximation. In their work, the tight-binding parameters have been found by the construction of the Maximally localized Wannier functions. Choi *et al.* have found ^3E - $^3A_2$ = 2.1 eV for the vertical transition. In ref. [35], Bockstedte *et al.* have combined Configuration Interaction (CI) with constrained Random Phase Approximation (cRPA) in order to account for the screening of interaction between highly correlated defect levels. The two methods of refs.[34] and [35] have a similar spirit in the sense that both methods treat accurately the screening of the Coulomb interaction which is important in strongly-correlated systems.

On the other hand, many works have demonstrated in recent years that the hybrid functionals can include the screening effectively [92]. For example, since the HSE06 contains a range-separated potential, it includes a part of the non-local exchange. In this way, one can think that the HSE06 can mimic part of the effect of the screening of the exchange in the GW being at the same time less computationally expensive (see section 4.4.2). Indeed, my results of the ^3E - $^3A_2$ transition, obtained with the 3-site Hubbard model parameterized using the HSE06 hybrid functional, compare rather well to the experimental vertical transition between triplet levels, and, as I will show in the next section, to the calculation of Ranjbar *et al* for both triplet-triplet and singlet-singlet transitions.

g3. Comparison with previous CI works

In figure 6.2.6, I show that the relative positions of the triplet ground state with respect to the first excited singlet $^3A_2 \leftrightarrow^1 E$ and first excited triplet with respect to the second excited singlet $^3E \leftrightarrow^1 A_1$ calculated with different flavors of the CI method are rather scattered.

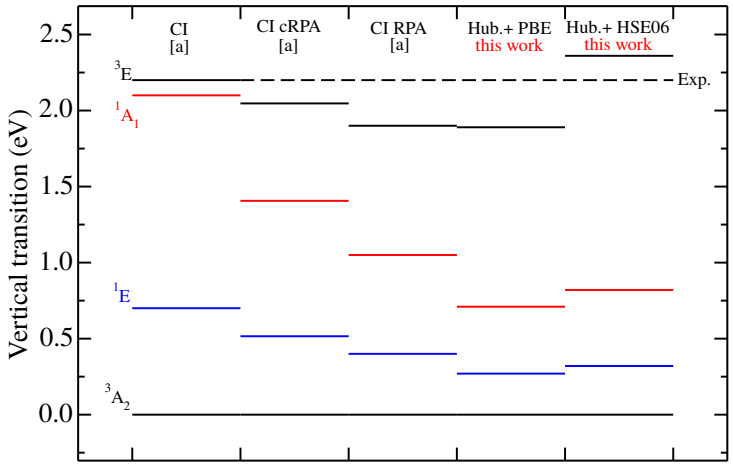

Figure 6.2.6: NV^- center. Comparison of the low-lying many-body states obtained with different methods. [a] ref. [35]. I indicate as Hub.+PBE and Hub.+HSE06 my results where the many-body states have been obtained using my DFT-PBE and HSE06 calculations as references for the 3-site Hubbard model.

For instance, CI with RPA yields a value of $^1A_1 - ^1E$ vertical transition of 0.65 eV, in close agreement with my values. The introduction of cRPA increases the value of the $^1A_1 - ^1E$ transition to 0.92 eV, close to the experimental lower bound of 1.19 eV (ZPL).

g4. Comparison with previous works including electron-hole interaction

In figure 6.2.7, I show that the inclusion of the electron-hole interaction on top of the *GW* correction, as done in ref. [34] and in ref. [127], yields values of the $^1A_1 - ^1E$ vertical transition of 0.63 eV and 0.60 eV respectively.

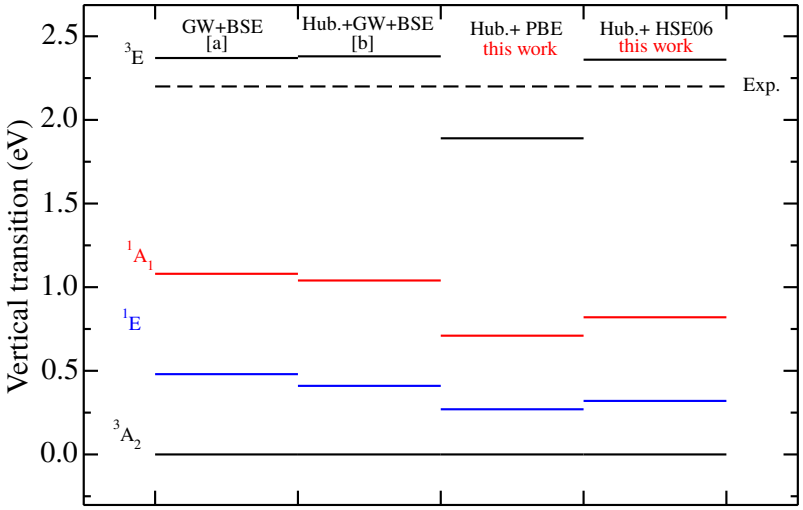

Figure 6.2.7: NV^- center. Comparison of the low-lying many-body states obtained with different methods showing the effect of electron-hole interaction. [a] ref. [127]. [b] ref. [34]. I indicate as Hub.+PBE and Hub.+HSE06 my results where the many-body states have been obtained using my DFT-PBE and HSE06 calculations as references for the 3-site Hubbard model.

The value of the singlet-singlet transition is thus very sensitive to the electron-hole interaction. The inclusion of the electron-hole interaction with the Bethe-Salpeter equation has the effect of cancelling the effect of the *GW* correction. This has already been observed in the calculations of optical absorption spectra of semiconductors [144]. Thus, one has to consider Choi's results with some care when only the *GW* correction is accounted for, and not combined with the accounting for the electron-hole interaction with BSE.

One should mention that when both quasiparticle corrections are applied in the work of ref. [127] where the direct *GW*+BSE calculation was performed and in the work of ref. [34] where the *GW*+BSE was included in Hubbard model, the results are very close. My Hubbard+HSE06 results are not far from these results, which tends to show that the BSE cancels in part the *GW* correction. Also, the role of the Hubbard model in the results of ref. [34] is questionable as the results are very close to the direct calculation with *GW*+BSE of ref. [127].

g5. Comparison with another Hubbard model-based work

Finally, in figure 6.2.8, I compare my results with the calculation of Ranjbar *et al* [75], based on the B3LYP functional and the 4-site model. In that work, the Hubbard parameters have been directly computed (see section 4.5.7). Ranjbar *et al* have found a value of 2.38 eV for the ${}^3E - {}^3A_2$ triplet-triplet transition, in perfect agreement with my HSE06 value of 2.36 eV (see section 6.2.1). This validates that my results weakly depend on the type of hybrid functional. Moreover, Ranjbar *et al* found a value of 0.61 eV for the singlet-singlet ${}^1A_1 - {}^1E$ vertical transition, to be compared with my result of 0.51 eV. Thus, my value is very close to that of Ranjbar *et al*, although the methods to find the parameters of the Hubbard model were rather different.

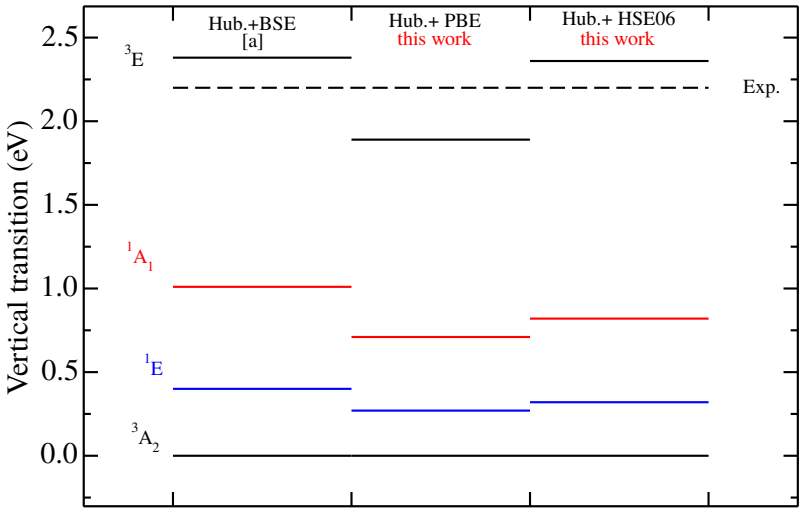

Figure 6.2.8: NV^- center. Comparison of the low-lying many-body states obtained with different methods. [a] ref. [75]. I indicate as Hub.+PBE and Hub.+HSE06 my results where the many-body states have been obtained using my DFT-PBE and HSE06 calculations as references for the 3-site Hubbard model.

h. Discussion

h1. Possible limitation of DFT

My results for the ${}^3E - {}^3A_2$ transition depend on the t hopping parameter of the eq. (6.22) which is predicted with an error of 10% in the HSE06 and B3LYP [75] calculations with respect to the experimental value. As the latter is determined with optical experiments which are very accurate, the error comes from the calculation. On the other hand, an error of 0.1 eV is the typical accuracy that one can expect from a supercell calculation with hybrid functionals and pseudopotentials. Thus, my results are in the standards of DFT calculations.

On the other hand, my results for the ${}^1A_1 - {}^1E$ transition depend on the $U - V$ parameter of eq. (6.22) which is predicted with an error estimated to be as large as 100%. Although

the effect of the supercell size needs to be checked, a test which is still being performed at the moment of writing of the manuscript [1], I do not expect large changes from a calculation with the 216-atom supercell. First, I point that, through the t parameter, finite size effects should show up in the singlet-singlet transition and in the triplet-triplet one and the latter is already within the DFT standard accuracy.

Rather, I would like to discuss the choice of the $^1A_1'$ state as a reference state for the fit of the Hubbard model. Although it is a closed-shell system (see Fig. 6.2.4), which requires a single Slater determinant (see table 4.1), the calculation of its total energy with constrained DFT may be insufficient.

h2. Gedanken experiment on $^1A_1'$ singlet state

In fact, in eq. (6.22), the parameter $U - V$ should be made larger by at least 2.24 eV (3.6-1.365 eV) in HSE06 in order to increase the $^1A_1 - ^1E$ transition energy by 0.68 eV (i.e 1.19-0.51 eV) to be larger than the experiment lower bound. I performed a Gedanken experiment by deducing the value of $E_{TOT}(^1A_1') - E_{TOT}(^3A_2)$ which would be required. It turns out that $E_{TOT}(^1A_1') - E_{TOT}(^3A_2)$ should be increased by at least 1.33 eV. The increase of the $^1A_1'$ reference total enegy would not only provoke the increase of the $^1A_1 - ^1E$ transition but would also push all singlet states $^1A_1$, ^1E, $^1E'$ and $^1A_1'$ to higher energies, as summarized in table 6.2.

Table 6.2: The 3-site Hubbard model for the NV^- center. Vertical energy transition between many-body excited states and $^3A_2$ ground state. Obtained with the evaluated $^1A_1'$ state in a way to reproduce the $^1A_1 - ^1E$ transition. Thus, $^1A_1'$ level is indicated as DFT+PBE/HSE06 Gedanken.

Symmetry	DFT-PBE (eV)	Hub.+PBE (eV)	DFT HSE06 (eV)	Hub.+HSE06 (eV)
$^1A_1'$	6.22 (Gedanken)	6.22 (Gedanken)	6.60 (Gedanken)	6.60 (Gedanken)
$^1E'$		5.52		5.44
^3E	1.89	1.89	2.36	2.36
$^1A_1$		1.66		1.72
^1E		0.46		0.52
$^3A_2$	0.0	0.0	0.0	0.0

In particular, the singlet state $^1E'$, has been found to be quasi-degenerate with the ^3E state in the calculations with GW+BSE by Ma et al. in ref. [127]. This finding is in controversy with the results of Bockstedte et al., who found the $^1E'$ state by 1 eV higher in energy than the ^3E state [35]. In my Gedanken experiment the $^1E'$ state was found

[1] Calculations with the HSE06 functional are of tremendous computational load, and the calculations realized in the present manuscript are already very involved.

to be higher in energy by the value of 3.63 eV in DFT-PBE and by the value of 3.08 eV in DFT-HSE06. This fact excludes any possibility for the $^1E'$ state to be involved in the intersystem crossing mechanism. The new parameters that has been found in this thought experiment are t_{CC} = 0.630 eV, $U - V$=4.1 eV for the DFT-PBE and t_{CC} = 0.787 eV, $U - V$=3.6 eV for DFT-HSE06.

This thought experiment substantiates the inadequacy of the DFT in evaluation the total energy of the $^1A_1'$ reference state, if we trust the experimental value. One reason of the deficiency might come from the fact that the DFT should be able to reproduce the low-lying excited state that has a symmetry different from the ground state [145]. Indeed, the ^3E triplet state is the first excited state of E symmetry, as the excited singlet state ^1E has E symmetry but it has a different spin (see figure 4.7.1). Thus, constrained DFT yields satisfying results on the $^3E - ^3A_2$ transition. On the other hand, the $^1A_1'$ state is not the excited state of the lowest energy. The singlet $^1A_1$ is also present (see figure 4.7.1). So it is probable that I have encountered the limitation of the DFT for excited states in my calculations of the $^1A_1'$ state. An alternative explanation requires to reconsider the experimental value.

h3. Fit to experiment

In the Gedanken experiment I have fitted the $^1A_1 - ^1E$ transition to the experimental value and have fixed the $^3E - ^3A_2$ transition to my DFT value in order to estimate what should have been my $^1A_1'$ to be in DFT in order to be in closer agreement to the experiment. In this section, I take the experimental values for both transitions as the reference values for my 3-site model. I summarize results in table 6.3

Table 6.3: The 3-site Hubbard model for the NV^- center. Vertical energy transition between many-body excited states and $^3A_2$ ground state. Obtained with the Hubbard model fit onto the experimental data.

Symmetry	EXP (eV)	Hubbard (eV)
$^1A_1'$		6.36
$^1E'$		5.65
^3E	1.945	1.94
$^1A_1$	↕ 1.19	1.69
^1E		0.47
$^3A_2$	0.0	0.0

One can see from table 6.3 that the many-body states fit onto the experiment are in-between the DFT-PBE and DFT-HSE06 results that I find with the Gedanken experiment

of section 6.2.1. The Hubbard model parameters that have been found to reproduce the experimental data are: t_{CC}=0.645 eV and $U-V$=4.19 eV. Finally, the procedure of the fit onto the experimental data is interesting in the sense to find the Hubbard model parameters at ambient pressure. However, since for the fit of my 3-site Hubbard model, at least two reference values are needed and since there only available experimentally data is about the triplet-triplet transition, one cannot use the experimental data for the pressure dependence study. Thus, I will continue to use my DFT calculations for the pressure study. Although the value of the singlet-singlet transition will be underestimated, we have seen in chapter 5 that the pressure coefficient for the triplet-triplet transition was valid.

k. Conclusions

I conclude that

- Many-body state ordering calculated in the 3-site Hubbard model turn out to be in perfect agreement with other recent state of the art theoretical results.
- When one accounts properly for the correlations in my model by fitting it to the HSE06 hybrid functional calculations, one can reproduce the experimental value of the triplet-triplet vertical transition ^3E - $^3A_2$.
- The 3-site model is proposed for the first time in the present work and I show will show in the next section that the 3-site model is enough to study the low lying many-body excited states of the NV^- center. Our 3-site Hubbard model contains only two independent parameters, which requires only two DFT references to be fit. For the study of the pressure dependence, the DFT references are indispensible.
- When one trusts the experimental results, and fit the 3-site model on experiment with no *adhoc* hypothesis, there is no qualitative change in the level ordering.
- I have identified a possible reason for the partial failure of DFT in calculation of the singlet-singlet transition energy in section 6.2.1 (g).

Finally, the fact that with a different approach, my results are close to those of Ranjbar *et al* [75] is puzzling and the reasons cannot be clarified from the reported results of ref. [34].

6.2.2 The 4- site Hubbard model

a. Method

I consider now the 4-site model. In this model I include the nitrogen site and 3 carbon sites neighboring the vacancy as shown in Fig. 6.2.9.

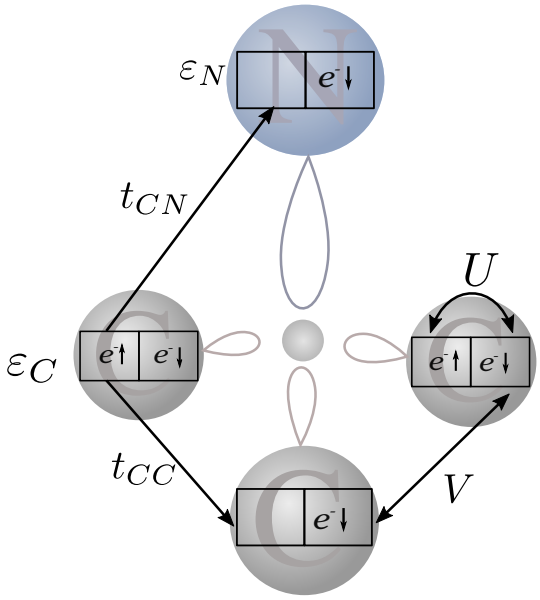

Figure 6.2.9: Schematic representation of the 4-site Hubbard model. Large grey balls are the carbon sites, the large blue ball is the nitrogen site. The small light grey ball is the vacant site. Each site can host spin-up one and spin-down one electron, this is indicated with the black squares.

Our Fock space contains $C_6^8 = 28$ basis functions. Thus, the Hamiltonian of the system is a 28×28 matrix. By analogy with the 3-site model, I start with the analytical solution.

b. Analytical solution

The analytical exact diagonalization of the 28 by 28 Hamiltonian is a tedious task, so I aim to simplify the Hamiltonian. I employ the same technique as for the 3-site model. Initially, the 4-site model contains 6 parameters: t_{CC}, t_{CN}, ε_C, ε_N, U, V. I first subtract from all the diagonal elements of the Hamiltonian its second diagonal element $\mathscr{E}_2$: $H - \mathscr{E}_2 I$, where $\mathscr{E}_2 = 2\,U + 13\,V + 4\,\varepsilon_C + 2\,\varepsilon_N$. This operation reduces my Hamiltonian to four parameters: t_{CC}, t_{CN}, $\varepsilon_C - \varepsilon_N$ and $U - V$. We can use the symmetry of the Hamiltonian and write it in the block-diagonal form. The Hamiltonian splits into three blocks with different spin projections: a 16×16 Hamiltonian with M_s=0, a 6×6 one with M_s=1 and a 6×6 one with M_s=-1. This allows us to diagonalize each block separately. For the sake of simplicity, the full initial and permuted Hamiltonians can be found in the Appendix 8.2 in the eq. (8.1) and eq. (8.2). I represent schematically non-zero matrix elements of the Hamiltonian in the block-diagonal in Fig. 6.2.10

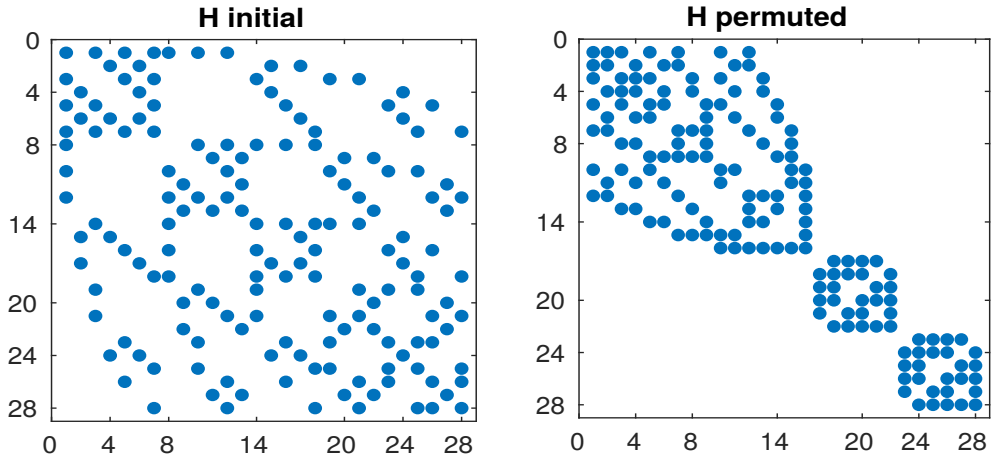

Figure 6.2.10: Schematic representation of the initial Hamiltonian and the same Hamiltonian in the block-diagonal form.

The first 16×16 sub-block of the Hamiltonian has M_s=0 and reads:

$$\begin{pmatrix}
2(\varepsilon_C-\varepsilon_N)+(\mathrm{U}-\mathrm{V}) & t_{\mathrm{CN}} & -t_{\mathrm{CN}} & 0 & -t_{\mathrm{CN}} & 0 & t_{\mathrm{CN}} & 0 & 0 & -t_{\mathrm{CN}} & 0 & t_{\mathrm{CN}} & 0 & 0 & 0 & 0 \\
t_{\mathrm{CN}} & (\varepsilon_C-\varepsilon_N) & 0 & t_{\mathrm{CN}} & 0 & -t_{\mathrm{CN}} & t_{\mathrm{CC}} & 0 & 0 & 0 & -t_{\mathrm{CN}} & t_{\mathrm{CC}} & 0 & 0 & 0 & 0 \\
-t_{\mathrm{CN}} & 0 & (\varepsilon_C-\varepsilon_N) & -t_{\mathrm{CN}} & t_{\mathrm{CC}} & 0 & 0 & -t_{\mathrm{CN}} & 0 & t_{\mathrm{CC}} & 0 & 0 & -t_{\mathrm{CN}} & 0 & 0 & 0 \\
0 & t_{\mathrm{CN}} & -t_{\mathrm{CN}} & (\mathrm{U}-\mathrm{V}) & 0 & -t_{\mathrm{CC}} & 0 & t_{\mathrm{CC}} & 0 & 0 & -t_{\mathrm{CC}} & 0 & t_{\mathrm{CC}} & 0 & 0 & 0 \\
-t_{\mathrm{CN}} & 0 & t_{\mathrm{CC}} & 0 & (\varepsilon_C-\varepsilon_N) & t_{\mathrm{CN}} & 0 & 0 & -t_{\mathrm{CN}} & t_{\mathrm{CC}} & 0 & 0 & 0 & t_{\mathrm{CN}} & 0 & 0 \\
0 & -t_{\mathrm{CN}} & 0 & -t_{\mathrm{CC}} & t_{\mathrm{CN}} & 0 & 0 & 0 & -t_{\mathrm{CC}} & 0 & t_{\mathrm{CC}} & 0 & 0 & t_{\mathrm{CC}} & 0 & 0 \\
t_{\mathrm{CN}} & t_{\mathrm{CC}} & 0 & 0 & 0 & (\varepsilon_C-\varepsilon_N) & t_{\mathrm{CN}} & t_{\mathrm{CN}} & 0 & 0 & 0 & t_{\mathrm{CC}} & 0 & 0 & t_{\mathrm{CN}} & 0 \\
0 & 0 & -t_{\mathrm{CN}} & t_{\mathrm{CC}} & 0 & 0 & t_{\mathrm{CN}} & 0 & t_{\mathrm{CC}} & 0 & 0 & 0 & t_{\mathrm{CC}} & 0 & t_{\mathrm{CC}} & 0 \\
0 & 0 & 0 & 0 & -t_{\mathrm{CN}} & -t_{\mathrm{CC}} & t_{\mathrm{CN}} & t_{\mathrm{CC}} & (\mathrm{U}-\mathrm{V}) & 0 & 0 & 0 & 0 & -t_{\mathrm{CC}} & t_{\mathrm{CC}} & 0 \\
-t_{\mathrm{CN}} & 0 & t_{\mathrm{CC}} & 0 & t_{\mathrm{CC}} & 0 & 0 & 0 & 0 & (\varepsilon_C-\varepsilon_N) & t_{\mathrm{CN}} & 0 & 0 & 0 & -t_{\mathrm{CN}} & -t_{\mathrm{CN}} \\
0 & -t_{\mathrm{CN}} & 0 & -t_{\mathrm{CC}} & 0 & t_{\mathrm{CC}} & 0 & 0 & 0 & t_{\mathrm{CN}} & 0 & 0 & 0 & 0 & -t_{\mathrm{CC}} & -t_{\mathrm{CC}} \\
t_{\mathrm{CN}} & t_{\mathrm{CC}} & 0 & 0 & 0 & 0 & t_{\mathrm{CC}} & 0 & 0 & 0 & 0 & (\varepsilon_C-\varepsilon_N) & t_{\mathrm{CN}} & -t_{\mathrm{CN}} & 0 & t_{\mathrm{CN}} \\
0 & 0 & -t_{\mathrm{CN}} & t_{\mathrm{CC}} & 0 & 0 & 0 & t_{\mathrm{CC}} & 0 & 0 & 0 & t_{\mathrm{CN}} & 0 & -t_{\mathrm{CC}} & 0 & t_{\mathrm{CC}} \\
0 & 0 & 0 & 0 & t_{\mathrm{CN}} & t_{\mathrm{CC}} & 0 & 0 & -t_{\mathrm{CC}} & 0 & 0 & -t_{\mathrm{CN}} & -t_{\mathrm{CC}} & 0 & 0 & -t_{\mathrm{CC}} \\
0 & 0 & 0 & 0 & 0 & 0 & t_{\mathrm{CN}} & t_{\mathrm{CC}} & t_{\mathrm{CC}} & -t_{\mathrm{CN}} & -t_{\mathrm{CC}} & 0 & 0 & 0 & 0 & t_{\mathrm{CC}} \\
0 & 0 & 0 & 0 & 0 & 0 & 0 & 0 & 0 & -t_{\mathrm{CN}} & -t_{\mathrm{CC}} & t_{\mathrm{CN}} & t_{\mathrm{CC}} & -t_{\mathrm{CC}} & t_{\mathrm{CC}} & (\mathrm{U}-\mathrm{V})
\end{pmatrix} \tag{6.26}$$

The two 6×6 sub-blocks are identical and they have M_s=1,-1, I show only one of them below:

$$\begin{pmatrix}
0 & -t_{\mathrm{CN}} & -t_{\mathrm{CC}} & t_{\mathrm{CN}} & t_{\mathrm{CC}} & 0 \\
-t_{\mathrm{CN}} & (\varepsilon_C-\varepsilon_N) & t_{\mathrm{CN}} & t_{\mathrm{CC}} & 0 & t_{\mathrm{CC}} \\
-t_{\mathrm{CC}} & t_{\mathrm{CN}} & 0 & 0 & t_{\mathrm{CC}} & -t_{\mathrm{CN}} \\
t_{\mathrm{CN}} & t_{\mathrm{CC}} & 0 & (\varepsilon_C-\varepsilon_N) & t_{\mathrm{CN}} & t_{\mathrm{CC}} \\
t_{\mathrm{CC}} & 0 & t_{\mathrm{CC}} & t_{\mathrm{CN}} & 0 & -t_{\mathrm{CN}} \\
0 & t_{\mathrm{CC}} & -t_{\mathrm{CN}} & t_{\mathrm{CC}} & -t_{\mathrm{CN}} & (\varepsilon_C-\varepsilon_N)
\end{pmatrix} \tag{6.27}$$

As two 6×6 sub-spaces of the Hamiltonian are the same, the eigenenergies will be identical. The diagonalization of all sub-spaces gives us 28 eigenvalues, or 11 different ones

(as some are degenerated). I present the differences of energies with respect to the ground state:

Energy	Degeneracy	Symmetry
$\Delta E_1 = 0$	$(g=3)$	${}^3A_2$
$\Delta E_2 = \frac{1}{2}(\varepsilon_C - \varepsilon_N) + 2\,t_{\mathrm{CC}} - \frac{1}{2}\sqrt{f}$	$(g=6)$	${}^3E$
$\Delta E_3 = \frac{1}{2}(\varepsilon_C - \varepsilon_N) + 2\,t_{\mathrm{CC}} + \frac{1}{2}\sqrt{f}$	$(g=6)$	${}^3E$
$\Delta E_4 = \frac{1}{3}(\varepsilon_C - \varepsilon_N) + 2\,t_{\mathrm{CC}} + m + bh^{-1/3} + h^{1/3}$	$(g=2)$	${}^1E$
$\Delta E_5 = \frac{1}{3}(\varepsilon_C - \varepsilon_N) + 2\,t_{\mathrm{CC}} + m - \frac{1}{2}bh^{-1/3} - \frac{1}{2}h^{1/3} - j$	$(g=2)$	${}^1E$
$\Delta E_6 = \frac{1}{3}(\varepsilon_C - \varepsilon_N) + 2\,t_{\mathrm{CC}} + m - \frac{1}{2}bh^{-1/3} - \frac{1}{2}h^{1/3} + j$	$(g=2)$	${}^1E$
$\Delta E_7 = (\varepsilon_C - \varepsilon_N) + 4\,t_{\mathrm{CC}}$	$(g=3)$	${}^3A_1$
$\Delta E_8 = a_1 - k_1 + 2\,t_{\mathrm{CC}} - \frac{1}{6}\sqrt{n_1 - p_1}\,{j_1}^{-1/4}{l_1}^{-1/6}$	$(g=1)$	${}^1A_1$
$\Delta E_9 = a_1 - k_1 + 2\,t_{\mathrm{CC}} + \frac{1}{6}\sqrt{n_1 - p_1}\,{j_1}^{-1/4}{l_1}^{-1/6}$	$(g=1)$	${}^1A_1$
$\Delta E_{10} = a_1 + k_1 + 2\,t_{\mathrm{CC}} - \frac{1}{6}\sqrt{n_1 + p_1}\,{j_1}^{-1/4}{l_1}^{-1/6}$	$(g=1)$	${}^1A_1$
$\Delta E_{11} = a_1 + k_1 + 2\,t_{\mathrm{CC}} + \frac{1}{6}\sqrt{n_1 + p_1}\,{j_1}^{-1/4}{l_1}^{-1/6}$	$(g=1)$	${}^1A_1$

(6.28)

The analytical solutions of the 4-site model are more complex than in the case of the 3-site model, I have used the notations indicated in eq. (6.29) and 6.30 to simplify them.

$$
\begin{aligned}
a &= (\varepsilon_C - \varepsilon_N) + (\mathrm{U} - \mathrm{V}) - 2\,t_{\mathrm{CC}} \\
b &= \tfrac{1}{3}(t_{\mathrm{CC}}((\varepsilon_C - \varepsilon_N) + 2(\mathrm{U} - \mathrm{V}) + t_{\mathrm{CC}}) - (\varepsilon_C - \varepsilon_N)\,(\mathrm{U} - \mathrm{V})) + \tfrac{1}{9}a^2 + {t_{\mathrm{CN}}}^2 \\
c &= t_{\mathrm{CC}}((\varepsilon_C - \varepsilon_N) + 2(\mathrm{U} - \mathrm{V}) + t_{\mathrm{CC}}) - (\varepsilon_C - \varepsilon_N)\,(\mathrm{U} - \mathrm{V}) + 3\,{t_{\mathrm{CN}}}^2 \\
d &= \tfrac{1}{6}a\,c - (\varepsilon_C - \varepsilon_N)\,{t_{\mathrm{CC}}}^2 + \tfrac{1}{2}(\mathrm{U} - \mathrm{V})\,{t_{\mathrm{CC}}}^2 - \tfrac{1}{2}(\mathrm{U} - \mathrm{V})\,{t_{\mathrm{CN}}}^2 + 3\,t_{\mathrm{CC}}\,{t_{\mathrm{CN}}}^2 + \tfrac{1}{27}a^3 \\
f &= (\varepsilon_{\mathrm{C}} - \varepsilon_{\mathrm{N}})^2 - 4\,(\varepsilon_{\mathrm{C}} - \varepsilon_{\mathrm{N}})\,t_{\mathrm{CC}} + 4\,{t_{\mathrm{CC}}}^2 + 12\,{t_{\mathrm{CN}}}^2 \\
g &= \left({t_{\mathrm{CC}}}^3 - \tfrac{1}{2}(\varepsilon_C - \varepsilon_N)\,(\mathrm{U} - \mathrm{V})\,t_{\mathrm{CC}} + d\right)^2 - b^3 \\
h &= d + \sqrt{g} + {t_{\mathrm{CC}}}^3 - \tfrac{1}{2}(\varepsilon_C - \varepsilon_N)\,(\mathrm{U} - \mathrm{V})\,t_{\mathrm{CC}} \\
j &= \tfrac{\sqrt{3}}{2}\,(bh^{-1/3} - h^{1/3})\,1\mathrm{i} \\
m &= \tfrac{1}{3}((\mathrm{U} - \mathrm{V}) - 2\,t_{\mathrm{CC}})
\end{aligned}
\tag{6.29}
$$

I notice that all of the singlet levels of the ${}^1A_1$ symmetry contain the $a_1 - p_1$ expressions, with

$$
\begin{aligned}
a_1 &= \tfrac{3}{4}\left(\varepsilon_C - \varepsilon_N\right) + \tfrac{1}{2}(\mathrm{U} - \mathrm{V}) + t_{\mathrm{CC}} \\
b_1 &= -6\,{a_1}^2 + 2\left(\varepsilon_C - \varepsilon_N\right)^2 + 4\left(\varepsilon_C - \varepsilon_N\right)(\mathrm{U} - \mathrm{V}) + 10\left(\varepsilon_C - \varepsilon_N\right) t_{\mathrm{CC}} + (\mathrm{U} - \mathrm{V})^2 + 8\,(\mathrm{U} - \mathrm{V})\, t_{\mathrm{CC}} \\
&\quad - 4\,{t_{\mathrm{CC}}}^2 - 12\,{t_{\mathrm{CN}}}^2 \\
c_1 &= 2\left(\varepsilon_C - \varepsilon_N\right)^2 + 4\left(\varepsilon_C - \varepsilon_N\right)(\mathrm{U} - \mathrm{V}) + 10\left(\varepsilon_C - \varepsilon_N\right) t_{\mathrm{CC}} + (\mathrm{U} - \mathrm{V})^2 + 8\,(\mathrm{U} - \mathrm{V})\, t_{\mathrm{CC}} - 4\,{t_{\mathrm{CC}}}^2 \\
&\quad - 12\,{t_{\mathrm{CN}}}^2 \\
d_1 &= 2\left(\varepsilon_C - \varepsilon_N\right)^2(\mathrm{U} - \mathrm{V}) + 4\left(\varepsilon_C - \varepsilon_N\right)^2 t_{\mathrm{CC}} + \left(\varepsilon_C - \varepsilon_N\right)(\mathrm{U} - \mathrm{V})^2 + 12\left(\varepsilon_C - \varepsilon_N\right)(\mathrm{U} - \mathrm{V})\, t_{\mathrm{CC}} \\
&\quad - 16\left(\varepsilon_C - \varepsilon_N\right){t_{\mathrm{CC}}}^2 - 12\left(\varepsilon_C - \varepsilon_N\right){t_{\mathrm{CN}}}^2 + 4\,(\mathrm{U} - \mathrm{V})^2\, t_{\mathrm{CC}} - 16\,(\mathrm{U} - \mathrm{V})\,{t_{\mathrm{CN}}}^2 - 16\,{t_{\mathrm{CC}}}^3 \\
f_1 &= 3\,{a_1}^4 - c_1\,{a_1}^2 + d_1\, a_1 - 4\left(\varepsilon_C - \varepsilon_N\right)^2(\mathrm{U} - \mathrm{V})\, t_{\mathrm{CC}} + 16\left(\varepsilon_C - \varepsilon_N\right)^2{t_{\mathrm{CC}}}^2 - 2\left(\varepsilon_C - \varepsilon_N\right)(\mathrm{U} - \mathrm{V})^2\, t_{\mathrm{CC}} \\
&\quad + 8\left(\varepsilon_C - \varepsilon_N\right)(\mathrm{U} - \mathrm{V})\,{t_{\mathrm{CN}}}^2 + 32\left(\varepsilon_C - \varepsilon_N\right){t_{\mathrm{CC}}}^3 - 24\left(\varepsilon_C - \varepsilon_N\right) t_{\mathrm{CC}}\,{t_{\mathrm{CN}}}^2 - 4\,(\mathrm{U} - \mathrm{V})^2\,{t_{\mathrm{CC}}}^2 \\
&\quad + 4\,(\mathrm{U} - \mathrm{V})^2\,{t_{\mathrm{CN}}}^2 + 16\,(\mathrm{U} - \mathrm{V})\,{t_{\mathrm{CC}}}^3 - 48\,{t_{\mathrm{CC}}}^2\,{t_{\mathrm{CN}}}^2 \\
g_1 &= 8\,{a_1}^3 - 2\,c_1\, a_1 + d_1 \\
h_1 &= 16\,{b_1}^4\, f_1 + 4\,{b_1}^3\,{g_1}^2 + 128\,{b_1}^2\,{f_1}^2 + 144\, b_1\, f_1\,{g_1}^2 + 256\,{f_1}^3 + 27\,{g_1}^4 \\
j_1 &= 9\,{l_1}^{2/3} - 6\, b_1\,{l_1}^{1/3} - 12\, f_1 + {b_1}^2 \\
k_1 &= \tfrac{1}{6}\sqrt{j_1}\,{l_1}^{-1/6} \\
l_1 &= \tfrac{4}{3}\, b_1\, f_1 + \tfrac{\sqrt{3}}{18}\sqrt{h_1} + \tfrac{1}{27}{b_1}^3 + \tfrac{1}{2}{g_1}^2 \\
m_1 &= 72\, b_1\, f_1 + 3\sqrt{3}\sqrt{h_1} + 2\,{b_1}^3 + 27\,{g_1}^2 \\
n_1 &= 12\, f_1\sqrt{j_1} - {b_1}^2\sqrt{j_1} - 9\sqrt{j_1}\,{l_1}^{2/3} - 12\, b_1\sqrt{j_1}\,{l_1}^{1/3} \\
p_1 &= 3\sqrt{6}\, g_1\sqrt{m_1}
\end{aligned}
\tag{6.30}
$$

As in the case of the 3-site model, the triplet energy differences obtained with the 4-site model do not depend on the U-V parameter.

c. Parameterization

I now want to parameterize my model. On the one hand, the 4-site model contains 4 parameters whereas the 3-site model contains only two, and thus more DFT references are needed. On the other hand, the Fock space of the 4-site model is also larger (28 basis function w.r.t to 15 ones). This fact allows us to associate more high energy transitions to those calculated in the DFT. I associate the differences $\Delta E_2, \Delta E_3, \Delta E_7, \Delta E_9, \Delta E_{11}$ from eq. (6.28) with the references $E_{TOT}(^3E) - E_{TOT}(^3A_2)$, $E_{TOT}(^3E^N) - E_{TOT}(^3A_2)$, $E_{TOT}(^3A_1^N) - E_{TOT}(^3A_2)$, $E_{TOT}(^1A_1') - E_{TOT}(^3A_2)$, $E_{TOT}(^1A_1'^N) - E_{TOT}(^3A_2)$ that can be calculated from the DFT. Fig. 6.2.11 shows what occupations should be imposed in the constrained DFT in order to calculate these levels.

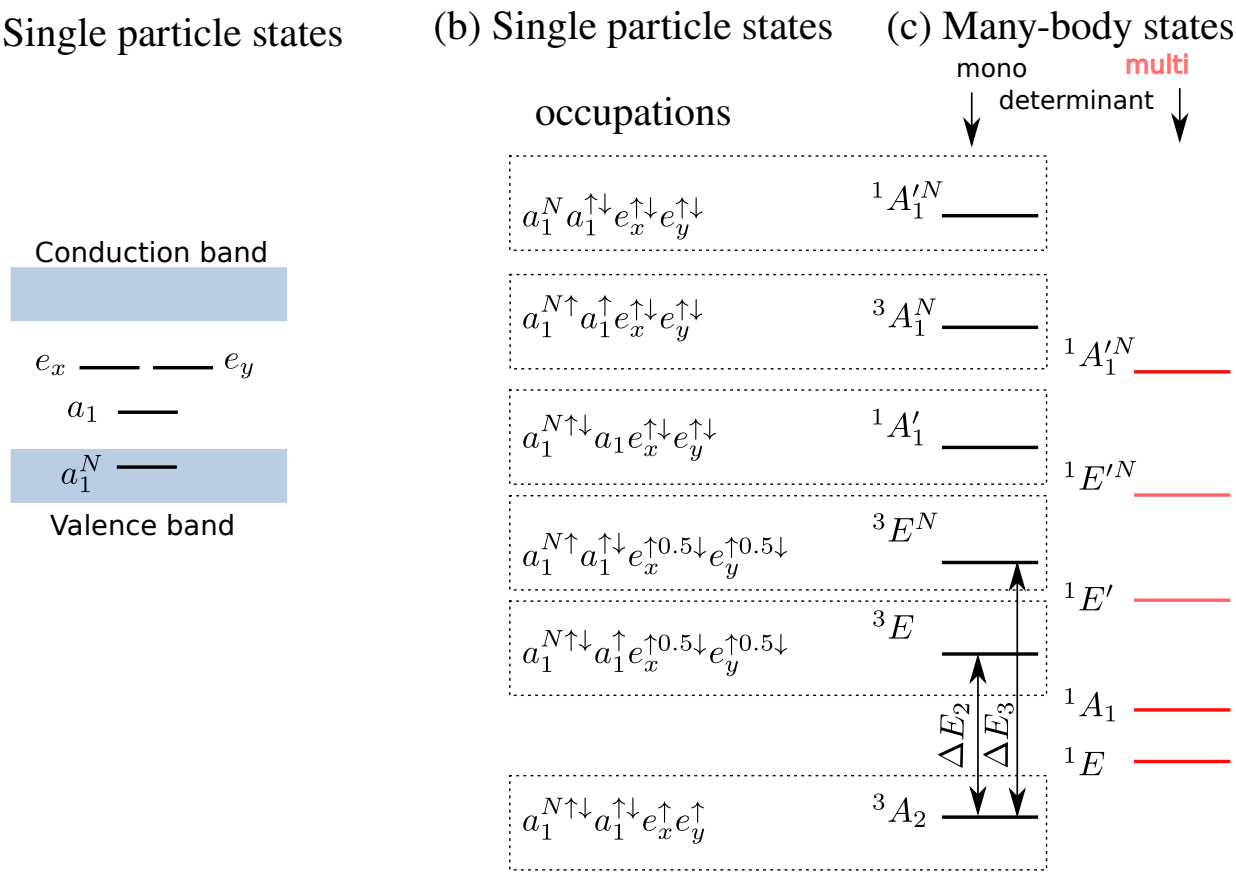

Figure 6.2.11: (a) Schema of the single-electron levels of the NV center in the band gap. same as Fig. 2.1.1 (b). (b) Occupations of the single-electron levels of panel (a) corresponding to the many-body state in panel (c). (c) Many-body levels of the NV^- center that can be found from the 4-site model. States that can be represented as a single Slater determinant are in the left column, the multi-determinant ones are in the right column.

I note that we have a set of dependent equations as $\Delta E_2 + \Delta E_3 = \Delta E_7$, this can be easily seen from the eq. (6.28). This means that we cannot solve together these 3 equations to obtain 3 parameters, but instead 2 parameters can be found. So, I solve 2 equations ΔE_2 and ΔE_3 from eq. (6.28) with respect to the parameters t_{CC}, t_{CN} and this gives us:

$$\begin{aligned} t_{CC} &= \frac{1}{4}(\Delta \mathrm{E}_2 - (\varepsilon_\mathrm{C} - \varepsilon_\mathrm{N}) + \Delta \mathrm{E}_3) \\ t_{CN} &= \frac{1}{2}\sqrt{\frac{1}{12}\left(3\,\Delta \mathrm{E}_3 - 3\,(\varepsilon_\mathrm{C} - \varepsilon_\mathrm{N}) - \Delta \mathrm{E}_2\right)\left(3\,(\varepsilon_\mathrm{C} - \varepsilon_\mathrm{N}) - 3\,\Delta \mathrm{E}_2 + \Delta \mathrm{E}_3\right)} \end{aligned} \tag{6.31}$$

Interestingly, the relation of the triplet energy levels, $\Delta E_2 + \Delta E_3 = \Delta E_7$ that I obtain analytically from my model is verified by my DFT calculations. By substituting my DFT-

PBE [2] values I find that this equation holds to the precision of 0.01 eV with my DFT-PBE calculations. This result is important because it confirms that my model is consistent with my DFT calculations and that I properly identify the levels that I occupy with constrained DFT.

Till now we have found only two parameters and two more are left undetermined. In principle, we have enough DFT references in order to obtain analytical expressions for all of the parameters. However, we have already used two triplet references to find t_{CC} and t_{CN} and another triplet reference ΔE_7 cannot be used since it forms a dependent set of equations, and thus, it is not a true reference. We are left with two singlet references ΔE_9 and ΔE_{11}. Unfortunately, the analytical expressions for these singlet references are equations of a high order and an analytical solution cannot be found for the parameters $\varepsilon_C - \varepsilon_N$ and $U - V$. Therefore, in the parameterization of the 4-site model I use a mixed determination of the parameters: I find t_{CC} and t_{CN} using formulas that I found and I perform the numerical fit of the $\varepsilon_C - \varepsilon_N$ and $U - V$ parameters as explained previously. As an error ctriterion, I have taken the root-mean square error:

$$\begin{aligned} RMSE =&(\tfrac{1}{4}[(\Delta^3 E^{DFT} - \Delta^3 E^{Hub.})^2 + (\Delta^1 {A_1'}^{DFT} - \Delta^1 {A_1'}^{Hub.})^2 \\ &+ (\Delta^3 E^{NDFT} - \Delta^3 E^{NHub.})^2 + (\Delta^1 {A_1'}^{NDFT} - \Delta^1 {A_1'}^{NHub.})^2])^{1/2}, \end{aligned} \tag{6.32}$$

where Δ stands for the energy difference between corresponding states ${}^3E$ or ${}^1A_1'$ and the ground state ${}^3A_2$, for example $\Delta^3 E = {}^3E - {}^3A_2$.

d. Results: Many-body states of NV^- at ambient pressure

I apply now my mixed analytical-fit procedure in order to find the many-body states of the NV^- center using the 4-site model. Table 6.4 shows the comparison of DFT calculated reference energies and energies found from the Hubbard model. Energy differences are calculated with respect to the ground state.

[2] The HSE06 calculations of the excited states of high energy are so far not being converged

Table 6.4: The 4-site Hubbard model for the NV^- center. Energy of the transitions between many-body excited states and the ${}^3A_2$ ground state.

Symmetry	DFT-PBE (eV)	Hub.+PBE (eV)
${}^1{A_1'}^N$	8.65	8.65
${}^1{A_1'}^N$		6.83
${}^3A_1^N$	6.03	6.03
${}^1{E'}^N$		4.79
${}^1A_1'$	4.28	4.28
${}^3E^N$	4.14	4.14
${}^1E'$		2.13
${}^3E$	1.89	1.89
${}^1A_1$		0.75
${}^1E$		0.31
${}^3A_2$	0.0	0.0

In order to reproduce the PBE energy differences I have found the following Hubbard parameters: $\varepsilon_C - \varepsilon_N = 1.486$ eV, $t_{CC} = 1.136$ eV, $t_{CN} = 0.609$ eV, $U - V = 1.219$ eV. As in the case of the 3-site model, I find a good agreement of the ordering of the low-lying excited states with the previous works reported in Fig 6.2.5. Also, the transition energies for the low lying states in the 4-site model are in very good agreement with the 3-site model.

e. Occupation matrix and unpaired spin density

Two other interesting properties of the system that can be calculated from my Hubbard model are the occupation matrix and the unpaired spin density. The calculation of the unpaired spin density in a certain site allows us to perform a comparison with experiments where the distribution of the spin density on the atoms neighboring to vacancy of the NV^- center was found with the EPR technique [29, 142]. Similar calculations have been performed in the ref. [75]. Such a comparison allows us to provide an additional validation of my Hubbard model.

The occupation matrix in my model is defined as follows:

$$Q = \Phi^T |C|^2, \tag{6.33}$$

where Φ^T is the transposed matrix of the basis functions. The C matrix is the eigenfunction coefficient matrix that we obtain after the diagonalization of the Hamiltonian of the system. Defining the occupation matrix Q in this way, the columns of this matrix correspond to the states and the raws correspond to the sites. I remind that there are two position reserved per site, the first one is the spin-up position, the second one is the spin-down position. So the occupation of the site i in the state j is given by the matrix element Q_{ij} and it has the

meaning of which number of electrons does occupy the considered site in the considered state.

From this definition I can derive the normalization condition for the Q matrix: for any state j we have

$$\sum_i Q_{ij} = N, \tag{6.34}$$

where N is the total number of electrons in the system (4 in our case). So, the sum over all sites in each state gives the total number of electrons in the system.

The occupation matrix itself is not very informative, however, we can define in a similar manner another physical quantity: the unpaired spin density matrix. Since fully occupied sites do not participate to the total spin, in order to calculate the spin density in a certain site, one should make the sum of squares of the corresponding eigenfunction coefficients of the basis functions that have one electron in the considered site:

$$Q' = \Phi'^T |C|^2, \tag{6.35}$$

where Φ' is non-zero only when the site is occupied only with one electron. I use the parameters found in the previous section in order to calculate numerically the spin density. Table 6.5 summarizes spin densities in the 3 carbon sites and in the nitrogen site at each many-electron state calculated using the Hubbard parameters fit onto the DFT-PBE calculations.

As one can see from Table 6.5, I have found that the spin density in the nitrogen site in the ground state $^3A_2$ is completely zero. Also, it is negligible in the two first excited singlets ^1E and $^1A_1$. In the higher excited states, the spin density increases in the nitrogen site and decreases in carbon sites. This is in perfect qualitative agreement with experimental EPR studies [29, 142] which have shown that the unpaired-electron probability density of the ground state is mainly localized on the nearest-neighbor carbon atoms.

Also, in ref. [75] where the unpaired spin density was calculated with the 4-site Hubbard model with exchange terms (see section 4.5.7), it was found that, in the excited ^3E state, the density around the nitrogen atom increases while it decreases around the carbon atoms. Our spin densities of the 4-site model compare rather well with the previous studies of this quantity in the Hubbard model [75] and in the EPR experiments [29, 142].

Table 6.5: The 4-site Hubbard model for the NV^- center. Spin density in carbon sites and nitrogen site for each many-body state of the NV^-.

Symmetry	spin-up				spin-down			
	C_1	C_2	C_3	N	C_1	C_2	C_3	N
$^3A_2$	0.333	0.333	0.333	0	0.333	0.333	0.333	0
	0.333	0.333	0.333	0	0.333	0.333	0.333	0
	0.333	0.333	0.333	0	0.333	0.333	0.333	0
^1E	0.170	0.389	0.438	0.004	0.170	0.389	0.438	0.004
	0.494	0.276	0.227	0.004	0.494	0.276	0.227	0.004
$^1A_1$	0.333	0.333	0.333	0.001	0.333	0.333	0.333	0.001
^3E	0.103	0.190	0.370	0.337	0.136	0.147	0.379	0.337
	0.331	0.275	0.058	0.337	0.324	0.282	0.056	0.337
	0.331	0.223	0.108	0.337	0.342	0.247	0.073	0.337
	0.374	0.199	0.090	0.337	0.316	0.277	0.070	0.337
	0.086	0.207	0.370	0.337	0.380	0.137	0.146	0.337
	0.129	0.231	0.303	0.337	0.087	0.203	0.373	0.337
$^1E'$	0.218	0.278	0.014	0.490	0.218	0.278	0.014	0.490
	0.122	0.062	0.326	0.490	0.122	0.062	0.326	0.490
$^3E^N$	0.170	0.373	0.294	0.163	0.125	0.315	0.398	0.163
	0.366	0.258	0.213	0.163	0.355	0.118	0.364	0.163
	0.175	0.22	0.444	0.163	0.201	0.192	0.445	0.163
	0.358	0.366	0.113	0.163	0.308	0.394	0.135	0.163
	0.439	0.230	0.168	0.163	0.193	0.199	0.445	0.163
	0.437	0.220	0.181	0.163	0.378	0.336	0.123	0.163
$^1A'_1$	0.185	0.185	0.185	0.444	0.185	0.185	0.185	0.444
$^1E'^N$	0.252	0.246	0.245	0.257	0.252	0.246	0.25	0.257
	0.244	0.250	0.250	0.257	0.244	0.250	0.250	0.257
$^3A_1^N$	0.167	0.167	0.167	0.5	0.167	0.167	0.167	0.5
	0.167	0.167	0.167	0.5	0.167	0.167	0.167	0.5
	0.167	0.167	0.167	0.5	0.167	0.167	0.167	0.5
$^1A'^N_1$	0.312	0.312	0.312	0.065	0.312	0.312	0.312	0.065
$^1A'_1$	0.235	0.235	0.235	0.295	0.235	0.235	0.235	0.295

6.2.3 Comparison of the 3- and 4- site models

a. Method

One can compare 3 and 4 site models if one considers the 3-site model as the limiting case of the 4-site model when t_{CN}=0.

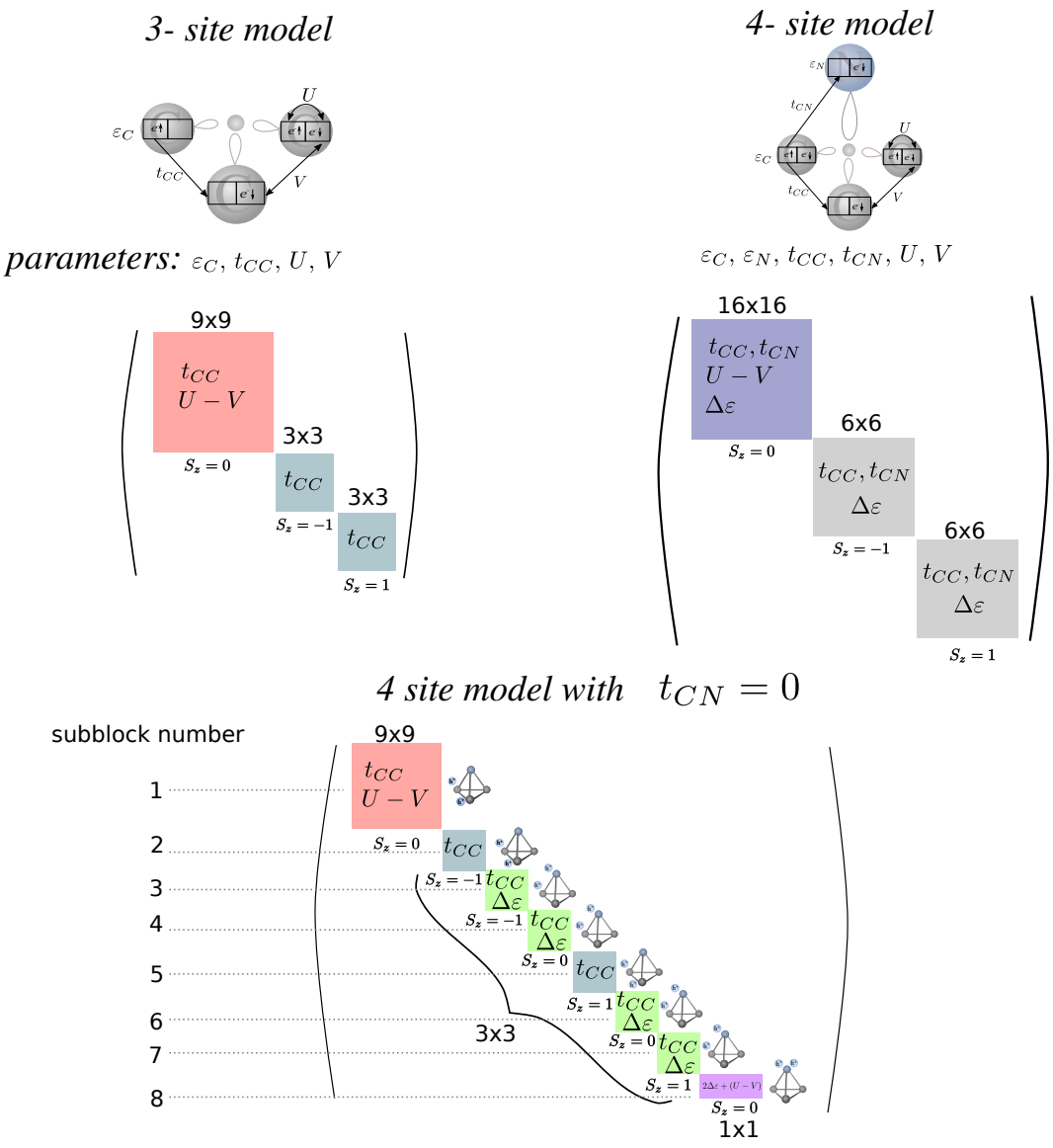

Figure 6.2.12: Schematic representation of the Hamiltonians of the 3-site model on the top left panel; 4-site model - top right panel; and the limit case $t_{CN} = 0$ in the 4-site model in the bottom panel. The identical sub-blocks in Hamiltonians are highlighted with the same color. The text within each sub-block indicates on which parameters it depends. A small drawing near each sub-block illustrates where the holes are localized in the basis functions corresponding to this sub-block.

When we put t_{CN}=0 in the Hamiltonian of the 4-site model in the block-diagonal form, it splits in more sub-blocks. This can be easily understood because in this case the system splits into two isolated systems: 1 nitrogen site and 3 carbon sites. Fig. 6.2.12 summarizes the comparison of the Halmitonians of the 3-, 4-site models and a model of 4-sites with $t_{CN} = 0$. One can identify the sub-blocks that are identical to those from the 3 site block-diagonal Hamiltonian. I highlight the identical sub-blocks with the same color in Fig. 6.2.12. This is the first sub-block which is identical to the first sub-block from the 3-site model in red color:

$$\begin{pmatrix} (\mathrm{U}-\mathrm{V}) & -t_{\mathrm{CC}} & t_{\mathrm{CC}} & 0 & -t_{\mathrm{CC}} & t_{\mathrm{CC}} & 0 & 0 & 0 \\ -t_{\mathrm{CC}} & 0 & 0 & -t_{\mathrm{CC}} & t_{\mathrm{CC}} & 0 & t_{\mathrm{CC}} & 0 & 0 \\ t_{\mathrm{CC}} & 0 & 0 & t_{\mathrm{CC}} & 0 & t_{\mathrm{CC}} & 0 & t_{\mathrm{CC}} & 0 \\ 0 & -t_{\mathrm{CC}} & t_{\mathrm{CC}} & (\mathrm{U}-\mathrm{V}) & 0 & 0 & -t_{\mathrm{CC}} & t_{\mathrm{CC}} & 0 \\ -t_{\mathrm{CC}} & t_{\mathrm{CC}} & 0 & 0 & 0 & 0 & 0 & -t_{\mathrm{CC}} & -t_{\mathrm{CC}} \\ t_{\mathrm{CC}} & 0 & t_{\mathrm{CC}} & 0 & 0 & 0 & -t_{\mathrm{CC}} & 0 & t_{\mathrm{CC}} \\ 0 & t_{\mathrm{CC}} & 0 & -t_{\mathrm{CC}} & 0 & -t_{\mathrm{CC}} & 0 & 0 & -t_{\mathrm{CC}} \\ 0 & 0 & t_{\mathrm{CC}} & t_{\mathrm{CC}} & -t_{\mathrm{CC}} & 0 & 0 & 0 & t_{\mathrm{CC}} \\ 0 & 0 & 0 & 0 & -t_{\mathrm{CC}} & t_{\mathrm{CC}} & -t_{\mathrm{CC}} & t_{\mathrm{CC}} & (\mathrm{U}-\mathrm{V}) \end{pmatrix} \tag{6.36}$$

Next, sub-blocks 2 and 5 are in blue color and are identical to the sub-blocks 2 and 3 of the 3-site model:

$$\begin{pmatrix} 0 & -t_{\mathrm{CC}} & t_{\mathrm{CC}} \\ -t_{\mathrm{CC}} & 0 & t_{\mathrm{CC}} \\ t_{\mathrm{CC}} & t_{\mathrm{CC}} & 0 \end{pmatrix} \tag{6.37}$$

The sub-blocks 3, 4, 6 and 7, in green color, are identical and correspond to the situation when one hole is hosted by one of three carbon atoms and one hole is hosted by the nitrogen atom. This situation is not possible in the 3-site model. I show only one of them:

$$\begin{pmatrix} (\varepsilon_C - \varepsilon_N) & t_{\mathrm{CC}} & t_{\mathrm{CC}} \\ t_{\mathrm{CC}} & (\varepsilon_C - \varepsilon_N) & t_{\mathrm{CC}} \\ t_{\mathrm{CC}} & t_{\mathrm{CC}} & (\varepsilon_C - \varepsilon_N) \end{pmatrix} \tag{6.38}$$

The very last sub-block of the Hamiltonian in purple color, contains only one element. This level corresponds to the situation when 2 holes are hosted by the nitrogen atom. This situation is also inherent only to the 4-site model and the term reads:

$$2\,(\varepsilon_C - \varepsilon_N) + (\mathrm{U}-\mathrm{V}). \tag{6.39}$$

To conclude, a simple analysis of the 4-site Hamiltonian with t_{CN}=0 allows us to understand that the 3-site model is completely contained in the 4-site model. We can find, inherent to the 3-site model Hamiltonian, sub-blocks that are inside the Hamiltonian of the 4-site model in the limiting case of t_{CN}=0. Therefore, the eigenenergies resulting from the diagonalization of these sub-block will be the same in the limiting case, as shown in the next section.

b. Numerical comparison: limiting case

I first want to compare the eigenenergies of the two models in the limiting case. In Fig. 6.2.13 I plot in the 3-site and 4-site levels together. I choose parameters which are close to the realistic ones of the 3-site model: ε_C= 2.0 eV, ε_N= 1.0 eV, t_{CC}=0.66 eV, $U-V$=1.24 eV. I plot the 4-site model levels as a function of t_{CN} in order to make a connection with the 3-site level at $t_{CN}=0$. Indeed, one can see that the 3-site model is fully contained in the 4-site model. All 3-site levels convert into the corresponding 4-site levels in the limiting case. I have done the same conclusion just looking at the Hamiltonian of the 4-site model with $t_{CN}=0$: it contains all sub-blocks of the 3-site model, plus nitrogen-related sub-blocks. Thus, on the right-hand side of the plot we can find nitrogen-related levels with a ^{N} superscript that have no analogue in the 3-site model.

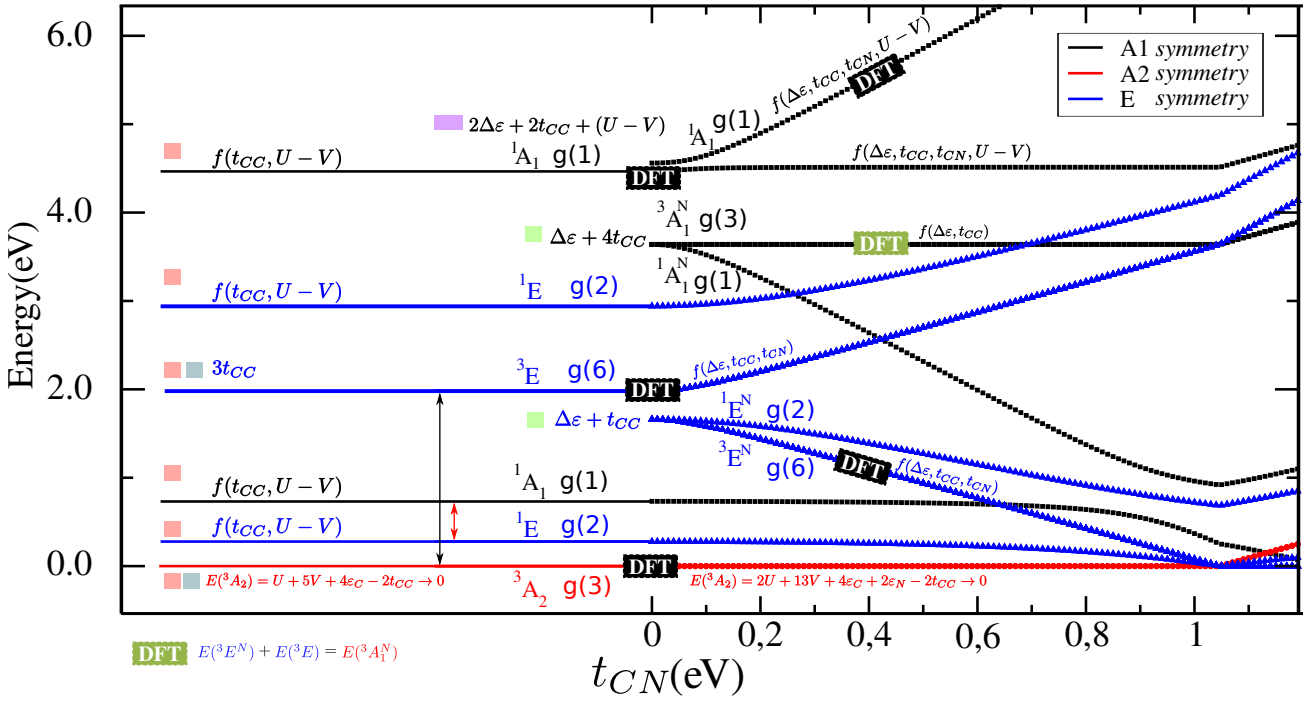

Figure 6.2.13: Comparison of eigenenergies of the 3-site and 4-site models. The 3-site model energy levels are plotted on the left util $t_{CN}=0$ value (energies are artificially drawn as a continuous line, there is no variation of t_{CN} value since the 3-site model does not contain this parameter). After this value, the 4-site model energy levels are plotted as a function of t_{CN}. Levels marked with a colored square are coming from the Hamiltonian sub-block of the corresponding color in Fig. 6.2.12. All levels are normalized with respect to the ground state. Black squares with the DFT signature illustrate that those levels can be calculated from the DFT (see section 6.2.1 (e)). The green square with the DFT signature illustrates that the level can be calculated from DFT but it forms a set of dependent equations and is not used as a reference level in the present work.

In Fig. 6.2.13 I indicate energy transitions which are of interest for the present study, namely, those corresponding to the triplet-triplet and singlet-singlet transitions observed experimentally.

Finally, I can conclude that the levels that are important for this study can be found from the 3-site model, and thus, the 3-site model is sufficient for our purposes.

c. Numerical comparison: fit onto DFT references

I now aim to compare the eigenenergies of the two models in the case when both are fit independently onto the DFT references, as discussed in previous sections 6.2.2 and 6.2.1 about parameterization. I plot in Fig. 6.2.14 the levels of both 3-site and 4-site models using the parameters at which both models fit the DFT references.

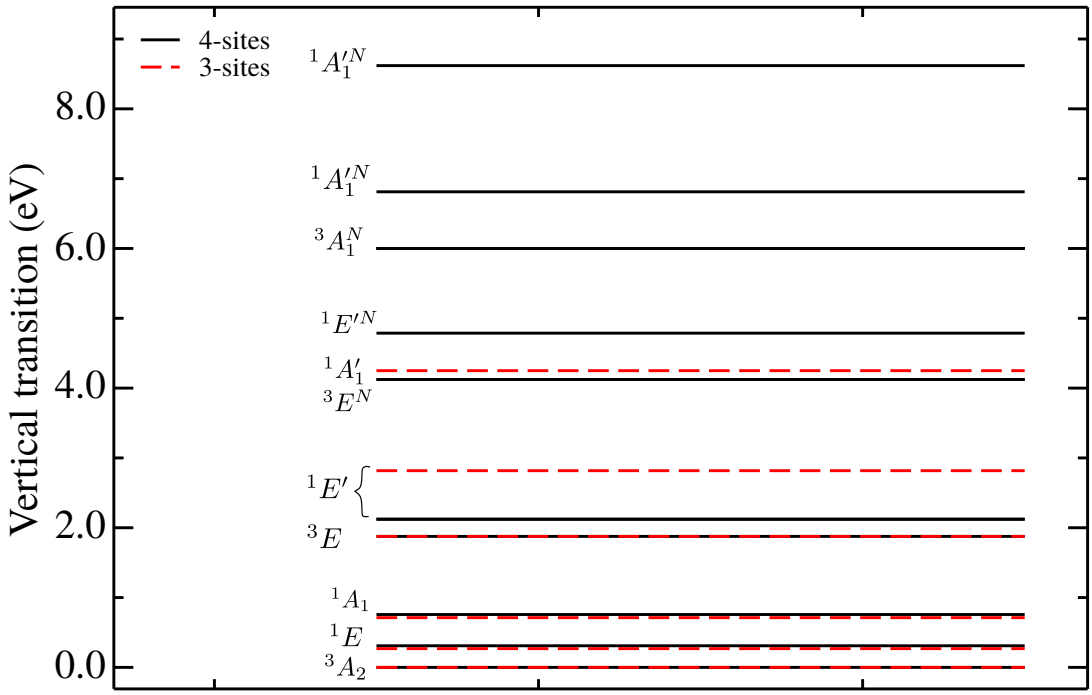

Figure 6.2.14: Comparison of eigenenergies of the 3-site and 4-site model when both models fit onto the DFT-PBE references.

One can see from Fig. 6.2.14 that the low-lying excited many-body levels $^3A_2$, ^1E, $^1A_1$, ^3E calculated with the 3-site model and the 4-site model are in perfect agreement with each other. Of course, the levels $^3A_2$, ^3E and $^1A_1'$ are the same in both models because they are fit onto the same DFT references. However, the ^1E and $^1A_1$ singlet levels also come out in perfect agreement, a knowledge which could not be known before the present study.

d. Comparison of the model parameters

One should mention that although in Fig. 6.2.14 the two models are fit on DFT-PBE references, the corresponding parameters are different in the two models, as one can see from rows 1 and 3 of table 6.6. As discussed in section 6.2.1 (g) the on-site energy provides a mere shift of the eigenenergies and does not play an important role. The difference in the t_{CC} parameter between the 3-site and 4-site model is larger than the difference between PBE and HSE06 with the 3-site model. However, the $U - V$ parameter is close in both models.

I compare also my parameters of the 4-site model to those found in previous works of refs. [34] and [75] (rows 3, 4 and 5 of table 6.6). One can say that the t_{CC} and t_{CN} of my 4-site model are very close to those obtained with fit onto the GW quasiparticles [34] (rows 3 and 4 of table 6.2.14). One should mention that the difference in the sign of the hopping parameter and the on-site energy with respect to my results is because of the different sign convention in the corresponding terms of the Hamiltonian in my model and in refs. [34] and [75].

Table 6.6: Comparison of the Hubbard model parameters. Top part of the table: the 3-site and 4-site models of this work as fit onto DFT references and the 4-site models of refs. [a] [34] and [b] [75]. Bottom part of the table: reference values for the 3-site model as given by the Gedanken experiment and by the fit onto the experimental values, as discussed in section 6.2.1 (h2) and 6.2.1 (h3)

Parameters	ε_C (eV)	ε_N (eV)	$\varepsilon_C - \varepsilon_N$ (eV)	t_{CC} (eV)	t_{CN} (eV)	$U - V$ (eV)	U_C	U_N	V_{CC}	V_{CN}
3-sites PBE	0.0	-	-	0.630	-	1.216	-	-	-	-
3-sites HSE06	0.0	-	-	0.787	-	1.365	-	-	-	-
4-sites	-	-	1.486	1.136	0.609	1.219	-	-	-	-
4-sites GW [a]	-	-	2.56	-1.03	-0.68	2.6	3.43	3.43	0.83	0.83
4-sites B3LYP [b]	-7.59	-2.73	10.32	-3.68	-2.97		3.54	10.8	0.02	5.66
3-sites Gedanken PBE	0.0	-	-	0.630	-	4.1	-	-	-	
3-sites Gedanken HSE06	0.0	-	-	0.787	-	3.6	-	-	-	
3-sites EXP	0.0	-	-	0.645	-	4.19	-	-	-	

e. Discussion of the electronic correlation

In this section I want to discuss the values of the $(U - V)$ Hubbard parameter. To this end, I consider the experimental value of the ${}^1A_1 - {}^1E$ transition as a reference one, as was done in my Gedanken experiment in section 6.2.1 (h2) and in section 6.2.1 (h3) where the fit was performed on both ${}^3E - {}^3A_2$ transition and ${}^1A_1 - {}^1E$ transition experimental values. The model parameters found in these two cases are presented in the bottom part of table 6.6.

The electronic correlations contained in the $U - V$ parameter are underestimated in my model where the fit was done onto the DFT-PBE and HSE06 references (row 1-3 in table 6.6). Surprisingly, the $(U-V)$ parameter is also severely underestimated in the 4-site model fit onto the GW in ref. [34]. Furthermore, the parameter $U_C - V_{CC}$ found in ref. [75]

is close to the reference Gedanken HSE06. Extending the 4-site Hubbard model with the parameter $U_N - V_{CN}$ yields scattered values for this parameter (row 5 of table 6.6) but does not improve significantly the results.

One should mention that including additional effects in the theoretical model such as electron-hole interaction may have an influence on the transition energies. As discussed in section 6.2.1 (h2) Ma et al. [127] have shown that the $^1E'$ singlet state is strongly affected by the electron-hole interaction. Also, in section 6.2.3 (c) we have seen, that in my 4-site model, the $^1E'$ state is precisely much affected by the inclusion of the nitrogen site (see Fig. 6.2.14). In my 4-site model the $^1E'$ state appears to be quasi-degenerate with the ^3E triplet state within the precision of the calculation (Fig. 6.2.14). The same was also found in the work of Ma et al. [127]. Based on this result Ma et al. proposed an alternative mechanism for the intersystem crossing, involving the $^1E'$ level. This model would imply that the $^1E'$ state is the upper state in the singlet-singlet transition, substantiating my 4-site model result. In my results, the $^1A_1$ state never appears very close to the ^3E triplet state and is never quasi degenerate with ^3E as would be required for the intersystem crossing, contrarily to the result of my 4-site model. Thus, the $^1E'$ singlet state may better explain the intersystem crossing mechanism playing a crucial role in the optical dynamics of the NV^- center. However, this comes in opposition to the experimental study of Rogers et al. [33].

f. Conclusion

It was not obvious that the levels which I obtain purely from the 3-site and 4-site Hubbard models (such as singlets ^1E, $^1A_1$ and $^1E'$) should coincide.

I have shown that both models yield almost the same results for the low-lying ^1E and $^1A_1$ states, and that the only level for which the two models predict a different energy is $^1E'$ singlet state.

I have made a detailed comparison of the Hubbard parameters, that turn out to be different in the 3-site and 4-site model with the exception for $(U - V)$ parameter.

I have shown that my 3-site Hubbard model allows to gain a deep understanding on the value of the electronic correlations for the NV^- center. So far, the value of $(U - V)$ in the literature is underestimated with respect to the value one should find if one trusts the experimental results for the ZPL attributed to the $^1A_1 - ^1E$ transition.

Finally, I am, interested in studying the pressure dependence of the transitions that are observable experimentally at ambient pressure: the $^3E - ^3A_2$ and $^1E - ^1A_1$ transitions. Therefore, the fact that the two models give the same result for these transitions give us the possibility to concentrate only on the 3-site model, as will be discussed in the chapter 7.

6.3 The Hubbard model for the NV^0 center

6.3.1 The 3-site Hubbard model

a. Parameterization

The neutral NV^0 center contains one electron less that the negatively charged NV^- center. Thus, in the 3-site model one should accommodate 3 electrons on six spin orbitals. The Fock space of 3 electrons distributed between 3 sites is $C_3^6 = 20$ and the basis set is:

$$
\begin{aligned}
\phi_1 &= |0 \;\; \downarrow \uparrow\downarrow \rangle && S = -1/2 \\
\phi_2 &= |0 \;\; \uparrow \;\; \uparrow\downarrow \rangle && S = 1/2 \\
\phi_3 &= |0 \;\; \uparrow\downarrow \;\; \downarrow \rangle && S = -1/2 \\
\phi_4 &= |0 \;\; \uparrow\downarrow \uparrow \;\; \rangle && S = 1/2 \\
\phi_5 &= | \downarrow \;\; 0 \;\; \uparrow\downarrow \rangle && S = -1/2 \\
\phi_6 &= | \downarrow \downarrow \downarrow \rangle && S = -3/2 \\
\phi_7 &= | \downarrow \downarrow \uparrow \;\; \rangle && S = -1/2 \\
\phi_8 &= | \downarrow \uparrow \;\; \downarrow \rangle && S = -1/2 \\
\phi_9 &= | \downarrow \uparrow \;\; \uparrow \;\; \rangle && S = 1/2 \\
\phi_{10} &= | \downarrow \uparrow\downarrow \;\; 0 \rangle && S = -1/2 \\
\phi_{11} &= | \uparrow \;\; 0 \;\; \uparrow\downarrow \rangle && S = 1/2 \\
\phi_{12} &= | \uparrow \;\; \downarrow \downarrow \rangle && S = -1/2 \\
\phi_{13} &= | \uparrow \;\; \downarrow \uparrow \;\; \rangle && S = 1/2 \\
\phi_{14} &= | \uparrow \uparrow \;\; \downarrow \rangle && S = 1/2 \\
\phi_{15} &= | \uparrow \uparrow \uparrow \;\; \rangle && S = 3/2 \\
\phi_{16} &= | \uparrow \uparrow\downarrow \;\; 0 \rangle && S = 1/2 \\
\phi_{17} &= | \uparrow\downarrow \;\; 0 \;\; \downarrow \rangle && S = -1/2 \\
\phi_{18} &= | \uparrow\downarrow \;\; 0 \;\; \uparrow \;\; \rangle && S = 1/2 \\
\phi_{19} &= | \uparrow\downarrow \;\; \downarrow \;\; 0 \rangle && S = -1/2 \\
\phi_{20} &= | \uparrow\downarrow \uparrow \;\; 0 \rangle && S = 1/2
\end{aligned}
\tag{6.40}
$$

The *differencies* of the analytical eigenenergies with respect to the ground state are

$$\begin{array}{lll} \textit{Energy} & \textit{Symmetry} & \textit{Degeneracy} \\ \Delta E_1 = 0 & {}^2E & (g=4) \\ \Delta E_2 = \frac{1}{6} c_0\, {b_0}^{-1/3} + \frac{1}{6} {b_0}^{1/3} + f_0 - \frac{2}{3}\,(\mathrm{U}-\mathrm{V}) & {}^4A_2 & (g=4) \\ \Delta E_3 = \frac{1}{6} c_0\, {b_0}^{-1/3} + \frac{1}{6} {b_0}^{1/3} + f_0 + \frac{1}{3}(\mathrm{U}-\mathrm{V}) & {}^2A + {}^2A & (g=4) \\ \Delta E_4 = \frac{1}{2} c_0\, {b_0}^{-1/3} + \frac{1}{2} {b_0}^{1/3} + f_{1,0} & {}^2E & (g=4) \\ \Delta E_5 = \frac{\sqrt{3}}{3} d_0 {b_0}^{-1/3} & {}^2E & (g=4) \end{array} \tag{6.41}$$

where I have used the following notations

$$\begin{aligned} a_0 &= -243\, t^4 - 27\, t^2\,(\mathrm{U}-\mathrm{V})^2 - (\mathrm{U}-\mathrm{V})^4 \\ b_0 &= 9\,\sqrt{a_0}\, t - (\mathrm{U}-\mathrm{V})^3 \\ c_0 &= 27\, t^2 + (\mathrm{U}-\mathrm{V})^2 \\ d_0 &= -{b_0}^{2/3}\,\mathrm{i} + t^2\, 27\mathrm{i} + (\mathrm{U}-\mathrm{V})^2\,\mathrm{i} \\ f_0 &= \frac{\sqrt{3}\, d_0}{6\, {b_0}^{1/3}} \end{aligned} \tag{6.42}$$

By solving the equation ΔE_2 with respect to the parameter t, we get:

$$t = \tfrac{1}{2}\,(\Delta \mathrm{E}_2 - (\mathrm{U}-\mathrm{V}))\,\sqrt{\frac{4\,\Delta \mathrm{E}_2}{9\,\Delta \mathrm{E}_2 - 6\,(\mathrm{U}-\mathrm{V})}} \tag{6.43}$$

One can associate ΔE_2 with the ${}^4A_2 - {}^2E$ transition between quartet first excited level and doublet ground state. The ${}^4A_2$ state can be, in principle, calculated in the DFT, as it was done in the ref. [74]. The single Slater determinant can be constructed by aligning all electrons with spin-up in the configuration $a_1^N(2)a_1(1)e(2)$ to obtain M_s=+3/2. However, it is not obvious that the ground state doublet ${}^2E$ of the NV^0 can be calculated in the DFT. Gali *et al.* have shown that the single Slater determinants $a_1^N(2)a_1(2)e_x(1)$ or $a_1^N(2)a_1(2)e_y(1)$ are the true orthonormal eigenstates of the ${}^2E$ ground state of the C_{3v} group. Their calculated quartet ${}^4A_2$ level is 0.86 eV higher the ground state. Gali *et al.* mention however, that because of the strong correlation interaction of the ${}^2E$ ground state with ${}^2E$ excited states, calculated in DFT, the ${}^4A_2 - {}^2E$ transition might be underestimated. My DFT HSE06 calculation yields 0.44 eV ${}^4A_2 - {}^2E$ transition, which is underestimated with respect to Gali's *et al* calculation by a factor of two. For the Fock space of the 3-site model I cannot associate another transition that can be calculated from the DFT. This results in a situation where we have more parameters in the model than the reference energy transitions to fit these parameters. In this case, I cannot use the method that has been applied in the case of the NV^- center.

In order to calculate the many-body states of the NV^0 center I make the hypothesis that the parameters do not change when modeling the NV center in the different charged states. Indeed, this is reasonable because these parameters should mainly be system-dependent. So, one can apply the same parameters found for NV^- but change the basis functions.

b. Results

I diagonalize numerically the Hamiltonian of the system in order to find the many-body states of the NV^0 center at ambient pressure. I do not show the Hamiltonian for the sake of simplicity. My results are summarized in Table 6.7. The ground state ^2E is shifted to zero. One can see that my results predict the quartet $^4A_2$ that is the first excited state in my model, 1.22 eV above the ground state. Also I find the state with ^2A symmetry in the manifold of low lying states, 2.44 eV above the ground state. This is in a reasonable agreement with the experimental ZPL 2.156 eV. I remind, however, that our calculated quantity is a vertical excitation and should not be directly compared to the ZPL, which only provide the lower bound.

Table 6.7: The 3-site Hubbard model for the NV^0 center. Energy of vertical transitions between many-body excited states and the ^2E ground state.

Symmetry	Hub.+PBE (eV)	Degeneracy
^2E	4.03	4
$^2A +^2 A$	2.44	4
^2E	2.07	4
$^4A_2$	1.22	4
^2E	0.0	4

The group theory considerations dictate that the NV^0 center contains the following many-body states $a_1^N(2)a_1(2)e(1)$: ^2E, $a_1^N(2)a_1(1)e(2)$: $^4A_2$, $^2A_2$, ^2E and $^2A_1$. One can see from Table 6.7 that my 3-site model one cannot discriminate between the $^2A_1$ and the $^2A_2$ excited doublets, but instead one find the four times degenerate doublet of A symmetry. Since the state of A symmetry cannot be four times degenerate, I suppose that in my 3-site model, $^2A_1$ and $^2A_2$ excited doublets have accidental degeneracy. This might be due to the fact that the 3-site model provides a not large enough Fock space. Therefore, in the section 6.3.2 I study NV^0 using the 4-site Hubbard model.

c. Previous data

Contrarily to the NV^- center case, there was only a small number of theoretical studies of the many-body states of the NV^0 center. Using the 4-site Hubbard model, with parameters calculated through the direct calculation of the interaction integrals in the local basis, Ranjbar *et al.* [75] have predicted the following ordering of the many-body states: $^2E^{GS}$, $^4A_2$, $^2A_1$, ^2E, $^2A_1$, ^2E. Earlier, Zyubin *et al.* [132] had used various theoretical methods and basis sets and using finite model NC_nH_m clusters. Using the CASPT2 calculations Zyubin *et al.* predicted the following ordering: $^2E^{GS}$, $^2A_2$, ^2E, $^2A_1$, ^2E. It is clear that there are some discrepancies between my work and previous calculations. One should mention also that in the previous works, the value of the optical transition has been misidentified, being

assigned to the ${}^2A_1 - {}^2E$ transition. This erroneous identification has been circulating in the literature for a long time [74, 75]. The recent experimental study of the ZPLs under strain, combined with the study of the polarization of split ZPLs allowed, finally to assign the optical transition to the ${}^2A_2 - {}^2E$ transition [76]. Among the two previous theoretical works, only Zyubin *et al.* has predicted the low-lying excited state of the proper orbital symmetry ${}^2A_2$ giving the optical transition of 2.4 eV, whereas in Ranjbar's *et al.* work, all of the excited doublets of A symmetry have the A_1 orbital symmetry. However, Zyubin *et al.* have not predicted any excited quartets, which seems to be in disagreement with the experimental findings where the low lying quartet ${}^4A_2$ was observed in electron paramagnetic resonance for the NV^0 center in optically excited state. This low lying quartet is believed to be under the optically allowed excited doublet. This feature had been properly captured in Ranjbar's work.

d. Conclusion

In summary, until now there was no theoretical study that predicted both the features of the NV^0 centers many-body states: the proper symmetry of the optically active state ${}^2A_2$ and the existence of the quadruplet state ${}^4A_2$ below the optically active one. Our study predicts both these features.

6.3.2 The 4-site Hubbard model

a. Results

The Fock space of the NV^0 center in the 4-site model contains C_5^8=56 basis functions. With the help of the simplifications by intrinsic symmetry, we can reduce the 56×56 Hamiltonian matrix to the 2 matrices of 24×24 and 2 matrices of 4×4 that can be diagonalized separately. However, because of the complexity of the analytical expressions, I do not overload this manuscript and do not present my analytical solutions. Moreover, in the 4-site model similarly to the 3-site model, we cannot calculate enough DFT energy transitions in order to fit the model parameters. Therefore, I use the parameters of the 4-site model that have been found for the case of the negative NV^- center. I show, the many-body states of the NV^0 found with the 4-site model in Table 6.8.

Table 6.8: The 4-site Hubbard model for the NV^0 center. Energy of the vertical transition between many-body excited states and the ^2E ground state.

Symmetry	Hub.+PBE (eV)	Degeneracy
$^2A_1$	10.21	2
^2E	8.23	4
$^2A_1$	8.11	2
^2E	6.32	4
^2E	5.97	4
^4E	5.30	8
$^2A_1$	4.50	2
$^2A_2$	4.35	2
^2E	4.08	4
^2E	3.70	4
$^4A_2$	3.42	4
$^2A_1$	2.06	2
^2E	1.64	4
$^2A_2$	1.45	2
$^4A_2$	1.17	4
^2E	0.0	4

b. Discussion

One can see that in the case of the 4-site model as in the case of the 3-site model, I obtain that $^4A_2$ is the first excited state. However, the $^2A_2$ excited doublet is now 1.45 eV, which is underestimated with respect to the experimental optical transition of 2.156 eV. Contrarily to the NV^- case, I find that in the case of the NV^0 center the 3- and 4-site models do not agree with each other. The ordering given by the two models is slightly different. Because of the small availability of other theoretical methods, it is difficult to say which ordering is pertinent. Moreover, the ordering of the excited state doublet is not known from the experiment. Finally, my hypothesis that the model parameters should be insensitive to the charge of the system is a strong statement which might be questionable. Ranjbar *et al.* for example, have found that the on-site Coulomb interaction in the case NV^- and NV^0 was different [75].

c. Conclusion

To conclude, because of the discrepancies in the ordering of the excited doublet levels in the 3-site and 4-site models in the case of the NV^0 one cannot conclude on the level ordering. However, I believe that the NV^0 parameters should be very similar to those that I have used. Therefore, I believe that my choice of parameters is valid in order to estimate the pressure behavior of the NV^0 center.

6.4 Conclusions

In this chapter I have introduced a new 3-site model and a conventional 4-site Hubbard model for the NV center. The 3-site model has been developed and used for the first time in the present work. I can conclude that:

- I have shown that 3-site model is able to reproduce the low lying set of the many-body states of the NV^- center in very good agreement with the 4-site model. Moreover, my 3-site model contains less independent parameters than the 4-site model, and thus requires less DFT references to fit the parameters. This makes the 3-site model more attractive for the investigations of the pressure behavior of the NV center.

- The procedure to fit the Hubbard model parameters to the DFT references that has been proposed in the present work, can, in principle, be generalized to other defect systems, however, under the condition that the reference states of the system can be represented as a single Slater determinant.

- I have shown that in the case of NV^0 it is not possible to calculate enough DFT references in order to fit the Hubbard parameters. However, since the charge should not influence the parameters but rather should be taken into account through the basis set, I have undertaken a strategy to use for the NV^0 center the parameters found for the NV^- center. I have shown that this approach is not accurate enough to conclude firmly on the many-body level ordering of the NV^0 center. However, it is still can be used for the estimation of the pressure behavior on the NV^0 center.

CHAPTER 7

Effect of the hydrostatic pressure

In this chapter I apply the 3-site and 4-site Hubbard models developed in this work and presented in chapter 6 in order to study many-body excited states under a hydrostatic pressure. I first study the pressure behavior of those high energy excited states that can be calculated within the DFT, as it has been done in the chapter 5 for the energy transition between the ground state $^3A_2$ and the first excited triplet ^3E. I then study the many-body states under pressure using the Hubbard model. My Hubbard Hamiltonian does not contain terms that depends on pressure explicitly. I rather want to introduce the pressure dependence in the model through the pressure dependence of the model parameters. In order to include the pressure dependence, I combine the Hubbard model with my DFT calculations of the NV center under a hydrostatic pressure, as explained in chapter 5. Finally, I perform an exact diagonalization of the Hubbard Hamiltonian at each pressure, which gives me access to the pressure dependence of the multi-determinant excited states that cannot be calculated in the DFT. I compare the pressure dependence in both the 3-site and 4-site models. In addition, I then use Hubbard parameters found for the NV^- center in order to study the pressure dependence of the NV^0 center.

7.1 Many-body states of the NV^- center

a. Results

Fig. 7.1.1 (a) illustrates the behavior of the transition energy between the many-body excited states and the ground state under pressure calculated in this work with the DFT-PBE. The ground state energy is shifted to zero at each pressure. As I have already shown in chapter 4, the DFT predicts the pressure coefficient of the $^3E - ^3A_2$ transition in very good agreement with the experiment of ref. [16, 17, 67] (see table 2.1). Therefore, I have used the pressure dependence of the DFT reference transitions $^3E - ^3A_2$, $^3E^N - ^3A_2$, $^1A_1' - ^3A_2$, $^1A_1'^N - ^3A_2$ in order to parameterize my pressure-dependent Hubbard model (see Fig. 6.2.11).

I show the result for the 4-site model of NV^- in Fig. 7.1.1 (b). I highlight with black color, the levels that were fit to reproduce the DFT calculations, and which are thus the same as in panel (a). I highlight with red color the multi-determinant states that occur due to the multi-configurational nature of the Hubbard model basis set. Even though the $^3A_1^N$ state can be calculated in the DFT, I highlight it with red color, because I do not use it as a reference level, so it does not appear in Fig. 7.1.1 (a).

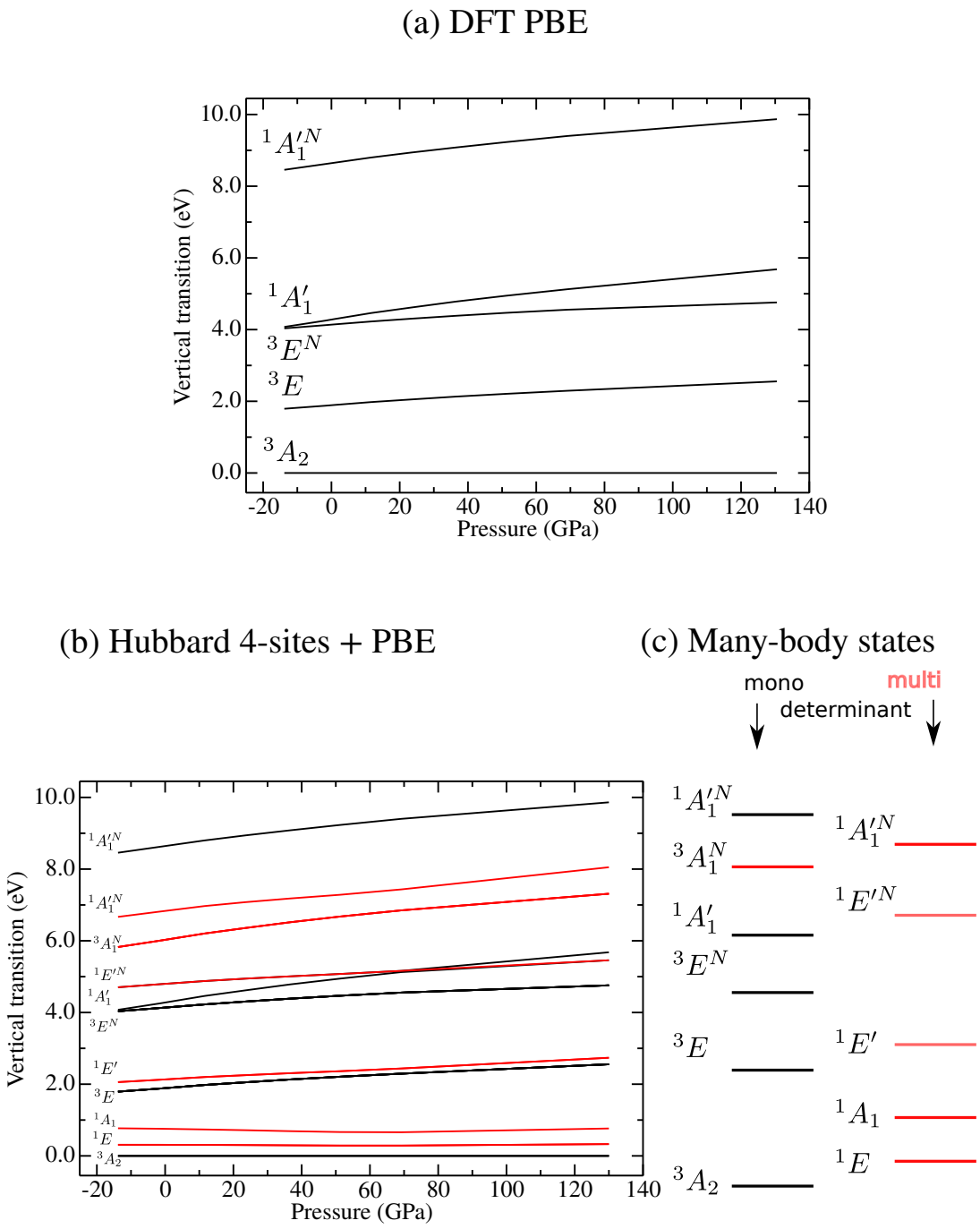

Figure 7.1.1: NV^- center. (a) Pressure dependence of the transition energy between the DFT-PBE calculated levels; (b) Pressure dependence found with the 4-site Hubbard model fit to the DFT-PBE. In both plots the ground state at each pressure has been normalized to zero. (c) Schematic representation of the many-body excited states that can and cannot be represented as a single Slater determinant.

Fig. 7.1.1 (c) schematically represents the many-body states of the NV^- center that can be represented as a single Slater determinant on the left column and those that cannot be - on the right one. I then compare the pressure behavior of the NV^- states obtained with the 3-site and 4-site model. This comparison is reported in Fig. 7.1.2.

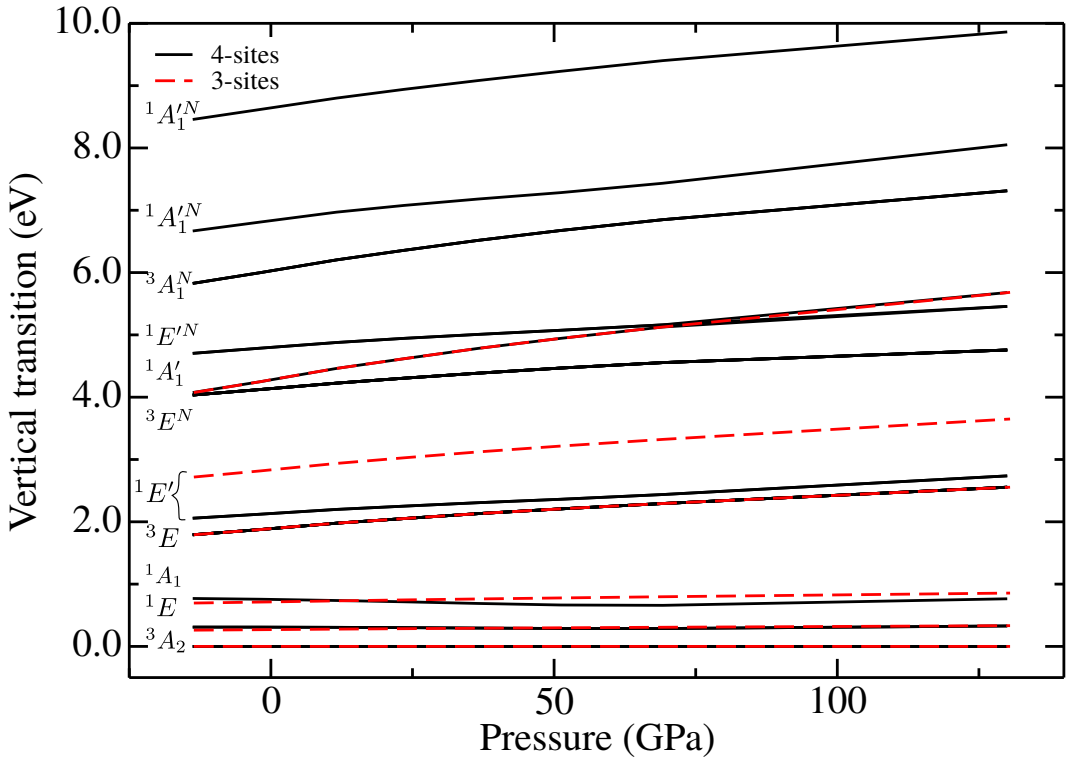

Figure 7.1.2: NV^- center. Comparison of the transition energy between the many-body excited states and the ground state calculated in the 4-site model (black solid line) and the 3-site model (red dashed line).

As I have shown in chapter 6, the 3-site and 4-site models predict the ordering of low-lying excited many-body levels in very good agreement with each other. One can see from the Fig. 7.1.2 that the pressure behavior of the low-lying excited many-body levels $^3A_2$, ^1E, $^1A_1$, ^3E calculated with the 3-site model and the 4-site model is also in very good agreement with each other. In Fig. 7.1.3 I show the pressure dependence of two transitions $^3E - ^3A_2$ and $^1A_1 - ^1E$ studied with the 3-site model fit both onto DFT-PBE and HSE06 calculations.

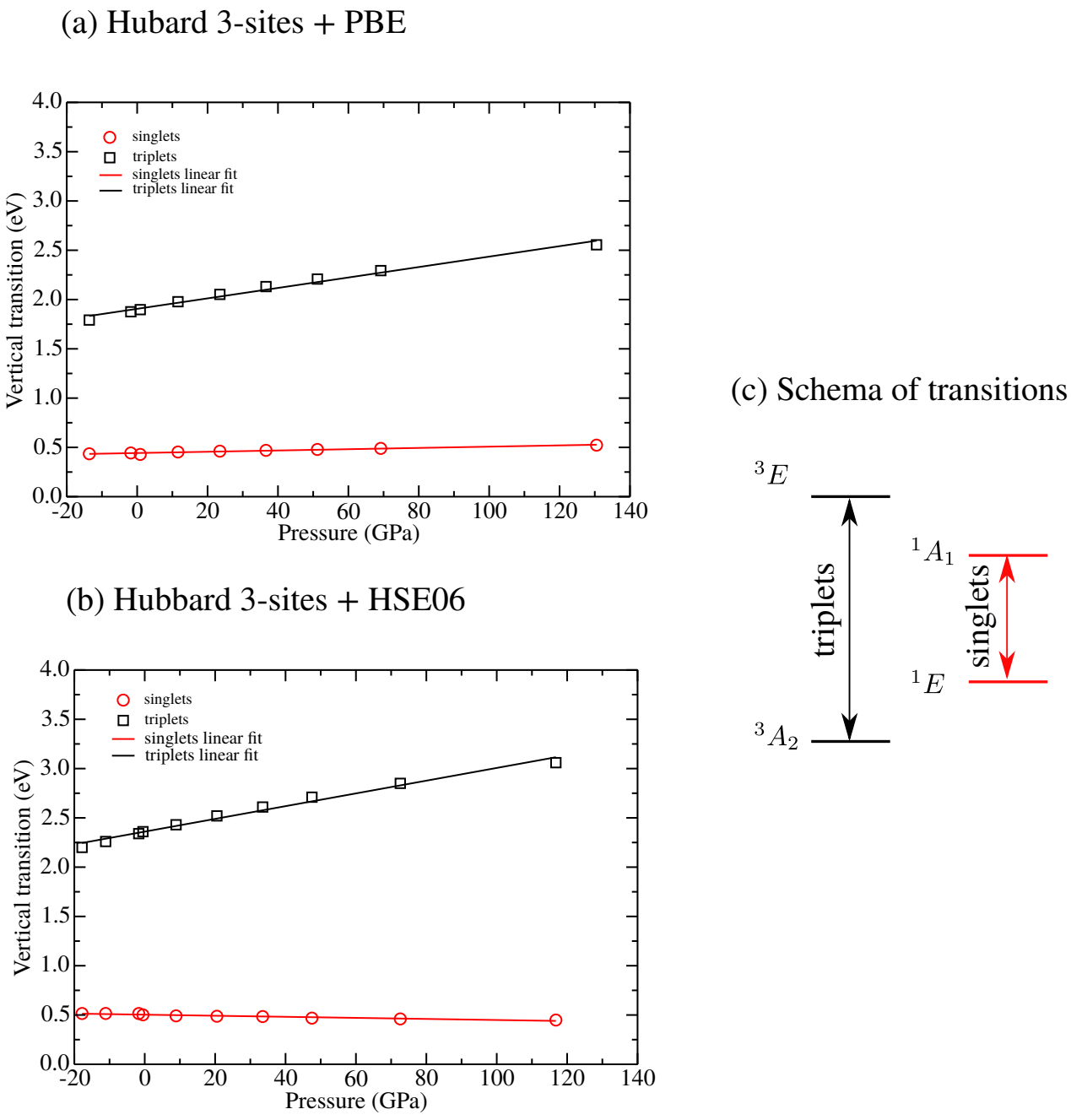

Figure 7.1.3: NV^- center. Pressure dependence of the triplet transition $^3E - ^3A_2$ and singlet transition $^1E - ^1A_1$ studied in the 3-site Hubbard model fit to both PBE (a) and HSE06 (b) calculations. (c) Schema explaining studied transitions.

My result of the pressure shift of the triplet-triplet transition is in very good agreement with the results of Doherty *et al.* as can be seen from Table 7.1. An important conclusion coming from my results is the very different behavior under the pressure of the triplet-triplet transition ${}^3E - {}^3A_2$ and the singlet-singlet ${}^1E - {}^1A_1$ one. Indeed, I have found, that the singlet-singlet transition is almost unchanged under the hydrostatic pressure. One should mention that this result has never been calculated nor observed experimentally before.

Table 7.1: NV^- center. Comparison of the pressure gradients of the vertical triplet-triplet and singlet-singlet transitions in the 3-site Hubbard model fit onto DFT-PBE and HSE06 (meV/GPa). [a] from ref. [17]. [b] from ref. [16]. [c] from ref. [67]

	296 K	**77 K**	**PBE**	**HSE06**
$E({}^3E) - E({}^3A_2)$	5.75 [a]	5.5 [b]	5.2	6.4
	5.81 [c]	5.57 [c]		
$E({}^1A_1) - E({}^1E)$	-	-	0.6	-0.5

b. Analysis of the molecular model

I have also made the important observation that all many-body excited states that originate from the same defect orbital configuration have the same pressure coefficient, as summarized in Table 7.2. To this end, I use the molecular model presented in section 2.5. For example, the many-body states ${}^3A_2$, ${}^1E$, ${}^1A_1$ belong to the same defect orbital configuration $a_1(2)e(2)$ and they all have almost the same pressure coefficient. I believe that the slight differences in the pressure coefficients for this set of states is due to the accuracy limitations. So, the pressure has the same effect on the levels ${}^3A_2$, ${}^1E$, ${}^1A_1$, and therefore, we find that the ${}^1E - {}^1A_1$ transition energy stays almost constant as a function of pressure. Whereas the ${}^3E$ and ${}^1E'$ states belong to the $a_1(1)e(3)$ configuration and they also have the same pressure coefficient. But when we think about the triplet-triplet transition ${}^3E - {}^3A_2$, the two states belong to different defect molecule configurations and are influenced in a different way by pressure, thus there is a shift of the optical transition under pressure.

One should mention that Rogers *et al.* [33] have studied the dependence of the triplet and singlet transitions under an uniaxial strains, as was discussed in chapter 2, section 2.4.1. Although they have not studied the effect of a hydrostatic pressure on the triplet-triplet and singlet-singlet transitions, they have proposed the following statement using their molecular model. If the symmetry is not changed by the applied stress (as it is the case for the hydrostatic pressure), it will only alter the a_1e energy separation. This will result in a change of the energy separation between configurations but causes no change within each configuration.

Rogers *et al.* have consideredhe example of the interaction in relation to the singlet-singlet transition. The ${}^1A_1$ ($a(2)e(2)$) - ${}^1E$ ($a(2)e(2)$) transition is between levels within the same $a(2)e(2)$ configuration and so the transition energy cannot be shifted by the hydrostatic strain.

My Hubbard model confirms the proposition that have been done by Rogers *et al.* [33].

Table 7.2: NV^- center. Pressure coefficients of all many-body states of the NV^- center

.

Configuration	$a_1^N(2)a_1(2)e(2)$			$a_1^N(2)a_1(1)e(3)$		$a_1^N(2)a_1(0)e(4)$	$a_1^N(1)a_1(2)e(3)$		$a_1^N(1)a_1(1)e(4)$		$a_1^N(0)a_1(2)e(4)$
Symmetry	${}^3A_2$	${}^1E$	${}^1A_1$	${}^3E$	${}^1E'$	${}^1A_1'$	${}^3E'^N$	${}^1E'^N$	${}^3A_1^N$	${}^1A_1'^N$	${}^1A_1'^N$
$\frac{dE(P)}{dP}$ $(\frac{meV}{GPa})$	0	0.06	0.2	5.2	4.6	9.7	5.0	5.1	10	9.3	9.7

c. Conclusion

In summary, in this section I performed a study of the pressure behavior of the many-body states of the NV^- center. I highlight the following important conclusions:

- I cross-checked one more time that the 3-site and 4-site model in the case of the NV^- center give the same results. The pressure behavior of the low-lying many-body states is in good agreement between each other in the two models.
- My results indicate that the pressure influences in the same way the states that originate from the same defect orbital configuration.
- As a consequence of the previous conclusion, the behavior of the optically observed singlet-singlet ${}^1A_1 - {}^1E$ and triplet-triplet ${}^3E - {}^3A_2$ transitions is very different.

7.2 Many-body states of the NV^0 center

a. Method

In this section, I use the same Hubbard model parameters for the NV^0 as for the NV^- center, as was explained in chapter 6. Therefore, I take parameters found for the NV^- center at each pressure and diagonalize the Hamiltonian of the NV^0 in the basis of the NV^0 center. Since in the chapter 6 we have seen that this technique leads to slight discrepancies between the 3- and 4-site models I investigate both of them under pressure.

b. Results

In Fig. 7.2.1 I present the pressure behavior of the many-body states of NV^0 obtained with 3-site and 4-site models. Looking at Fig. 7.2.1 one can make the same conclusion as I did for the NV^- center: namely, all many-body states originating from the same configuration of occupation of defect levels have almost the same pressure coefficient. This conclusion holds equally for the results obtained with the 3- and 4-site models. I summarize the results in Table 7.3.

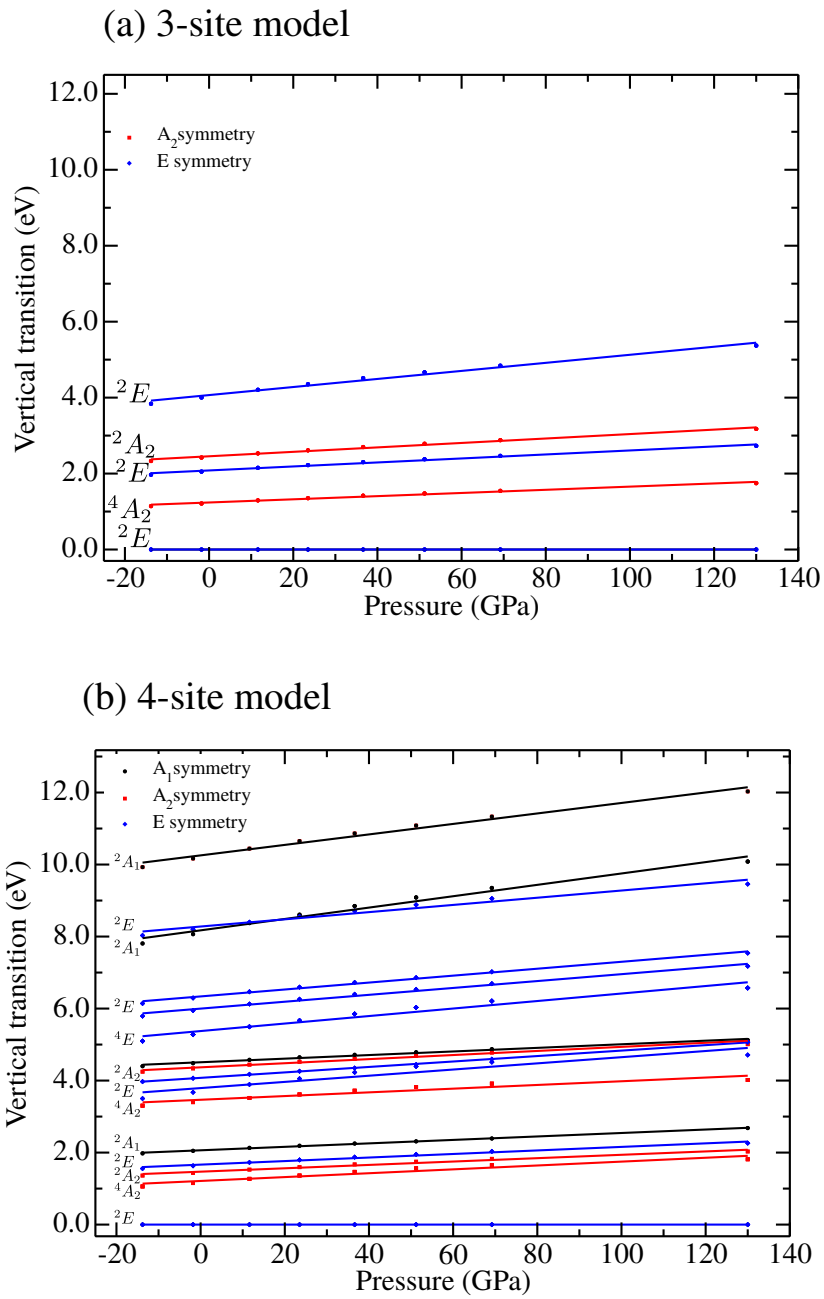

Figure 7.2.1: NV^0 center. Pressure dependence of the many-body states studied in the 3-site Hubbard model (a) and with the 4-site Hubbard model (b). The ground state level is normalized to zero at each pressure.

One can see from table 7.3 that the pressure dependence of the optical transition $^2A_2 - ^2E$ is predicted to be in the range of 4.6 - 5.8 meV/GPa when using the same parameters of the Hubbard model found for the NV^- center. Even though my choice to

use the parameters as in NV^- for NV^0 leads to some discrepancies in the level ordering obtained with the 3-site and 4-site models, we can see that the pressure coefficients are in a reasonable agreement between the two models. In addition, I confirm my observation that the many-body levels of the same molecular configuration are influenced in the same way by pressure. Therefore, since the $^4A_2$ low lying quartet state and the $^2A_2$ doublet state, responsible for the optical transition, are of the same molecular configuration $a_1^N(2)a_1(1)e(2)$ I can calculate the pressure behavior of the $^4A_2$ from the DFT. Indeed, as I explained in the chapter 6 the $^4A_2 - ^2E$ transition can be calculated directly using constrained occupation DFT. Therefore, I calculate the behavior of this transition under pressure directly from DFT and suppose that this behavior is the same for $^2A_2$ and $^4A_2$. This result is demonstrated in Fig. 7.2.2.

Our DFT calculations predict that the pressure coefficient of the $^4A_2 - ^2E$ vertical transition is 5.5 meV/GPa. This is in good agreement with the prediction of my Hubbard 3- and 4-site models, which yield respectively 5.3 meV/GPa and 4.2 meV/GPa (see table 7.3), and give results in the range of 4.2-5.3 meV/GPa for the first group of molecular orbitals (see table 7.3).

c. Conclusion

I conclude that:

- First, my DFT and Hubbard models are in good agreement for predicting the pressure coefficient of the $^4A_2 - ^2E$ vertical transition, this indicates that my assumption of using parameters found for NV^- in order to study the pressure behavior of the NV^0 is reasonable.

- I have found that the use of the same parameters in the NV^- and NV^0 leads to the slight discrepancy in the ordering of the low lying doublets in the 3- and 4- site models. If the Hubbard parameters I took for NV^0 were the true parameters of this system, I would expect the coincidence of the two 3- and 4-site models, as it was a case of the NV^- center. I think however, that the true NV^0 parameters should not very different from those that I have used. Thus, I cannot conclude on the levels ordering but the pressure behavior can be predicted by my model. Also, my model allows us to make an important conclusion about the influence of the pressure on levels of the same molecular configuration. This observation has allowed us to cross-check my model with my DFT calculation for NV^0 under pressure.

Table 7.3: NV^0 center. Pressure coefficients of all many-body states center.

Configuration		$a_1^N(2)a_1(2)e(1)$	$a_1^N(2)a_1(1)e(2)$				$a_1^N(1)a_1(2)e(2)$				$a_1^N(2)a_1(0)e(3)$	$a_1^N(1)a_1(1)e(3)$			$a_1^N(1)a_1(0)e(4)$	$a_1^N(0)a_1(2)e(3)$	$a_1^N(0)a_1(1)e(4)$
Symmetry	4 site	^2E	$^4A_2$	$^2A_2$	^2E	$^2A_1$	$^4A_2$	^2E	$^2A_1$	$^2A_2$	^2E	^4E	^2E	^2E	$^2A_1$	^2E	$^2A_1$
	3 site	^2E	$^4A_2$	$^2A_2$	^2E						^2E						
$\frac{dE(P)}{dP}$ $(\frac{meV}{GPa})$	4 site	0.0	5.3	4.6	4.9	4.8	5.1	7.5	5.0	5.7	8.3	10.4	9.5	9.6	15.7	9.4	14.5
	3 site	0.0	4.2	5.8	5.2						10.6						

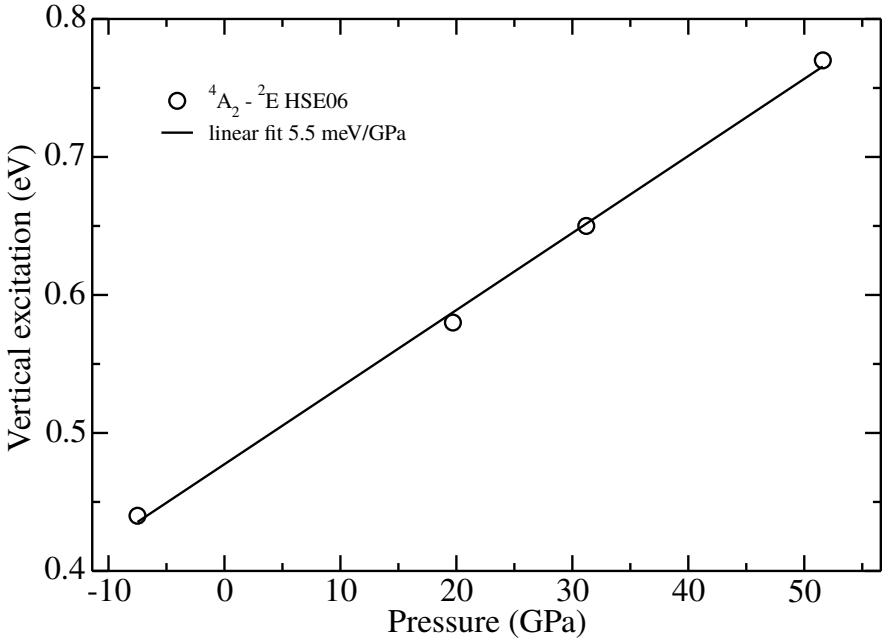

Figure 7.2.2: Nv^0 center. Pressure dependence of the $^4A_2 - ^2E$ transition of the NV^0 center in DFT-HSE06.

7.3 Conclusions

In this chapter I studied the pressure behavior of the many-body states of the negatively charged NV^- center and neutral NV^0 center. The pressure dependence was introduced through the fitting of the Hubbard parameters to the pressure dependent DFT transition energies.

I have shown that in both systems I can make an important observation: the pressure behavior of the states originating from the same defect orbital configuration is the same. This conclusion results in a very different pressure behavior of the singlet-singlet and triplet-triplet transitions of the NV^- center. This fact might have the important consequences on the application of the NV center as a magnetic sensor. For example, one can tentatively link the loss of the ODMR contrast (see section 2.3.1) to the difference of the pressure behavior of the singlet-singlet and the triplet-triplet transition. The ODMR contrast is believed to be caused by the intersystem crossing between the excited triplet state ^3E and excited singlet state $^1A_1$. My observation that under pressure the energy gap between these two states increases does not directly says that the intersystem crossing should decrease, to make such a conclusion one should to account for electron-phonon interaction and spin-orbit couplings. However, my observation gives a hint that this could be one of the possible reasons of the ODMR contrast loss.

In the case of the NV^0 I have used the parameters found for NV^-. I have shown that this choice is reasonable in order to study the pressure behavior of the optical transition $^2A_2 -^2 E$, even though I cannot conclude on the level ordering. This conclusion was cross-checked through the calculation of the pressure dependence of the quartet state $^4A_2$ directly with DFT, because of the fact that $^4A_2$ and $^2A_2$ states originate from the same molecular orbital configuration and must have the same pressure behavior according to my observation.

CHAPTER 8

Conclusions and perspectives

To conclude, in this work I have developed and compared the results of two Hubbard models used to study the NV center. I have used both the conventional 4-site Hubbard model and my 3-site model that is reported for the first time. I have presented both analytical and numerical solutions of the two models.

The analytical solution allowed me to obtain the analytical expressions of the Hubbard parameters as a function of the DFT total energies. In order to find the manifold of the many-body states of the NV^- center, the Hubbard model was parameterized through the fitting to the DFT total energies. I have shown that in the case of NV^-, the 3- and 4-site models are in good agreement with each other and with previous theoretical studies with respect to the low-lying many-body states ordering. Moreover, I have pointed out that the advantage of the 3-site model over the 4-site model is its simplicity since it contains only 2 parameters and can be directly fit onto experiment with no *ad hoc* assumption.

In the case of the neutral NV^0 center, I have shown that it was not possible to apply the same fitting procedure because not enough DFT references are accessible for this system. The approximation I have applied in order to calculate the many-body states of the NV^0 center consisted in the supposition that the Hubbard parameters of the NV^0 center should be the same as for the NV^- center. I have found that this approach can be used for the estimation of the pressure behavior on the NV^0 center.

Finally, the effect of the hydrostatic pressure on the many-body states have been studied for the NV^- and NV^0 centers. For both systems I have observed that the hydrostatic pressure does not produce a shift between the many-body states within the same molecular configuration, but rather between the states of different molecular configurations. In the case of the negative NV^- center, the previous observation leads to the important consequences that the singlet transition ${}^1A_1 - {}^1E$ and triplet transition ${}^3E - {}^3A_2$ behave very different under the hydrostatic pressure. This difference in the behavior can have an important influence on the intersystem crossing for ${}^3E - {}^1A_1$ and ${}^1E - {}^3A_2$ transitions.

In the case of the neutral NV^0 center, the conclusion about the influence of the hydrostatic pressure with respect to the molecular configurations allows to crosscheck the result of the Hubbard models. Due to the fact that the non optical quartet ${}^4A_2$ state and the optical excited doublet ${}^2A_2$ state belong to the same molecular configuration, they should have the same pressure behavior. Since among these two states only ${}^4A_2$ can be calculated with DFT, I have studied its pressure behavior within DFT and I have confirmed the validity of 3-site and 4-site Hubbard models. So, finally I have found that the pressure coefficients of the optical transition of the NV^- and NV^0 centers are almost the same

under the hydrostatic pressure.

There are two perspectives which I would like to discuss about the possible extensions of my model. The first perspective deals with the inclusion of the electron-phonon coupling. In fact, in order to explain the difference of the pressure coefficients of the triplet-triplet and the singlet-singlet transition of the NV^- center more in detail, one should take into account an important aspect when talking about the optical transitions. The change of the electronic configuration is followed by the relaxation of the ionic configuration. As it was shown earlier [34, 118], and confirmed with my DFT calculations, in the ground state relaxed configuration carbon atoms are located closer to vacancy than the nitrogen, whereas in the ^3E excited state I observe an opposite pattern: the nitrogen relaxes inwards and carbon atoms outwards. This leads to the fact that the equilibrium ionic configuration is very different in the ground and in the first excited triplet. Since the optical transition is very sensitive to the ionic configuration, the additional change of the lattice nuclei positions under pressure shifts the optical transition energy. However, my Hubbard model does not take into account the ionic relaxations. The relaxations occur through the interaction with phonons, thus a possible solution is to include the ionic relaxations into the Hubbard model by adding of the electron-phonon interaction term into the Hamiltonian. This extension to the Hubbard model is called the Hubbard-Holstein model [146]. It was successfully applied and parameterized through DFT in order to study the K3 picene molecule [147]. However, such a study never performed for the NV center in diamond and it is out of the scope of this work. Nevertheless, I think it would be important to perform this study in perspective.

The second perspective deals with the extension of the study to a uniaxial pressure. In the present work, I have studied the effect of a hydrostatic pressure on the many-body states of the NV center. My study is in very satisfactory agreement with the experiments reported in refs. [16, 17, 67] where the pressure applied on NV centers was hydrostatic because the NV centers were located inside the chamber of the diamond anvil cell. The recent works in ref. [63] and in ref. [15] indicate that the pressure could be non hydrostatic inside the diamond of the anvil cell and would rather be an effective P_{eff} which is probably uniaxial. Thus, because the implanted NV centers are not located inside the diamond anvil cell chamber but inside the diamond itself, the pressure felt by the NV centers could contain non hydrostatic components, whose precise determination is still lacking. We have seen in section 2.4 that new effects appear in optical properties when applying a uniaxial pressure. The shifts and splittings of ZPL are different with respect to the hydrostatic conditions and depend on the axis along which the pressure was applied.

Thus, to account for non-hydrostatic stress in my Hubbard model, I have identified two approaches:

- Firstly, the ZPL pressure coefficient obtained with the experiment where the NV centers feel the uniaxial pressure can be re-scaled in a way to reproduce the pressure coefficient under hydrostatic conditions, and the so-determined scaling factor may be applied to all of the many-body states of my model.

- Secondly, in order to compare the pressure behavior of the many-body levels found with my model to experiments where a uniaxial stress is present one needs to fit the

Hubbard model to DFT calculations performed under a uniaxial pressure. Consequently, one has to distinguish between the case of "hidden anisotropy", where the C_{3v} symmetry is preserved by the effect of averaging the orientation of several NV centers, for which my model is valid; and the case of one isolated center, which has some anisotropy. In the latter case the model requires some extensions to account for the reduction of the symmetry to the C_s point group.

Finally, my model can be extended to study other defects in diamond as well as deep level centers in other materials like silicon carbide.

Appendix

This appendix is to provide the details on the pseudopotentials that have been generated in the present work and have been used in the calculations, as discussed in section 5.1.

8.1 Pseudopotentials

8.1.1 Performance of available pseudopotentials

In this section, the discussion is made about the impact of different pseudopotentials on the calculation of the same system.

Five pseudopotentials available in the PSlibrary [137] were selected in order to test the lattice parameter relaxation in the diamond structure. Table 8.1 summarizes properties of selected pseudopotentials and figure 8.1.1 represents the plot of the total energy as a function of lattice parameter.

One can mention from the plot, that different pseudopotentials have different values of the equilibrium lattice parameter and of bulk modulus. Lattice parameters are specified in the table and compared to the experimental value [148]. The error of lattice parameter with respect to the experimental value is within 1%, which is acceptable for calculations. However, we can see that the calculated results depend on the choice of the pseudopotential. The best reproducibility of the experiment is found for C-EB.pw used for boron carbide in refs. [149–152], C.pz-vbc.UPF and C.pbe-rrkjus.UPF pseudopotentials.

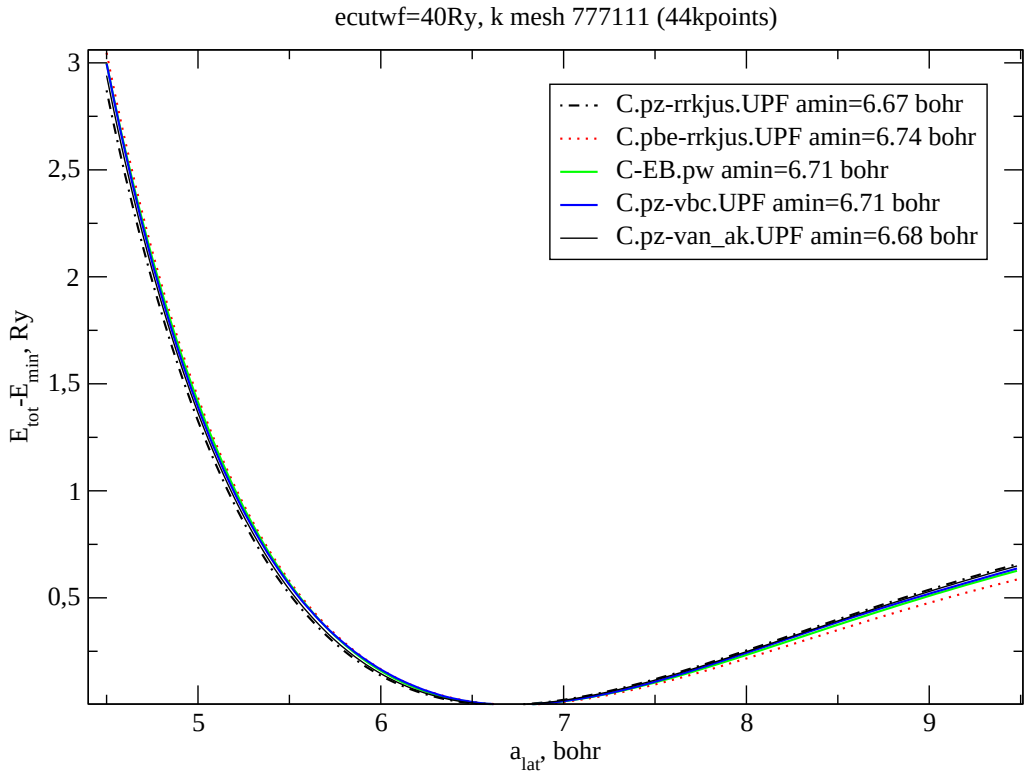

Figure 8.1.1: Total energy as a function of lattice parameter for different pseudopotentials.

Table 8.1: Properties of pseudopotentials

Name	Configuration	XC	method	N projectors	$r_c 2s^0$,a.u.	$r_c 2s^2$	$r_c 2p^0$	$r_c 2p^2$	$r_c 3d^{-2}$	lloc	lnloc	grid	a_{eq}^{lat} a.u.	$\frac{th-exp}{exp}$, %
Experiment													6.74	
C-EB.pw	$2s^2 2p^2$	LDA	NC	1		1.74		1.74		1	0	851	6.71	-0.45
C.pz-vbc.UPF	$2s^2 2p^2$	LDA	NC	1		0		0		1	0	269	6.71	-0.45
C.pz-rrkjus.UPF	$2s^2 2s^0 2p^2 2p^0 3d^{-2}$	LDA	US	4	1.6	1.6	1.6	1.6	1.3		0,0,1,1	1425	6.67	-1.04
C.pbe-rrkjus.UPF	$2s^2 2s^0 2p^2 2p^0 3d^{-2}$	PBE	US	4	1.6	1.6	1.7	1.7	1.7		0,0,1,1	627	6.74	0
C.pz-van_ak.UPF	$2s^2 2p^2$	LDA	US van	4		1.1		1.1			0,0,1,1	721	6.68	-0.89

One should mention here, however, that selected pseudopotentials differ by many parameters from each other. Among those parameters the number of points in the radial grid, the cut off radii of projectors, the exchange-correlation approximation and the method of pseudopotential construction. In principle, the disagreement in results is expected. Therefore, the next subsection is devoted to the understanding of the impact of the parameters of the pseudopotential on the error in the calculation of lattice parameter.

8.1.2 Generation of pseudopotentials with reduced errors

a. Objectives

In previous section the pseudopotentials were hardly comparable. The aim of present section was to see the impact of adding a $3d$ projector. The idea was to generate $2s2p$ and $2s2p3d$ pseudopotentials which would be comparable, meaning that all other parameters are the same. For simplicity, the norm-conserving C-EB.pw pseudopotential have been taken as a reference and its copy was generated, also, the same pseudopotential but containing $3d$ projector was generated. Another point of this section is to understand the impact of internal pseudopotential parameters on its performance. When generating the pseudopotential one should choose which component of the orbital moment will be attributed to the local part of the pseudopotential, and which to the nonlocal one. Therefore, pseudopotentials with different combination of component per local and nonlocal part of the potential were generated. For each pseudopotential, the cut off radius of wave function of each orbital moment was varied between 1.74 a.u. and 1.3 a.u.. A total, 44 pseudopotentials were studied. The table 8.1.2 shows lattice parameters and errors with respect to the experimental value.

b. Performance criterion

As a first criterion of the pseudopotential performance, the relative error of the total energy of the atom as a function of the cut off radius was chosen. However, it turned out that it does not correlate with the error on lattice parameter. So in the solid phase, for example, pseudopotentials with larger error because of the cut off radius were giving better results for lattice parameters. Thus, the differences in total energies for potentials with different cut off radii was not taken as important and only the error on the lattice parameters were considered.

c. Results

An interesting observation was done: if to vary the cut off radius of wave function with l, this variation influences the profile of the local part of the potential only if its l is the same of what we change the radius. This is natural behavior, since the wave function is related to the eletronic density which can influence the potential.

It was found from this study that for the NC pseudopotential the addition, to the configuration, of the non occupied $3d$ orbital leads to the rise of the lattice parameter error

when keeping the same cut off radii as in $2s2p$ case. However, it is possible to recover again a smaller value of the error when reducing the cut off radius for all s, p, d components to the 1.3 a.u.. This works for any value of local potential (lloc), however, the lloc=1 comparing to lloc=0, or lloc=2 seems to result in the smallest errors on the calculated lattice parameter calculation.

As a result of this work, two pseudopotentials were chosen for future calculations. One $2s2p$ with 1.74 a.u. cut off radii for each l component and one $2s2p3d$ with 1.3 a.u. cut off radii for each component.These two pseudopotentials given an error on the lattice parameter of 0.45%.

Comparison of $2s2p$ and $2s2p3d$ pseudopotentials with different cut off radii.

Name	Configuration	XC	method	N projectors	$r_c 2s^0$ a.u.	$r_c 2s^2$	$r_c 2p^0$	$r_c 2p^2$	$r_c 3d^{-2}$	$\Delta E_{ps}^{s,p,d}$	lloc	lnloc	grid	a_{eq}^{lat} a.u.	$\frac{th-exp}{exp}$, %
Experiment														6.74	
C-EB.pw	$2s^2 2p^2$	LDA :	NC	1		1.74		1.74			1	0	851	6.71	-0.45
C.my.rrkjnc.UPF	$2s^2 2p^2$	LDA	NC	1		1.74		1.74			1	0	887	6.71	-0.45
C.my.rrkjnc.UPF	$2s^2 2p^2$	PBE	NC	1		1.74		1.74			1	0	887	6.79	+0.74
C.my.rrkjnc.UPF	$2s^2 2p^2$	LDA	NC	1		1.3		1.3			1	0	887	6.71	-0.45
C.my.rrkjnc.UPF	$2s^2 2p^2$	PBE	NC	1		1.3		1.3			1	0	887	6.78	+0.89
C.my.rrkjnc.UPF (3d)	$2s^2 2p^2 3d^{-2}$	LDA	NC	2		1.3		1.3	1.3		1	0,2	887	6.71	-0.45
C.my.rrkjnc.UPF (3d)	$2s^2 2p^2 3d^{-2}$	PBE	NC	2		1.3		1.3	1.3		1	0,2	887	6.77	+0.45
C.my.rrkjnc.UPF (3d)	$2s^2 2p^2 3d^{-2}$	LDA	NC	2		1.74		1.74	1.74		1	0,2	887	6.68	-0.89
										$1.3 \cdot 10^{-4}$					
									1.6		1	0,2		6.68	-0.89
										$7.8 \cdot 10^{-5}$					
									1.5					6.68	-0.89
										$1 \cdot 10^{-4}$					
									1.4					6.68	-0.89
										$7.2 \cdot 10^{-5}$					
									1.3					6.68	-0.89
								1.74	1.3					6.68	-0.89
										$1.9 \cdot 10^{-2}$					
								1.6	1.3					6.67	-1.04
										$2.6 \cdot 10^{-3}$					
								1.5	1.3					6.67	-1.04
										$1.1 \cdot 10^{-2}$					
								1.4	1.3					6.67	-1.04
										$1.6 \cdot 10^{-2}$					

		1.3	1.3				6.71	-0.45
		1.3	1.74	$3.4 \cdot 10^{-4}$			6.67	-1.04
		1.3	1.6	$1.6 \cdot 10^{-4}$			6.67	-1.04
		1.3	1.5	$1.8 \cdot 10^{-4}$			6.67	-1.04
		1.3	1.4				6.67	-1.04
	1.74	1.6	1.3				6.67	-1.04
		1.3		$2.2 \cdot 10^{-2}$			6.71	-0.45
				$2.2 \cdot 10^{-2}$				
	1.6	1.6	1.3				6.69	-0.74
		1.3		$1.2 \cdot 10^{-2}$			6.71	-0.45
				$1.2 \cdot 10^{-2}$				
	1.5	1.6	1.3				6.68	-0.89
		1.3		$1.4 \cdot 10^{-2}$			6.71	-0.45
				$1.4 \cdot 10^{-2}$				
	1.4	1.6	1.3				6.67	-1.04
		1.3		$6.6 \cdot 10^{-3}$			6.71	-0.45
				$7 \cdot 10^{-3}$				
	1.3	1.6	1.3				6.67	-1.04
		1.3					6.71	-0.45
			1.74	$6.8 \cdot 10^{-4}$	2	0,1	6.64	-1.48
			1.6	$2.2 \cdot 10^{-4}$	2	0,1	6.64	-1.48
			1.5	$2 \cdot 10^{-4}$			6.64	-1.48
			1.4	$4.7 \cdot 10^{-4}$			6.64	-1.48
			1.3				6.64	-1.48

		1.74	1.3		2	0,1	6.64	-1.48
				$8.8 \cdot 10^{-3}$				
		1.6	1.3		2	0,1	6.65	-1.34
				$1.8 \cdot 10^{-3}$				
		1.5	1.3				6.67	-1.04
				$1.5 \cdot 10^{-2}$				
		1.4	1.3				6.67	-1.04
				$1.7 \cdot 10^{-2}$				
		1.3	1.3				6.67	-1.04
	1.74	1.6	1.3		2	0,1	6.65	-1.34
		1.3		$2.2 \cdot 10^{-2}$			6.67	-1.04
				$2.3 \cdot 10^{-2}$				
	1.6	1.6	1.3		2	0,1	6.65	-1.34
		1.3		$1.2 \cdot 10^{-2}$			6.67	-1.04
				$1.2 \cdot 10^{-2}$				
	1.5	1.6	1.3				6.67	-1.04
		1.3		$1.4 \cdot 10^{-2}$			6.67	-1.04
				$1.4 \cdot 10^{-2}$				
	1.4	1.6	1.3				6.67	-1.04
		1.3		$6.5 \cdot 10^{-3}$			6.71	-0.45
				$7 \cdot 10^{-3}$				
	1.3	1.6	1.3				6.67	-1.04
		1.3					6.71	-0.45
			1.74		0	1,2	6.58	-2.3
				$1.6 \cdot 10^{-4}$				
			1.6		0	1,2	6.58	-2.3
				$5.6 \cdot 10^{-4}$				
			1.5				6.59	-2.2
				$1.8 \cdot 10^{-4}$				
			1.4				6.59	-2.2
				$4.4 \cdot 10^{-5}$				
			1.3				6.59	-2.2

		1.74	1.3		0	1,2	6.59	-2.2
				$7.7{\cdot}10^{-3}$				
		1.6	1.3		0	1,2	6.61	-1.92
				$3.1{\cdot}10^{-3}$				
		1.5	1.3				6.62	-1.78
				$1.8{\cdot}10^{-2}$				
		1.4	1.3				6.64	-1.48
				$2.1{\cdot}10^{-2}$				
		1.3	1.3				6.67	-1.04
	1.74	1.6	1.3		0	1,2	6.64	-1.48
		1.3		$4{\cdot}10^{-2}$			6.67	-1.04
				$4.2{\cdot}10^{-2}$				
	1.6	1.6	1.3		0	1,2	6.64	-1.48
		1.3		$1.7{\cdot}10^{-2}$			6.67	-1.04
				$1.7{\cdot}10^{-2}$				
	1.5	1.6	1.3				6.65	-1.34
		1.3		$1.8{\cdot}10^{-2}$			6.67	-1.04
				$1.8{\cdot}10^{-2}$				
	1.4	1.6	1.3				6.67	-1.04
		1.3		$8.5{\cdot}10^{-3}$			6.71	-0.45
				$8.5{\cdot}10^{-3}$				
	1.3	1.6	1.3				6.67	-1.04
		1.3					6.71	-0.45

8.1.3 Impact of the exchange correlation approximation

The two most used approximations: local-density approximation (LDA) and generalized gradient approximation (GGA) have disadvantages. LDA always underestimates the volume while Perdew, Burke, Ernzherfor (PBE - one of the various flavors of the GGA approximations) often overestimates the lattice constants [153].

In order to understand the role played by the exchange correlation approximation, the two previously selected LDA pseudopotentials have been studied, and compared to the same pseudopotentials generated with the PBE approximation. The lattice parameter calculations were done with these four pseudopotentials. Table 8.3 shows results of the calculations and error with respect to the experiment.

Indeed, we can see that the LDA underestimates the value of lattice parameter and PBE overestimates. For the $2s2p$ pseudopotential PBE error turned out to be larger than the LDA. While for the $2s2p3d$ the absolute value of the error stayed the same. In both cases the error did not exceed 1%.

Table 8.3: Comparison of LDA and PBE pseudopotentials.

Configuration	XC	$r_c 2s^2$	$r_c 2p^2$	$r_c 3d^{-2}$	a_{eq}^{lat} a.u.	$\frac{th-exp}{exp}$, %
Experiment					6.74	
$2s^2 2p^2$	LDA	1.74	1.74		6.71	-0.45
$2s^2 2p^2$	PBE	1.74	1.74		6.79	+0.74
$2s^2 2p^2 3d^{-2}$	LDA	1.3	1.3	1.3	6.71	-0.45
$2s^2 2p^2 3d^{-2}$	PBE	1.3	1.3	1.3	6.77	+0.45

8.1.4 Transferability test

In the previous sections, the discussion was about the performance that the pseudopotentials can achieve in the solid state. Basing on results of this study four best NC pseudopotentials were chosen. In order to choose the best potential among this four, their performance inside atom was tested - the transferability test was performed. This test allows to estimate errors on the determination of energy levels when we excite electrons between these levels. The error is with respect to the all electron calculation. This test can be performed for the atom in neutral state as well as for the ionized one.

At the first step neutral state (valence charge is 4) of the diamond was tested for 2s-2p, 2p-3d and 2s-3d transitions. Energy level errors were studied. Table 8.1.4 shows all tested

configurations and related errors.

It was observed that for each pseudopotential both PBE and LDA, whatever the transition is (2s-2p, 2p-3d, 2s-3d) the errors on s and p levels $\Delta\epsilon^{2s}_{ae-ps}$, $\Delta\epsilon^{2p}_{ae-ps}$ always rise with increasing the number of electrons in the 2p level, the order of magnitude of the error for $\Delta\epsilon^{2s}_{ae-ps}$, $\Delta\epsilon^{2p}_{ae-ps}$ is in the same range (10^{-4} - 10^{-3} Ry). However, the error $\Delta\epsilon^{3d}_{ae-ps}$ is either very small (10^{-5}) or zero in the case where 3d transition takes place. Those errors are acceptable for our purposes. One should however be careful in the case of 2p-3d transition when we depopulate completely 2p level - the error exceeds out limit and becomes 10^{-2} order.

Comparing errors of eigenvalues for PBE and LDA approximations one should say that the absolute value of errors in the case of PBE is somewhat larger, but is of the same order of magnitude. Therefore, PBE approximation was considered to be not discussed further.

Since those pseudopotentials are going to be used in the calculation of defects in diamond and since defects usually have a charged state, the NV^- center for example, it is interesting to study how our pseudopotentials will behave in this case. Therefore, the same transferability test was repeated for the ionized configuration with the valence charge equal 3 and 3.5.

Tables 8.1.4 and 8.1.4 shows results of the transferability test for ionized configurations. It was found that for 2s-2p transitions values of $\Delta\epsilon^{2s}_{ae-ps}$ and $\Delta\epsilon^{2p}_{ae-ps}$ are almost the same for both ionized configurations, however, ΔE^{tot}_{ae-ps} is one order of magnitude larger in the case of valence charge equal 3. For the 2p-3d transition problem with 2p0 configuration became even worse in the case of ionized configurations since $\Delta\epsilon^{2s}_{ae-ps}$ and $\Delta\epsilon^{2p}_{ae-ps}$ exceeded 10^{-2} Ry error limit. Another configuration leading to the limit case the in 2p-3d transition was the 2p0.5 which gave $\Delta\epsilon^{2p}_{ae-ps}$ equal to 10^{-2} Ry.

Conclusion

To conclude, ionized configurations showed lower transferability in the case where 3d transitions are involved, compared to the neutral configuration. Thus, the pseudopotential that was used for calculations in the present manuscript was 2s2p PBE pseudopotential with the cut off radius of wave function of each orbital moment of 1.74 a.u..

Neutral state transferability test of four selected pseudopotentials.

Name	Configuration	ΔE^{tot}_{ae-ps}	$\Delta\epsilon^{2s}_{ae-ps}$	$\Delta\epsilon^{2p}_{ae-ps}$	$\Delta\epsilon^{3d}_{ae-ps}$	XC	Method	N proj.	$r_c 2s^2$	$r_c 2p^2$	$r_c 3d^{-2}$	lloc	lnloc	grid	a^{lat}_{eq} (a.u.)	$\frac{th-exp}{exp}$, (%)
Experiment															6.74	
C-EB.pw	$2s^2 2p^2$					LDA	NC	1	1.74	1.74		1	0	851	6.71	-0.45
C.my.rrkjnc.UPF	$2s^2 2p^2$					LDA	NC	1	1.74	1.74		1	0	887	6.71	-0.45
	2s2 2p2	0	0	0												
	2s1.5 2p2.5	$1.7{\cdot}10^{-4}$	$2.1{\cdot}10^{-4}$	$9{\cdot}10^{-4}$												
	2s1 2p3	$7.1{\cdot}10^{-4}$	$1.2{\cdot}10^{-4}$	$1.6{\cdot}10^{-3}$												
	2s0.5 2p3.5	$1.7{\cdot}10^{-3}$	$2.5{\cdot}10^{-4}$	$2.1{\cdot}10^{-3}$												
C.my.rrkjnc.UPF	$2s^2 2p^2$					PBE	NC	1	1.74	1.74		1	0	887	6.79	+0.74
	2s2 2p2	0	0	0												
	2s1.5 2p2.5	$3.3{\cdot}10^{-4}$	$2.6{\cdot}10^{-4}$	$1.1{\cdot}10^{-3}$												
	2s1 2p3	$1.4{\cdot}10^{-3}$	$1.1{\cdot}10^{-3}$	$1.9{\cdot}10^{-3}$												
	2s0.5 2p3.5	$3.1{\cdot}10^{-3}$	$1.6{\cdot}10^{-3}$	$2.3{\cdot}10^{-3}$												
C.my.rrkjnc.UPF (3d)	$2s^2 2p^2 3d^{-2}$					LDA	NC	2	1.3	1.3	1.3	1	0,2	887	6.71	-0.45
	2s2 2p2	0	0	0												
	2s1.5 2p2.5	$1.7{\cdot}10^{-4}$	$4.2{\cdot}10^{-4}$	$2.6{\cdot}10^{-4}$												
	2s1 2p3	$6.8{\cdot}10^{-4}$	$9.9{\cdot}10^{-4}$	$4.1{\cdot}10^{-4}$												

	2s0.5 2p3.5	$1.6{\cdot}10^{-3}$	$1.7{\cdot}10^{-3}$	$4.6{\cdot}10^{-4}$											
	2s2 2p2 3d-2	0	0	0											
	2s2 2p1.5 3d0.5	$9.5{\cdot}10^{-5}$	$1{\cdot}10^{-5}$	$5.4{\cdot}10^{-4}$	0										
	2s2 2p1 3d1	$7.9{\cdot}10^{-4}$	$9{\cdot}10^{-4}$	$2.6{\cdot}10^{-3}$	0										
	2s2 2p0 3d2	$9.6{\cdot}10^{-3}$	$1{\cdot}10^{-2}$	$1.9{\cdot}10^{-2}$	$1{\cdot}10^{-5}$										
	2s1.5 2p2 3d0.5	$4.2{\cdot}10^{-5}$	$1.8{\cdot}10^{-4}$	$1.4{\cdot}10^{-4}$	0										
	2s1 2p2 3d1	$1.8{\cdot}10^{-4}$	$4.1{\cdot}10^{-4}$	$8{\cdot}10^{-5}$	0										
C.my.rrkjnc.UPF (3d)	$2s^2 2p^2 3d^{-2}$					PBE	NC	2	1.3	1.3	1.3	1	0,2	887	6.77	+0.45
	2s2 2p2	0	0	0											
	2s1.5 2p2.5	$1.9{\cdot}10^{-4}$	$3.2{\cdot}10^{-4}$	$4{\cdot}10^{-4}$											
	2s1 2p3	$7{\cdot}10^{-4}$	$6.6{\cdot}10^{-4}$	$6.2{\cdot}10^{-4}$											
	2s0.5 2p3.5	$1.5{\cdot}10^{-3}$	$1.1{\cdot}10^{-3}$	$7.1{\cdot}10^{-4}$											
	2s2 2p2 3d-2	0	0	0											
	2s2 2p1.5 3d0.5	$1.1{\cdot}10^{-4}$	$2.5{\cdot}10^{-4}$	$6.4{\cdot}10^{-4}$	0										
	2s2 2p1 3d1	$9.3{\cdot}10^{-4}$	$1.4{\cdot}10^{-4}$	$3.1{\cdot}10^{-3}$	0										
	2s2 2p0 3d2	$1.1{\cdot}10^{-2}$	$8.6{\cdot}10^{-3}$	$2.6{\cdot}10^{-2}$	$2{\cdot}10^{-5}$										
	2s1.5 2p2 3d0.5	$4.7{\cdot}10^{-5}$	$2.9{\cdot}10^{-4}$	$4.7{\cdot}10^{-4}$	0										
	2s1 2p2 3d1	$3.8{\cdot}10^{-4}$	$1.2{\cdot}10^{-3}$	$1.2{\cdot}10^{-3}$	0										

3.5 valence charge state transferability test of two selected LDA pseudopotentials.

Name	Configuration	ΔE^{tot}_{ae-ps}	E^{2s}_{ae-ps}	E^{2p}_{ae-ps}	E^{3d}_{ae-ps}	XC	Method	N proj.	$r_c 2s^2$	$r_c 2p^2$	$r_c 3d^{-2}$	lloc	lnloc	grid	a^{lat}_{eq} a.u.	$\frac{th-exp}{exp}$, %
Experiment															6.74	
C-EB.pw	$2s^2 2p^2$					LDA	NC	1	1.74	1.74		1	0	851	6.71	-0.45
C.my.rrkjnc.UPF	$2s^2 2p^2$					LDA	NC	1	1.74	1.74		1	0	887	6.71	-0.45
	2s2 2p1.5	0	$4.6{\cdot}10^{-4}$	$1.2{\cdot}10^{-3}$												
	2s1.5 2p2	$5.7{\cdot}10^{-4}$	$1.7{\cdot}10^{-3}$	$1{\cdot}10^{-3}$												
	2s1 2p2.5	$6.4{\cdot}10^{-4}$	$2.5{\cdot}10^{-3}$	$2.9{\cdot}10^{-3}$												
	2s0.5 2p3	$1.6{\cdot}10^{-4}$	$2.8{\cdot}10^{-3}$	$4.4{\cdot}10^{-3}$												
C.my.rrkjnc.UPF (3d)	$2s^2 2p^2 3d^{-2}$					LDA	NC	2	1.3	1.3	1.3	1	0,2	887	6.71	-0.45
	2s2 2p1.5	0	$4.6{\cdot}10^{-4}$	$1.2{\cdot}10^{-3}$												
	2s1.5 2p2	$5.7{\cdot}10^{-4}$	$1.7{\cdot}10^{-3}$	$1{\cdot}10^{-3}$												
	2s1 2p2.5	$6.4{\cdot}10^{-4}$	$2.5{\cdot}10^{-3}$	$2.9{\cdot}10^{-3}$												
	2s0.5 2p3	$1.6{\cdot}10^{-4}$	$2.8{\cdot}10^{-3}$	$4.4{\cdot}10^{-3}$												
	2s2 2p1.5 3d0	0	$4.6{\cdot}10^{-4}$	$1.2{\cdot}10^{-3}$	$3{\cdot}10^{-5}$											
	2s2 2p1 3d0.5	$1.5{\cdot}10^{-3}$	$5.5{\cdot}10^{-4}$	$5.6{\cdot}10^{-3}$	$3{\cdot}10^{-5}$											
	2s2 2p0.5 3d1	$6.6{\cdot}10^{-3}$	$4.7{\cdot}10^{-3}$	$1.6{\cdot}10^{-2}$	$4{\cdot}10^{-5}$											
	2s2 2p0 3d1.5	$1.9{\cdot}10^{-2}$	$1.4{\cdot}10^{-2}$	$3.4{\cdot}10^{-2}$	$2{\cdot}10^{-5}$											
	2s1.5 2p1.5 3d0.5	$6.7{\cdot}10^{-4}$	$2.4{\cdot}10^{-3}$	$1.3{\cdot}10^{-3}$	$2{\cdot}10^{-5}$											

2s1 2p1.5 3d1	$2.6{\cdot}10^{-3}$	$5.3{\cdot}10^{-3}$	$1.8{\cdot}10^{-3}$	$2{\cdot}10^{-5}$

3 valence charge state transferability test of two selected LDA pseudopotentials.

Name	Configuration	ΔE^{tot}_{ae-ps}	E^{2s}_{ae-ps}	E^{2p}_{ae-ps}	E^{3d}_{ae-ps}	XC	Method	N proj.	$r_c 2s^2$	$r_c 2p^2$	$r_c 3d^{-2}$	lloc	lnloc	grid	a^{lat}_{eq} a.u.	$\frac{th-exp}{exp}$, %
Experiment															6.74	
C-EB.pw	$2s^2 2p^2$					LDA	NC	1	1.74	1.74		1	0	851	6.71	-0.45
C.my.rrkjnc.UPF	$2s^2 2p^2$					LDA	NC	1	1.74	1.74		1	0	887	6.71	-0.45
	2s2 2p1	0	$4{\cdot}10^{-4}$	$5.4{\cdot}10^{-3}$												
	2s1.5 2p1.5	$2.2{\cdot}10^{-3}$	$2.5{\cdot}10^{-3}$	$1.1{\cdot}10^{-3}$												
	2s1 2p2	$3.6{\cdot}10^{-3}$	$4.8{\cdot}10^{-3}$	$2.7{\cdot}10^{-3}$												
	2s0.5 2p2.5	$4.2{\cdot}10^{-3}$	$6.4{\cdot}10^{-3}$	$5.6{\cdot}10^{-3}$												
C.my.rrkjnc.UPF (3d)	$2s^2 2p^2 3d^{-2}$					LDA	NC	2	1.3	1.3	1.3	1	0,2	887	6.71	-0.45
	2s2 2p1	0	$4{\cdot}10^{-4}$	$5.4{\cdot}10^{-3}$												
	2s1.5 2p1.5	$3.6{\cdot}10^{-3}$	$2.4{\cdot}10^{-3}$	$1.1{\cdot}10^{-3}$												
	2s1 2p2	$3.6{\cdot}10^{-3}$	$4.8{\cdot}10^{-3}$	$2.7{\cdot}10^{-3}$												
	2s0.5 2p2.5	$4.2{\cdot}10^{-3}$	$6.4{\cdot}10^{-3}$	$5.9{\cdot}10^{-3}$												
	2s2 2p1 3d0	0	$4{\cdot}10^{-4}$	$5.4{\cdot}10^{-3}$	$3.7{\cdot}10^{-4}$											
	2s2 2p0.5 3d0.5	$5.1{\cdot}10^{-3}$	$4.5{\cdot}10^{-3}$	$1.6{\cdot}10^{-2}$	$1.8{\cdot}10^{-4}$											
	2s2 2p0 3d1	$1.7{\cdot}10^{-2}$	$1.4{\cdot}10^{-2}$	$3.4{\cdot}10^{-2}$	$1{\cdot}10^{-4}$											
	2s1.5 2p1 3d0.5	210^{-6}	$8.7{\cdot}10^{-4}$	$8.3{\cdot}10^{-3}$	$1.7{\cdot}10^{-4}$											
	2s1 2p1 3d1	$7.7{\cdot}10^{-4}$	$2.6{\cdot}10^{-3}$	$1.3{\cdot}10^{-2}$	$2.1{\cdot}10^{-4}$											

8.2 Matrices of the 4-site model Hamiltonian

The full Hamiltonian for the NV^- 4-site model discussed in section 6.2.2 (b) of chapter 6.

$$\begin{pmatrix}
\mathrm{U}-\mathrm{V} & 0 & t_{\mathrm{CC}} & 0 & t_{\mathrm{CC}} & 0 & t_{\mathrm{CN}} & -t_{\mathrm{CC}} & 0 & -t_{\mathrm{CC}} & 0 & -t_{\mathrm{CN}} & 0 & 0 & 0 & 0 & 0 & 0 & 0 & 0 & 0 & 0 & 0 & 0 & 0 & 0 & 0 & 0 \\
0 & 0 & 0 & t_{\mathrm{CC}} & 0 & t_{\mathrm{CN}} & 0 & 0 & 0 & 0 & 0 & 0 & 0 & 0 & -t_{\mathrm{CC}} & 0 & -t_{\mathrm{CN}} & 0 & 0 & 0 & 0 & 0 & 0 & 0 & 0 & 0 & 0 & 0 \\
t_{\mathrm{CC}} & 0 & 0 & 0 & t_{\mathrm{CC}} & 0 & t_{\mathrm{CN}} & 0 & 0 & 0 & 0 & 0 & 0 & t_{\mathrm{CC}} & 0 & 0 & 0 & -t_{\mathrm{CC}} & 0 & -t_{\mathrm{CN}} & 0 & 0 & 0 & 0 & 0 & 0 & 0 & 0 \\
0 & t_{\mathrm{CC}} & 0 & 0 & 0 & t_{\mathrm{CN}} & 0 & 0 & 0 & 0 & 0 & 0 & 0 & 0 & t_{\mathrm{CC}} & 0 & 0 & 0 & 0 & 0 & 0 & 0 & -t_{\mathrm{CN}} & 0 & 0 & 0 & 0 & 0 \\
t_{\mathrm{CC}} & 0 & t_{\mathrm{CC}} & 0 & 0 & 0 & t_{\mathrm{CN}} & 0 & 0 & 0 & 0 & 0 & 0 & 0 & 0 & t_{\mathrm{CC}} & 0 & 0 & 0 & 0 & t_{\mathrm{CC}} & 0 & 0 & -t_{\mathrm{CN}} & 0 & 0 & 0 & 0 \\
0 & t_{\mathrm{CN}} & 0 & t_{\mathrm{CN}} & 0 & \varepsilon_{\mathrm{C}}-\varepsilon_{\mathrm{N}} & 0 & 0 & 0 & 0 & 0 & 0 & 0 & 0 & 0 & 0 & t_{\mathrm{CC}} & 0 & 0 & 0 & 0 & 0 & 0 & t_{\mathrm{CC}} & 0 & 0 & 0 & 0 \\
t_{\mathrm{CN}} & 0 & t_{\mathrm{CN}} & 0 & t_{\mathrm{CN}} & 0 & \varepsilon_{\mathrm{C}}-\varepsilon_{\mathrm{N}} & 0 & 0 & 0 & 0 & 0 & 0 & 0 & 0 & 0 & 0 & 0 & 0 & 0 & 0 & 0 & 0 & 0 & t_{\mathrm{CC}} & 0 & 0 & t_{\mathrm{CN}} \\
-t_{\mathrm{CC}} & 0 & 0 & 0 & 0 & 0 & 0 & 0 & 0 & t_{\mathrm{CC}} & 0 & t_{\mathrm{CN}} & 0 & -t_{\mathrm{CC}} & 0 & -t_{\mathrm{CC}} & 0 & -t_{\mathrm{CN}} & 0 & 0 & 0 & 0 & 0 & 0 & 0 & 0 & 0 & 0 \\
0 & 0 & 0 & 0 & 0 & 0 & 0 & 0 & 0 & 0 & t_{\mathrm{CC}} & 0 & t_{\mathrm{CN}} & 0 & 0 & 0 & 0 & 0 & 0 & -t_{\mathrm{CC}} & 0 & -t_{\mathrm{CN}} & 0 & 0 & 0 & 0 & 0 & 0 \\
-t_{\mathrm{CC}} & 0 & 0 & 0 & 0 & 0 & 0 & t_{\mathrm{CC}} & 0 & 0 & 0 & t_{\mathrm{CN}} & 0 & 0 & 0 & 0 & 0 & t_{\mathrm{CC}} & 0 & 0 & 0 & -t_{\mathrm{CC}} & 0 & -t_{\mathrm{CN}} & 0 & 0 & 0 & 0 \\
0 & 0 & 0 & 0 & 0 & 0 & 0 & 0 & t_{\mathrm{CC}} & 0 & 0 & 0 & t_{\mathrm{CN}} & 0 & 0 & 0 & 0 & 0 & 0 & t_{\mathrm{CC}} & 0 & 0 & 0 & 0 & 0 & -t_{\mathrm{CN}} & 0 \\
-t_{\mathrm{CN}} & 0 & 0 & 0 & 0 & 0 & 0 & t_{\mathrm{CN}} & 0 & t_{\mathrm{CN}} & 0 & \varepsilon_{\mathrm{C}}-\varepsilon_{\mathrm{N}} & 0 & 0 & 0 & 0 & 0 & 0 & 0 & 0 & t_{\mathrm{CC}} & 0 & 0 & 0 & 0 & t_{\mathrm{CC}} & 0 & -t_{\mathrm{CN}} \\
0 & 0 & 0 & 0 & 0 & 0 & 0 & 0 & t_{\mathrm{CN}} & 0 & t_{\mathrm{CN}} & 0 & \varepsilon_{\mathrm{C}}-\varepsilon_{\mathrm{N}} & 0 & 0 & 0 & 0 & 0 & 0 & 0 & 0 & t_{\mathrm{CC}} & 0 & 0 & 0 & 0 & t_{\mathrm{CC}} & 0 \\
0 & 0 & t_{\mathrm{CC}} & 0 & 0 & 0 & 0 & -t_{\mathrm{CC}} & 0 & 0 & 0 & 0 & 0 & \mathrm{U}-\mathrm{V} & 0 & t_{\mathrm{CC}} & 0 & t_{\mathrm{CN}} & -t_{\mathrm{CC}} & 0 & -t_{\mathrm{CN}} & 0 & 0 & 0 & 0 & 0 & 0 & 0 \\
0 & -t_{\mathrm{CC}} & 0 & t_{\mathrm{CC}} & 0 & 0 & 0 & 0 & 0 & 0 & 0 & 0 & 0 & 0 & 0 & 0 & t_{\mathrm{CN}} & 0 & 0 & 0 & 0 & 0 & 0 & -t_{\mathrm{CN}} & 0 & 0 & 0 & 0 \\
0 & 0 & 0 & 0 & t_{\mathrm{CC}} & 0 & 0 & -t_{\mathrm{CC}} & 0 & 0 & 0 & 0 & 0 & t_{\mathrm{CC}} & 0 & 0 & 0 & 0 & 0 & 0 & t_{\mathrm{CC}} & 0 & 0 & -t_{\mathrm{CN}} & 0 & 0 & 0 & 0 \\
0 & -t_{\mathrm{CN}} & 0 & 0 & 0 & t_{\mathrm{CC}} & 0 & 0 & 0 & 0 & 0 & 0 & 0 & 0 & t_{\mathrm{CN}} & 0 & t_{\mathrm{CN}} & 0 & \varepsilon_{\mathrm{C}}-\varepsilon_{\mathrm{N}} & 0 & 0 & 0 & 0 & t_{\mathrm{CC}} & 0 & 0 & 0 & 0 \\
0 & 0 & 0 & 0 & 0 & 0 & t_{\mathrm{CC}} & -t_{\mathrm{CN}} & 0 & 0 & 0 & 0 & t_{\mathrm{CN}} & 0 & t_{\mathrm{CN}} & 0 & \varepsilon_{\mathrm{C}}-\varepsilon_{\mathrm{N}} & 0 & 0 & 0 & 0 & 0 & 0 & t_{\mathrm{CC}} & 0 & 0 & 0 & t_{\mathrm{CN}} \\
0 & 0 & -t_{\mathrm{CC}} & 0 & 0 & 0 & 0 & 0 & t_{\mathrm{CC}} & 0 & 0 & 0 & -t_{\mathrm{CC}} & 0 & 0 & 0 & 0 & 0 & t_{\mathrm{CN}} & 0 & -t_{\mathrm{CC}} & 0 & -t_{\mathrm{CN}} & 0 & 0 & 0 & 0 \\
0 & 0 & 0 & 0 & 0 & 0 & 0 & -t_{\mathrm{CC}} & 0 & t_{\mathrm{CC}} & 0 & 0 & 0 & 0 & 0 & 0 & 0 & 0 & 0 & t_{\mathrm{CN}} & 0 & 0 & 0 & 0 & -t_{\mathrm{CN}} & 0 \\
0 & 0 & -t_{\mathrm{CN}} & 0 & 0 & 0 & 0 & 0 & 0 & t_{\mathrm{CC}} & 0 & -t_{\mathrm{CN}} & 0 & 0 & 0 & 0 & 0 & t_{\mathrm{CN}} & 0 & \varepsilon_{\mathrm{C}}-\varepsilon_{\mathrm{N}} & 0 & 0 & 0 & 0 & t_{\mathrm{CC}} & 0 & -t_{\mathrm{CN}} \\
0 & 0 & 0 & 0 & 0 & 0 & 0 & 0 & -t_{\mathrm{CN}} & 0 & 0 & 0 & t_{\mathrm{CC}} & 0 & 0 & 0 & 0 & 0 & 0 & 0 & t_{\mathrm{CN}} & 0 & \varepsilon_{\mathrm{C}}-\varepsilon_{\mathrm{N}} & 0 & 0 & t_{\mathrm{CC}} & 0 \\
0 & 0 & 0 & -t_{\mathrm{CN}} & 0 & t_{\mathrm{CC}} & 0 & 0 & 0 & 0 & 0 & 0 & 0 & 0 & -t_{\mathrm{CN}} & 0 & t_{\mathrm{CC}} & 0 & 0 & 0 & 0 & \varepsilon_{\mathrm{C}}-\varepsilon_{\mathrm{N}} & 0 & 0 & 0 & 0 & t_{\mathrm{CN}} \\
0 & 0 & 0 & 0 & -t_{\mathrm{CN}} & 0 & 0 & 0 & 0 & 0 & t_{\mathrm{CC}} & 0 & 0 & 0 & -t_{\mathrm{CN}} & 0 & 0 & 0 & t_{\mathrm{CC}} & 0 & -t_{\mathrm{CN}} & 0 & 0 & \varepsilon_{\mathrm{C}}-\varepsilon_{\mathrm{N}} & 0 & 0 & -t_{\mathrm{CN}} \\
0 & 0 & 0 & 0 & 0 & 0 & 0 & 0 & 0 & -t_{\mathrm{CN}} & 0 & t_{\mathrm{CC}} & 0 & 0 & 0 & 0 & 0 & 0 & -t_{\mathrm{CN}} & 0 & t_{\mathrm{CC}} & 0 & 0 & 0 & \varepsilon_{\mathrm{C}}-\varepsilon_{\mathrm{N}} & 0 & 0 \\
0 & 0 & 0 & 0 & 0 & 0 & t_{\mathrm{CN}} & 0 & 0 & 0 & 0 & -t_{\mathrm{CN}} & 0 & 0 & 0 & 0 & 0 & t_{\mathrm{CN}} & 0 & 0 & -t_{\mathrm{CN}} & 0 & 0 & 0 & t_{\mathrm{CN}} & -t_{\mathrm{CN}} & 0 & 2\varepsilon_{\mathrm{C}}-\varepsilon_{\mathrm{N}}+\mathrm{U}-\mathrm{V}
\end{pmatrix} \tag{8.1}$$

The full permuted Hamiltonian of the 4-site model discussed in section 6.2.2 (b) of chapter 6.

$$\begin{pmatrix}
2\varepsilon_{\mathrm{C}}-\varepsilon_{\mathrm{N}}+\mathrm{U}-\mathrm{V} & t_{\mathrm{CN}} & -t_{\mathrm{CN}} & 0 & -t_{\mathrm{CN}} & 0 & t_{\mathrm{CN}} & 0 & 0 & -t_{\mathrm{CN}} & 0 & t_{\mathrm{CN}} & 0 & 0 & 0 & 0 & 0 & 0 & 0 & 0 & 0 & 0 & 0 & 0 & 0 & 0 & 0 & 0 \\
t_{\mathrm{CN}} & \varepsilon_{\mathrm{C}}-\varepsilon_{\mathrm{N}} & 0 & t_{\mathrm{CN}} & 0 & -t_{\mathrm{CN}} & t_{\mathrm{CC}} & 0 & 0 & 0 & -t_{\mathrm{CN}} & t_{\mathrm{CC}} & 0 & 0 & 0 & 0 & 0 & 0 & 0 & 0 & 0 & 0 & 0 & 0 & 0 & 0 & 0 & 0 \\
-t_{\mathrm{CN}} & 0 & \varepsilon_{\mathrm{C}}-\varepsilon_{\mathrm{N}} & -t_{\mathrm{CN}} & t_{\mathrm{CC}} & 0 & 0 & -t_{\mathrm{CN}} & 0 & t_{\mathrm{CC}} & 0 & 0 & -t_{\mathrm{CN}} & 0 & 0 & 0 & 0 & 0 & 0 & 0 & 0 & 0 & 0 & 0 & 0 & 0 & 0 & 0 \\
0 & t_{\mathrm{CN}} & -t_{\mathrm{CN}} & \mathrm{U}-\mathrm{V} & 0 & -t_{\mathrm{CC}} & 0 & t_{\mathrm{CC}} & 0 & 0 & -t_{\mathrm{CC}} & 0 & t_{\mathrm{CC}} & 0 & 0 & 0 & 0 & 0 & 0 & 0 & 0 & 0 & 0 & 0 & 0 & 0 & 0 & 0 \\
-t_{\mathrm{CN}} & 0 & t_{\mathrm{CC}} & 0 & \varepsilon_{\mathrm{C}}-\varepsilon_{\mathrm{N}} & t_{\mathrm{CN}} & 0 & 0 & -t_{\mathrm{CN}} & t_{\mathrm{CC}} & 0 & 0 & t_{\mathrm{CN}} & 0 & 0 & 0 & 0 & 0 & 0 & 0 & 0 & 0 & 0 & 0 & 0 & 0 & 0 & 0 \\
0 & -t_{\mathrm{CN}} & 0 & -t_{\mathrm{CC}} & t_{\mathrm{CN}} & 0 & 0 & 0 & -t_{\mathrm{CC}} & 0 & t_{\mathrm{CC}} & 0 & 0 & t_{\mathrm{CC}} & 0 & 0 & 0 & 0 & 0 & 0 & 0 & 0 & 0 & 0 & 0 & 0 & 0 & 0 \\
t_{\mathrm{CN}} & t_{\mathrm{CC}} & 0 & 0 & 0 & \varepsilon_{\mathrm{C}}-\varepsilon_{\mathrm{N}} & t_{\mathrm{CN}} & t_{\mathrm{CN}} & 0 & 0 & t_{\mathrm{CC}} & 0 & 0 & t_{\mathrm{CN}} & 0 & 0 & 0 & 0 & 0 & 0 & 0 & 0 & 0 & 0 & 0 & 0 & 0 & 0 \\
0 & 0 & -t_{\mathrm{CN}} & t_{\mathrm{CC}} & 0 & 0 & t_{\mathrm{CN}} & 0 & t_{\mathrm{CC}} & 0 & 0 & 0 & t_{\mathrm{CC}} & 0 & t_{\mathrm{CC}} & 0 & 0 & 0 & 0 & 0 & 0 & 0 & 0 & 0 & 0 & 0 & 0 & 0 \\
0 & 0 & 0 & 0 & -t_{\mathrm{CN}} & -t_{\mathrm{CC}} & t_{\mathrm{CN}} & t_{\mathrm{CC}} & \mathrm{U}-\mathrm{V} & 0 & 0 & 0 & 0 & -t_{\mathrm{CC}} & t_{\mathrm{CC}} & 0 & 0 & 0 & 0 & 0 & 0 & 0 & 0 & 0 & 0 & 0 & 0 & 0 \\
-t_{\mathrm{CN}} & 0 & t_{\mathrm{CC}} & 0 & t_{\mathrm{CC}} & 0 & 0 & 0 & 0 & \varepsilon_{\mathrm{C}}-\varepsilon_{\mathrm{N}} & t_{\mathrm{CN}} & 0 & 0 & 0 & -t_{\mathrm{CN}} & -t_{\mathrm{CN}} & 0 & 0 & 0 & 0 & 0 & 0 & 0 & 0 & 0 & 0 & 0 & 0 \\
0 & -t_{\mathrm{CN}} & 0 & -t_{\mathrm{CC}} & 0 & t_{\mathrm{CC}} & 0 & 0 & 0 & t_{\mathrm{CN}} & 0 & 0 & 0 & -t_{\mathrm{CC}} & -t_{\mathrm{CC}} & 0 & 0 & 0 & 0 & 0 & 0 & 0 & 0 & 0 & 0 & 0 & 0 & 0 \\
t_{\mathrm{CN}} & t_{\mathrm{CC}} & 0 & 0 & 0 & 0 & t_{\mathrm{CC}} & 0 & 0 & 0 & 0 & \varepsilon_{\mathrm{C}}-\varepsilon_{\mathrm{N}} & t_{\mathrm{CN}} & -t_{\mathrm{CN}} & 0 & t_{\mathrm{CN}} & 0 & 0 & 0 & 0 & 0 & 0 & 0 & 0 & 0 & 0 & 0 & 0 & 0 \\
0 & 0 & -t_{\mathrm{CN}} & t_{\mathrm{CC}} & 0 & 0 & 0 & t_{\mathrm{CC}} & 0 & 0 & 0 & t_{\mathrm{CN}} & 0 & -t_{\mathrm{CC}} & 0 & t_{\mathrm{CC}} & 0 & 0 & 0 & 0 & 0 & 0 & 0 & 0 & 0 & 0 & 0 & 0 \\
0 & 0 & 0 & t_{\mathrm{CN}} & t_{\mathrm{CN}} & t_{\mathrm{CC}} & 0 & 0 & -t_{\mathrm{CC}} & 0 & 0 & -t_{\mathrm{CN}} & -t_{\mathrm{CN}} & 0 & 0 & -t_{\mathrm{CC}} & 0 & 0 & 0 & 0 & 0 & 0 & 0 & 0 & 0 & 0 & 0 & 0 \\
0 & 0 & 0 & 0 & 0 & 0 & t_{\mathrm{CN}} & t_{\mathrm{CC}} & t_{\mathrm{CC}} & -t_{\mathrm{CN}} & -t_{\mathrm{CC}} & 0 & 0 & 0 & 0 & t_{\mathrm{CC}} & 0 & 0 & 0 & 0 & 0 & 0 & 0 & 0 & 0 & 0 & 0 & 0 \\
0 & 0 & 0 & 0 & 0 & 0 & 0 & 0 & 0 & -t_{\mathrm{CN}} & -t_{\mathrm{CC}} & t_{\mathrm{CN}} & t_{\mathrm{CC}} & -t_{\mathrm{CC}} & t_{\mathrm{CC}} & \mathrm{U}-\mathrm{V} & 0 & 0 & 0 & 0 & 0 & 0 & 0 & 0 & 0 & 0 & 0 & 0 \\
0 & 0 & 0 & 0 & 0 & 0 & 0 & 0 & 0 & 0 & 0 & 0 & 0 & 0 & 0 & 0 & -t_{\mathrm{CN}} & -t_{\mathrm{CC}} & t_{\mathrm{CN}} & t_{\mathrm{CC}} & 0 & 0 & 0 & 0 & 0 & 0 & 0 \\
0 & 0 & 0 & 0 & 0 & 0 & 0 & 0 & 0 & 0 & 0 & 0 & 0 & 0 & 0 & 0 & -t_{\mathrm{CN}} & \varepsilon_{\mathrm{C}}-\varepsilon_{\mathrm{N}} & t_{\mathrm{CN}} & t_{\mathrm{CC}} & 0 & t_{\mathrm{CC}} & 0 & 0 & 0 & 0 & 0 \\
0 & 0 & 0 & 0 & 0 & 0 & 0 & 0 & 0 & 0 & 0 & 0 & 0 & 0 & 0 & 0 & -t_{\mathrm{CC}} & t_{\mathrm{CN}} & 0 & 0 & t_{\mathrm{CC}} & -t_{\mathrm{CN}} & 0 & 0 & 0 & 0 & 0 \\
0 & 0 & 0 & 0 & 0 & 0 & 0 & 0 & 0 & 0 & 0 & 0 & 0 & 0 & 0 & 0 & t_{\mathrm{CN}} & t_{\mathrm{CC}} & 0 & \varepsilon_{\mathrm{C}}-\varepsilon_{\mathrm{N}} & t_{\mathrm{CN}} & t_{\mathrm{CC}} & 0 & 0 & 0 & 0 & 0 \\
0 & 0 & 0 & 0 & 0 & 0 & 0 & 0 & 0 & 0 & 0 & 0 & 0 & 0 & 0 & 0 & t_{\mathrm{CC}} & 0 & t_{\mathrm{CC}} & t_{\mathrm{CN}} & 0 & -t_{\mathrm{CN}} & 0 & 0 & 0 & 0 & 0 \\
0 & 0 & 0 & 0 & 0 & 0 & 0 & 0 & 0 & 0 & 0 & 0 & 0 & 0 & 0 & 0 & 0 & -t_{\mathrm{CN}} & -t_{\mathrm{CC}} & t_{\mathrm{CN}} & t_{\mathrm{CC}} & 0 & -t_{\mathrm{CN}} & \varepsilon_{\mathrm{C}}-\varepsilon_{\mathrm{N}} & 0 & 0 & 0 \\
0 & 0 & 0 & 0 & 0 & 0 & 0 & 0 & 0 & 0 & 0 & 0 & 0 & 0 & 0 & 0 & 0 & t_{\mathrm{CC}} & -t_{\mathrm{CN}} & t_{\mathrm{CC}} & -t_{\mathrm{CN}} & \varepsilon_{\mathrm{C}}-\varepsilon_{\mathrm{N}} & 0 & 0 & 0 & 0 & 0
\end{pmatrix} \tag{8.2}$$

Bibliography

[1] C. Kurtsiefer, S. Mayer, P. Zarda, and H. Weinfurter, "Stable solid-state source of single photons," Phys. Rev. Lett., vol. 85, 2000. 1

[2] A. Beveratos, R. Brouri, T. Gacoin, A. Villing, J. P. Poizat, and P. Grangier, "Single Photon Quantum Cryptography," Phys. Rev. Lett., vol. 89, 2002. 1

[3] F. Jelezko, T. Gaebel, I. Popa, M. Domhan, A. Gruber, and J. Wrachtrup, "Observation of coherent oscillation of a single nuclear spin and realization of a two-qubit conditional quantum gate," Phys. Rev. Lett., vol. 93, 2004. 1

[4] A. P. Nizovtsev, S. Y. Kilin, F. Jelezko, T. Gaebal, I. Popa, A. Gruber, , , and J. Wrachtrup, "A Quantum Computer Based on NV Centers in Diamond: Optically Detected Nutations of Single Electron and Nuclear Spins," Opt. Spectrosc., vol. 99, 2005. 1, 12

[5] M. V. G. Dutt, L. Childress, L. Jiang, E. Togan, J. Maze, F. Jelezko, A. S. Zibrov, P. R. Hemmer, and M. D. Lukin, "Quantum Register Based on," Science, vol. 316, 2007. 1

[6] L. Gordon, J. R. Weber, J. B. Varley, A. Janotti, D. D. Awschalom, and C. G. Van De Walle, "Quantum computing with defects," MRS Bull., vol. 38, 2013. 1, 39, 40, 44

[7] L. Childress and R. Hanson, "Diamond NV centers for quantum computing and quantum networks," MRS Bull., vol. 38, 2013. 1

[8] C. L. Degen, "Scanning magnetic field microscope with a diamond single-spin sensor," Appl. Phys. Lett., vol. 92, 2008. 1

[9] J. M. Taylor, P. Cappellaro, L. Childress, L. Jiang, D. Budker, P. R. Hemmer, A. Yacoby, R. Walsworth, and M. D. Lukin, "High-sensitivity diamond magnetometer with nanoscale resolution," Nat. Phys., vol. 4, 2008. 1

[10] J. R. Maze, P. L. Stanwix, J. S. Hodges, S. Hong, J. M. Taylor, P. Cappellaro, L. Jiang, M. V. Dutt, E. Togan, A. S. Zibrov, A. Yacoby, R. L. Walsworth, and M. D. Lukin, "Nanoscale magnetic sensing with an individual electronic spin in diamond," Nature, vol. 455, 2008. 1

[11] G. Balasubramanian, I. Y. Chan, R. Kolesov, M. Al-Hmoud, J. Tisler, C. Shin, C. Kim, A. Wojcik, P. R. Hemmer, A. Krueger, T. Hanke, A. Leitenstorfer, R. Bratschitsch, F. Jelezko, and J. Wrachtrup, "Nanoscale imaging magnetometry with diamond spins under ambient conditions," Nature, vol. 455, 2008. 1

[12] G. Balasubramanian, P. Neumann, D. Twitchen, M. Markham, R. Kolesov, N. Mizuochi, J. Isoya, J. Achard, J. Beck, J. Tissler, V. Jacques, P. R. Hemmer, F. Jelezko, and J. Wrachtrup, "Ultralong spin coherence time in isotopically engineered diamond," Nature Materials, vol. 8, 2009. 1, 14

[13] L. Rondin, J.-P. Tetienne, T. Hingant, J.-F. Roch, P. Maletinsky, and V. Jacques, "Magnetometry with nitrogen-vacancy defects in diamond," Rep Prog Phys., vol. 77, 2014. 1

[14] J.-P. Tetienne, T. Hingant, J.-V. Kim, L. H. Diez, J.-P. Adam, K. Garcia, J.-F. Roch, S. Rohart, A. Thiaville, D. Ravelosona, and V. Jacques, "Nanoscale imaging and control of domain-wall hopping with a nitrogen-vacancy center microscope," Science, vol. 344, 2014. 1

[15] M. A. Lesik, T. Plisson, L. Toraille, J. Renaud, F. Occelli, M. Schmidt, O. Salord, A. Delobbe, T. Debuisschert, L. Rondin, P. Loubeyre, and J.-F. Roch, "Magnetic measurements on micron-size samples under high pressure using designed nv centers," arXiv:1812.09894, 2018. 2, 17, 18, 108

[16] M. Kobayashi and Y. Nisida, "High pressure effects on photoluminescence spectra of color centers in diamond," Japanese Journal of Applied Physics, vol. 32, 1993. 2, 18, 19, 51, 52, 97, 101, 108

[17] M. W. Doherty, V. V. Struzhkin, D. A. Simpson, L. P. McGuinness, Y. Meng, A. Stacey, T. J. Karle, R. J. Hemley, N. B. Manson, L. C. L. Hollenberg, and S. Prawer, "Electronic properties and metrology applications of the diamond nv^- center under pressure," Phys. Rev. Lett., vol. 112, 2014. 2, 18, 19, 20, 49, 50, 51, 52, 97, 101, 108

[18] B. Deng, R. Q. Zhang, and X. Q. Shi, "New insight into the spin-conserving excitation of the negatively charged nitrogen-vacancy center in diamond," Scientific Reports, vol. 4, 2014. 2, 21, 49

[19] F. Jelezko and J. Wrachtrup, "Single defect centres in diamond: A review," Phys. Status Solidi Appl. Mater. Sci., vol. 203, 2006. 5, 11

[20] M. W. Doherty, N. B. Manson, P. Delaney, F. Jelezko, J. Wrachtrup, and L. C. Hollenberg, "The nitrogen-vacancy colour centre in diamond," Physics Reports, vol. 528, 2013. 5, 7, 8, 9, 25

[21] C. E. Dreyer, A. Alkauskas, J. L. Lyons, A. Janotti, and C. G. V. D. Walle, "First-Principles Calculations of Point Defects for Quantum Technologies," Annu. Rev. of Materials Res., vol. 48, 2018. 5, 10, 11, 34

[22] A. Gali, "Ab initio theory of nitrogen-vacancy center in diamond," arXiv:1906.00047, 2019. 5, 6, 7, 26

[23] R. Robertson, J. J. Fox, and A. E. Martin, "Two types of diamond," R. Soc. London, vol. 232, 1934. 5

[24] W. Kaiser and W. L. Bond, "Nitrogen, a major impurity in common type I diamond," Phys. Rev., vol. 115, 1959. 5

[25] L. Du Preez, "Electron paramagnetic resonance and optical invesitgations of defect centres in diamond," PhD Thesis, Univ. Witwatersrand, 1965. 5, 10

[26] A. Gruber, A. Dräbenstedt, C. Tietz, L. Fleury, J. Wrachtrup, and C. v. Borczyskowski, "Scanning confocal optical microscopy and magnetic resonance on single defect centers," Science, vol. 276, 1997. 5, 12

[27] C. A. Norris and C. D. Clark, "Photoluminescence associated with the 1.673, 1.944 and 2.498 eV centres in diamond," J. Phys. C: Solid State Phys., vol. 4, 1971. 5, 37

[28] G. Davies, M. F. Hamer, and W. C. Price, "Optical studies of the 1.945 ev vibronic band in diamond," Proc. R. Soc. Lond. A., vol. 348, 1976. 5, 10, 22, 24, 25, 37, 40, 41, 68

[29] J. A. V. Wyk and Loubser, "Carbon-12 hyperfine interaction of the unique carbon of the P_2 (ESR) or N_3 (optical) centre in diamond," J. Phys. C Solid State Phys., vol. 15, 1982. 5, 8, 82, 83

[30] A. Gali, E. Janzén, P. Deák, G. Kresse, and E. Kaxiras, "Theory of Spin-Conserving Excitation of the NV^- center in Diamond," Phys. Rev. Lett., vol. 103, 2009. 6, 47

[31] A. Drabenstedt, L. Fleury, C. Tietz, F. Jelezko, S. Kilin, A. Nizovtzev, and J. Wrachtrup, "Low-temperature microscopy and spectroscopy on single defect centers in diamond," Phys. Rev. B, vol. 60, 1999. 7

[32] A. Beveratos, R. Brouri, J.-P. Poizat, and P. Grangier, "Bunching and Antibunching from Single NV Color Centers in Diamond," Quantum Commun. Comput. Meas. 3, 2000. 7

[33] L. J. Rogers, M. W. Doherty, M. S. Barson, S. Onoda, T. Ohshima, and N. B. Manson, "Singlet levels of the NV- centre in diamond," New J. Phys., vol. 17, 2015. 7, 9, 22, 29, 90, 101, 102

[34] S. Choi, M. Jain, and S. G. Louie, "Mechanism for optical initialization of spin in NV center in diamond," Phys. Rev. B, vol. 86, p. 041202, 2012. 7, 33, 41, 44, 54, 56, 69, 70, 71, 75, 89, 108

[35] M. Bockstedte, F. Schütz, T. Garratt, V. Ivády, and A. Gali, "Ab initio description of highly correlated states in defects for realizing quantum bits," npj Quantum Materials, vol. 3, p. 31, 2018. 7, 30, 31, 41, 44, 69, 70, 73

[36] A. Batalov, V. Jacques, F. Kaiser, P. Siyushev, P. Neumann, L. J. Rogers, R. L. McMurtrie, N. B. Manson, F. Jelezko, and J. Wrachtrup, "Low temperature studies of the excited-state structure of negatively charged nitrogen-vacancy color centers in diamond," Phys. Rev. Lett., vol. 102, 2009. 8, 9, 12, 22

[37] L. J. Rogers, R. L. McMurtrie, M. J. Sellars, and N. B. Manson, "Time-averaging within the excited state of the nitrogen-vacancy centre in diamond," New J. Phys., vol. 11, 2009. 9, 10

[38] R. J. Epstein, F. M. Mendoza, Y. K. Kato, and D. D. Awschalom, "Anisotropic interactions of a single spin and dark-spin spectroscopy in diamond," Nat. Phys., vol. 1, 2005. 9

[39] G. D. Fuchs, V. V. Dobrovitski, R. Hanson, A. Batra, C. D. Weis, T. Schenkel, and D. D. Awschalom, "Excited-state spectroscopy using single Spin manipulation in diamond," Phys. Rev. Lett., vol. 101, 2008. 9

[40] P. Neumann, R. Kolesov, V. Jacques, J. Beck, J. Tisler, A. Batalov, L. Rogers, N. B. Manson, G. Balasubramanian, F. Jelezko, and J. Wrachtrup, "Excited-state spectroscopy of single NV defects in diamond using optically detected magnetic resonance," New J. Phys., vol. 11, 2009. 9, 12, 13

[41] R. Ulbricht, S. Dong, A. Gali, S. Meng, and Z. H. Loh, "Vibrational relaxation dynamics of the nitrogen-vacancy center in diamond," Phys. Rev. B, vol. 97, 2018. 11

[42] L. J. Rogers, S. Armstrong, M. J. Sellars, and N. B. Manson, "Infrared emission of the NV centre in diamond: Zeeman and uniaxial stress studies," New J. Phys., vol. 10, 2008. 12

[43] N. B. Manson, J. P. Harrison, and M. J. Sellars, "Nitrogen-vacancy center in diamond: Model of the electronic structure and associated dynamics," Phys. Rev. B, vol. 74, 2006. 12

[44] A. P. Nizovtsev, S. Y. Kilin, I. Popa, F. Jelezko, A. Gruber, C. Tietz, and J. Wrachtrup, "Spin-selective low temperature spectroscopy on single molecules with a triplet-triplet optical transition: Application to the NV defect center in diamond," Opt. Spectrosc., vol. 94, 2003. 12

[45] M. L. Goldman, M. W. Doherty, A. Sipahigil, N. Y. Yao, S. D. Bennett, N. B. Manson, A. Kubanek, and M. D. Lukin, "State-selective intersystem crossing in nitrogen-vacancy centers," Phys. Rev. B, vol. 91, 2015. 12

[46] R. Ulbricht and Z. H. Loh, "Excited-state lifetime of the N V- infrared transition in diamond," Phys. Rev. B, vol. 98, 2018. 13

[47] L. Robledo, H. Bernien, T. V. D. Sar, and R. Hanson, "Spin dynamics in the optical cycle of single nitrogen-vacancy centres in diamond," New J. Phys., vol. 13, 2011. 13

[48] G. Thiering and A. Gali, "Theory of the optical spin-polarization loop of the nitrogen-vacancy center in diamond," Phys. Rev. B, vol. 98, 2018. 13

[49] X.-F. He, N. B. Manson, and P. T. H. Fisk, "Paramagnetic resonance of photoexcited N-V defects in diamond. II. Hyperfine interaction with ^{1}4N nucleus," Phys. Rev. B, vol. 47, 1993. 13, 56

[50] J. P. Tetienne, L. Rondin, P. Spinicelli, M. Chipaux, T. Debuisschert, J. F. Roch, and V. Jacques, "Magnetic-field-dependent photodynamics of single NV defects in diamond: An application to qualitative all-optical magnetic imaging," New J. Phys., vol. 14, 2012. 14

[51] A. P. Drozdov, M. I. Eremets, I. A. Troyan, V. Ksenofontov, and S. I. Shylin, "Conventional superconductivity at 203 kelvin at high pressures in the sulfur hydride system," Nature, vol. 525, 2015. 15

[52] P. L. Alireza, , , and G. George Lonzarich, "Miniature ceramic-anvil high-pressure cell for magnetic measurements in a commercial superconducting quantum interference device magnetometer," Rev. Sci. Instrum., vol. 80, p. 023906, 2009. 15, 16

[53] R. Torchio, Y. O. Kvashnin, S. Pascarelli, O. Mathon, C. Marini, L. Genovese, P. Bruno, G. Garbarino, A. Dewaele, F. Occelli, and P. Loubeyre, "X-ray magnetic circular dichroism measurements in Ni up to 200 GPa: Resistant ferromagnetism," Phys. Rev. Lett., vol. 107, 2011. 15, 16

[54] O. Mathon, F. Baudelet, J. P. Itié, S. Pasternak, A. Pollan, and S. Pascarelli, "XMCD under pressure at the Fe K edge on the energy-dispersive beamline of the ESRF," J. Synchrotron Radiat., vol. 11, 2004. 15, 16, 17

[55] J. P. Rueff and A. Shukla, "Inelastic x-ray scattering by electronic excitations under high pressure," Rev. Mod. Phys., vol. 82, 2010. 15

[56] I. L. Spain and D. J. Dunstan, "The technology of diamond anvil high-pressure cells: II. Operation and use," J. Phys. E., vol. 22, 1989. 16

[57] A. Marizy, B. Guigue, F. Occelli, B. Leridon, and P. Loubeyre, "A symmetric miniature diamond anvil cell for magnetic measurements on dense hydrides in a SQUID magnetometer," High Press. Res., vol. 37, 2017. 16

[58] P. J. Stephens, "Magnetic Circular Dichroism," Annu. Rev. Phys. Chem., vol. 2, 1974. 16

[59] I. Board and H. Member, In memoriam Rudolf L. Mößbauer, vol. 204. Springer Science+Business Media B.V. 2012, 2012. 16

[60] I. Troyan, A. Gavriliuk, R. Rüffer, A. Chumakov, A. Mironovich, I. Lyubutin, D. Perekalin, A. P. Drozdov, and M. I. Eremets, "Resonant Scattering," vol. 351, 2016. 17

[61] M. Lesik, P. Spinicelli, S. Pezzagna, P. Happel, V. Jacques, O. Salord, B. Rasser, A. Delobbe, P. Sudraud, A. Tallaire, J. Meijer, and J. F. Roch, "Maskless and targeted creation of arrays of colour centres in diamond using focused ion beam technology," Phys. Status Solidi Appl. Mater. Sci., vol. 210, 2013. 17

[62] S. Lyapin, I. Ilichev, A. Novikov, V. Davydov, and V. Agafonov, "Study of optical properties of the NV and SiV centres in diamond at high pressures," Nanosyst. Physics, Chem. Math., 2018. 18, 19, 28

[63] S. Hsieh, P. Bhattacharyya, C. Zu, T. Mittiga, T. J. Smart, F. Machado, B. Kobrin, N. Z. Rui, M. Kamrani, S. Chatterjee, S. Choi, M. Zaletel, V. V. Struzhkin, J. E. Moore, V. I. Levitas, R. Jeanloz, and N. Y. Yao, "Imaging stress and magnetism at high pressures using a nanoscale quantum sensor," arXiv:1812.08796 [cond-mat.mes-hall], 2018. 18, 108

[64] S. Klotz, J. C. Chervin, P. Munsch, and G. Le Marchand, "Hydrostatic limits of 11 pressure transmitting media," J. Phys. D. Appl. Phys., vol. 42, 2009. 19

[65] G. J. Piermarini, "High Pressure X-Ray Crystallography With the Diamond Cell at NIST/NBS," J. Res. Natl. Inst. Stand. Technol., vol. 106, 2001. 19

[66] Z. Mi, S. R. Shieh, and High Pressure Mineral Physics Group, "High Pressure Strength Study on NaCl," AGU Fall Meeting Abstracts, 2010. 20

[67] S. Lyapin, A. Razgulov, A. Novikov, E. Ekimov, and M. Kondrin, "High pressure photoluminescence studies of diamond with GeV centers," Nanosyst. Physics, Chem. Math., vol. 9, 2018. 21, 28, 97, 101, 108

[68] G. E. Pikus and G. I. Bir, Symmetry and Strain Induced Effects in Semiconductors. New York: Wiley, 1974. 21

[69] M. Cardona and M. L. Thewalt, "Isotope effects on the optical spectra of semiconductors," Rev. Mod. Phys., vol. 77, 2005. 21

[70] V. A. Karasyuk, A. G. Steele, A. M. E. C., Lightowlers, , , and G. Davies, "to boron in silicon under uniaxial stress," vol. 45, 1992. 22

[71] G. Davies, "Dynamic Jahn-Teller distortion at trigonal optical centres in diamond," J. Phys. C Solid State Phys., vol. 12, 1979. 22, 25, 29

[72] Y. Mita, "Change of absorption spectra in type-Ib diamond with heavy neutron irradiation," Phys. Rev. B, vol. 53, 1996. 24

[73] S. Felton, A. M. Edmonds, and M. E. Newton, "Electron paramagnetic resonance studies of the neutral nitrogen vacancy in diamond," Phys. Rev. B, vol. 77, 2008. 25

[74] A. Gali, "Theory of the neutral nitrogen-vacancy center in diamond and its application to the realization of a qubit Adam," Phys. Rev. B, vol. 79, 2009. 25, 42, 44, 92, 94

[75] A. Ranjbar, M. Babamoradi, M. H. Saani, M. A. Vesaghi, K. Esfarjani, and Y. Kawazoe, "Many-electron states of nitrogen-vacancy centers in diamond and spin density calculations," Phys. Rev. B, vol. 84, 2011. 25, 38, 40, 42, 43, 44, 54, 56, 72, 75, 82, 83, 89, 93, 94, 95

[76] N. B. Manson, K. Beha, A. Batalov, L. J. Rogers, M. W. Doherty, R. Bratschitsch, and A. Leitenstorfer, "Assignment of the NV^0 575-nm zero-phonon line in diamond to a $^2E - ^2A_2$ transition," Phys. Rev. B, vol. 87, 2013. 25, 27, 29, 42, 43, 94

[77] N. B. Manson and J. P. Harrison, "Photo-ionization of the nitrogen-vacancy center in diamond," Diam. Relat. Mater., vol. 14, 2005. 26

[78] N. Aslam, G. Waldherr, P. Neumann, F. Jelezko, and J. Wrachtrup, "Photo-induced ionization dynamics of the nitrogen vacancy defect in diamond investigated by single-shot charge state detection," New J. Phys., vol. 15, 2013. 26

[79] P. Siyushev, H. Pinto, M. Vörös, A. Gali, F. Jelezko, and J. Wrachtrup, "Optically controlled switching of the charge state of a single nitrogen-vacancy center in diamond at cryogenic temperatures," Phys. Rev. Lett., vol. 110, 2013. 26

[80] P. Siyushev, M. Nesladek, E. Bourgeois, M. Gulka, J. Hruby, T. Yamamoto, M. Trupke, T. Teraji, J. Isoya, and F. Jelezko, "Photoelectrical imaging and coherent spin-state readout of single nitrogen-vacancy centers in diamond," Science (80-.)., vol. 363, 2019. 26

[81] M. Barson, E. Krausz, N. B. Manson, and M. W. Doherty, "The fine structure of the neutral nitrogen-vacancy center in diamond," arXiv:1905.09037v1, 2019. 26, 27, 28

[82] R. M. Martin, L. Reining, and D. M. Ceperley, Interacting Electrons: Theory and Computational Approaches. Cambridge University Press, 2016. 30, 31

[83] D. K. W. Mok, R. Neumann, and N. C. Handy, "Dynamical and nondynamical correlation," J. Phys. Chem., vol. 100, 1996. 30

[84] O. Sinanoğlu Adv. Chem. Phys., vol. 6, 1964. 30

[85] J. Kong and E. Proynov, "Density functional model for nondynamic and strong correlation," Journal of Chemical Theory and Computation, vol. 12, 2016. 30

[86] E. Ramos-Cordoba, P. Salvador, and E. Matito, "Separation of dynamic and nondynamic correlation," Phys. Chem. Chem. Phys., vol. 18, 2016. 30, 31

[87] M. Casula, "Resonating valence bond ansatz for real materials : from electronic structure to molecular dynamics of correlated compounds," HDR thesis, 2017. 31

[88] D. Zgid, E. Gull, and G. K. L. Chan, "Truncated configuration interaction expansions as solvers for correlated quantum impurity models and dynamical mean-field theory," Phys. Rev. B, vol. 86, 2012. 31

[89] F. Aryasetiawan, M. Imada, A. Georges, G. Kotliar, S. Biermann, and A. I. Lichtenstein, "Frequency-dependent local interactions and low-energy effective models from electronic structure calculations," Phys. Rev. B, vol. 70, 2004. 31

[90] A. J. Garza, C. A. Jiménez-Hoyos, and G. E. Scuseria, "Capturing static and dynamic correlations by a combination of projected Hartree-Fock and density functional theories," J. Chem. Phys., vol. 138, 2013. 31

[91] D. Cremer, "Density functional theory: coverage of dynamic and non-dynamic electron correlation effects," Molecular Physics, vol. 99, 2001. 32, 34

[92] F. Bechstedt, Many-Body Approach to Electronic Excitations: Concepts and Applications. Springer-Verlag Berlin Heidelberg, 2014. 32, 33, 70

[93] D. A. Liberman, "Slater transition-state band-structure calculations," Phys. Rev. B, vol. 62, 2000. 32

[94] R. W. Godby, M. Schluter., and L. J. Sham, "Nene," Phys. Rev. B, vol. 37, 1998. 32

[95] P. Mori-Sánchez, A. J. Cohen, and W. Yang, "Localization and delocalization errors in density functional theory and implications for band-gap prediction," Phys. Rev. Lett., vol. 100, 2008. 32, 35

[96] V. I. Anisimov, J. Zaanen, and O. K. Andersen, "Band theory and Mott insulators: Hubbard U instead of Stoner I," Phys. Rev. B, vol. 44, 1991. 32

[97] V. I. Anisimov, I. V. Solovyev, M. A. Korotin, M. T. Czyyk, and G. A. Sawatzky, "Density-functional theory and NiO photoemission spectra," Phys. Rev. B, vol. 48, 1993. 32

[98] I. Solovyev, H. Dederichs, and V. Anisimov, "Corrected atomic limit in the local-density approximation and the electronic structure of d impurities in Rb," Phys. Rev. B, vol. 50, 1994. 32

[99] A. Lichtenstein and M. Katsnelson, "Ab initio calculations of quasiparticle band structure in correlated systems: LDA++ approach," Phys. Rev. B, vol. 57, 1998. 32

[100] J. Hubbard, "Electron correlations in narrow energy bands - IV. The atomic representation," Proc. R. Soc. London. A., vol. 285, 1964. 32, 34, 54

[101] M. Cococcioni and S. De Gironcoli, "Linear response approach to the calculation of the effective interaction parameters in the LDA+U method," Phys. Rev. B, vol. 71, 2005. 32

[102] V. Leiria Campo and M. Cococcioni, "Extended DFT + U + V method with on-site and inter-site electronic interactions," J. Phys. Condens. Matter, vol. 22, 2010. 32

[103] I. Timrov, N. Marzari, and M. Cococcioni, "Hubbard parameters from density-functional perturbation theory," Phys. Rev. B, vol. 98, 2018. 32

[104] S. Koizumi, "Chapter 5 N-type diamond growth," Semicond. Semimetals, vol. 76, 2003. 33

[105] C. Freysoldt, B. Grabowski, T. Hickel, J. Neugebauer, G. Kresse, A. Janotti, and C. G. Van De Walle, "First-principles calculations for point defects in solids," Rev. Mod. Phys., vol. 86, 2014. 33, 34, 48

[106] J. Heyd, G. E. Scuseria, and M. Ernzerhof, "Hybrid functionals based on a screened Coulomb potential," J. Chem. Phys., vol. 118, 2003. 33, 37, 50

[107] J. Heyd, G. E. Scuseria, and M. Ernzerhof, "Erratum: Hybrid functionals based on a screened Coulomb potential (Journal of Chemical Physics (2003) 118 (8207))," J. Chem. Phys., vol. 124, 2006. 33, 37, 50

[108] L. Hedin, "New method for calculating the one-particle green's function with application to the electron-gas problem," Phys. Rev., vol. 139, 1965. 33

[109] Viktor Ivady, Igor A. Abrikosov and A. Gali, "Scientific Highlight Of The Month," Psik Sci. Highlight Mon., vol. 141, 2018. 34

[110] J. P. Perdew and M. Levy, "Extrema of the density functional for the energy: Excited states from the ground-state theory," Phys. Rev. B, vol. 31, 1985. 35

[111] C. Li, J. Lu, and W. Yang, "Gentlest ascent dynamics for calculating first excited state and exploring energy landscape of Kohn-Sham density functionals," J. Chem. Phys., vol. 143, 2015. 35

[112] T. Ziegler and A. Rank, "On the Calculation of Multiplet Energies by the Hartree-Fock-Slater Method," Theor. China. Acta, vol. 43, 1977. 35, 36

[113] U. von Barth, "Local-density theory of multiplet structure," Phys. Rev. A, vol. 20, 1979. 35, 36

[114] A. J. Cohen, P. Mori-Sánchez, and W. Yang, "Fractional charge perspective on the band gap in density-functional theory," Phys. Rev. B, vol. 77, 2008. 35

[115] M. M. Rieger and P. Vogl, "Relativistic self-interaction-free density-functional formalism," Phys. Rev. A, vol. 52, 1995. 35

[116] T. A. Pham, H. V. Nguyen, D. Rocca, and G. Galli, "GW calculations using the spectral decomposition of the dielectric matrix: Verification, validation, and comparison of methods," Phys. Rev. B, vol. 87, 2013. 35

[117] M. K. Chan and G. Ceder, "Efficient band gap prediction for solids," Phys. Rev. Lett., vol. 105, 2010. 36

[118] A. Gali, M. Fyta, and E. Kaxiras, "Ab initio supercell calculations on nitrogen-vacancy center in diamond: Electronic structure and hyperfine tensors," Phys. Rev. B, vol. 77, 2008. 36, 37, 39, 44, 56, 108

[119] A. Gali, E. Janzén, P. Deák, G. Kresse, and E. Kaxiras, "Theory of spin-conserving excitation of the $n - V^-$ center in diamond," Phys. Rev. Lett., vol. 103, 2009. 37, 40, 44, 49, 50

[120] P. Deák, B. Aradi, T. Frauenheim, E. Janzén, and A. Gali, "Accurate defect levels obtained from the HSE06 range-separated hybrid functional," Phys. Rev. B, vol. 81, 2010. 37

[121] A. Alkauskas, C. E. Dreyer, J. L. Lyons, and C. G. Van de Walle, "Role of excited states in shockley-read-hall recombination in wide-band-gap semiconductors," Phys. Rev. B, vol. 93, 2016. 37

[122] M. Tinkham and A. A. Cottey, Group Theory and Quantum Mechanics, vol. 26. Dover Publications, 1975. 37, 56

[123] M. S. Dresselhaus, Group Theory for solid. Springer-Verlag Berlin Heidelberg, 2002. 37, 56

[124] A. Lenef and S. C. Rand, "Electronic structure of the $N - V$ center in diamond: Theory," Phys. Rev. B, vol. 53, 1996. 37, 39, 47, 56

[125] J. P. Goss, R. Jones, S. J. Breuer, P. R. Briddon, and S. Öberg, "The twelve-line 1.682 eV luminescence center in diamond and the vacancy-silicon complex," Phys. Rev. Lett., vol. 77, 1996. 39, 40, 44

[126] J. A. Larsson and P. Delaney, "Electronic structure of the nitrogen-vacancy center in diamond from first-principles theory," Phys. Rev. B, vol. 77, 2008. 39, 44, 56

[127] Y. Ma, M. Rohlfing, and A. Gali, "Excited states of the negatively charged nitrogen-vacancy color center in diamond," Phys. Rev. B, vol. 81, 2010. 39, 44, 49, 71, 73, 90

[128] P. Delaney and J. A. Larsson, "Small cluster model of the NV centre in diamond," Phys. Procedia, vol. 3, 2010. 39, 40, 44

[129] A. Alkauskas, B. B. Buckley, D. D. Awschalom, and C. G. Van De Walle, "First-principles theory of the luminescence lineshape for the triplet transition in diamond NV centres," New J. Phys., vol. 16, 2014. 39, 40, 44

[130] U. von Barth, "Local-density theory of multiplet structure," Phys. Rev. A, vol. 20, 1979. 40

[131] V. M. Acosta, A. Jarmola, E. Bauch, and D. Budker, "Optical properties of the nitrogen-vacancy singlet levels in diamond," Phys. Rev. B, vol. 82, p. 201202, 2010. 41, 68

[132] A. S. Zyubin, A. M. Mebel, M. Hayashi, H. C. Chang, and S. H. Lin, "Quantum Chemical Modeling of Photoadsorption Properties of the Nitrogen-Vacancy Point Defect in Diamond," J Comput Chem, vol. 30, 2008. 43, 44, 93

[133] P. Giannozzi, S. Baroni, N. Bonini, M. Calandra, R. Car, C. Cavazzoni, D. Ceresoli, G. L. Chiarotti, M. Cococcioni, I. Dabo, A. Dal Corso, S. de Gironcoli, S. Fabris, G. Fratesi, R. Gebauer, U. Gerstmann, C. Gougoussis, A. Kokalj, M. Lazzeri, L. Martin-Samos, N. Marzari, F. Mauri, R. Mazzarello, S. Paolini, A. Pasquarello, L. Paulatto, C. Sbraccia, S. Scandolo, G. Sclauzero, A. P. Seitsonen, A. Smogunov, P. Umari, and R. M. Wentzcovitch, "Quantum espresso: a modular and open-source software project for quantum simulations of materials," Journal of Physics: Condensed Matter, vol. 21, no. 39, p. 395502 (19pp), 2009. 46

[134] P. Giannozzi, O. Andreussi, T. Brumme, O. Bunau, M. B. Nardelli, M. Calandra, R. Car, C. Cavazzoni, D. Ceresoli, M. Cococcioni, N. Colonna, I. Carnimeo, A. D. Corso, S. de Gironcoli, P. Delugas, R. A. D. Jr, A. Ferretti, A. Floris, G. Fratesi, G. Fugallo, R. Gebauer, U. Gerstmann, F. Giustino, T. Gorni, J. Jia, M. Kawamura, H.-Y. Ko, A. Kokalj, E. Küçükbenli, M. Lazzeri, M. Marsili, N. Marzari, F. Mauri, N. L. Nguyen, H.-V. Nguyen, A. O. de-la Roza, L. Paulatto, S. Poncé, D. Rocca, R. Sabatini, B. Santra, M. Schlipf, A. P. Seitsonen, A. Smogunov, I. Timrov, T. Thonhauser, P. Umari, N. Vast, X. Wu, and S. Baroni, "Advanced capabilities for materials modelling with quantum espresso," Journal of Physics: Condensed Matter, vol. 29, 2017. 46

[135] H. J. Monkhorst and J. D. Pack, "Special points for brillouin-zone integrations," Phys. Rev. B, vol. 13, 1976. 46

[136] D. R. Hamann, "Optimized norm-conserving vanderbilt pseudopotentials," Phys. Rev. B, vol. 88, 2013. 46

[137] A. D. Corso, "Pseudopotentials periodic table: From H to Pu," Comput. Mater. Sci., vol. 95, 2014. 46, 110

[138] D. Vanderbilt, "Soft self-consistent pseudopotentials in a generalized eigenvalue formalism," Phys. Rev. B, vol. 41, 1990. 46

[139] C. A. Ullrich and W. Kohn, "Kohn-sham theory for ground-state ensembles," Phys. Rev. Lett., vol. 87, 2001. 48

[140] G. Li Manni, R. K. Carlson, S. Luo, D. Ma, J. Olsen, D. G. Truhlar, and L. Gagliardi, "Multiconfiguration pair-density functional theory," J. Chem. Theory Comput., vol. 10, 2014. 48

[141] J.-D. Chai, "Density functional theory with fractional orbital occupations," J. Chem. Phys., vol. 136, p. 154104, 2012. 48

[142] S. Felton, A. M. Edmonds, M. E. Newton, P. M. Martineau, D. Fisher, D. J. Twitchen, and J. M. Baker, "Hyperfine interaction in the ground state of the negatively charged nitrogen vacancy center in diamond," Phys. Rev. B, vol. 79, 2009. 56, 82, 83

[143] E. Cuthill and J. McKee, "Reducing the bandwidth of sparse symmetric matrices," Proc. 1969 24th Natl. Conf. -, 1969. 59

[144] G. Onida, L. Reining, and A. Rubio, "Electronic excitations: density-functional versus many-body green's-function approaches," Rev. Mod. Phys., vol. 74, 2002. 71

[145] J. Seminario, ed., Recent developments and Applications of Modern Density Functional Theory. Amsterdam: Elsevier, 1996. 74

[146] E. Berger, P. Valáek, and W. Von Der Linden, "Two-dimensional Hubbard-Holstein model," Phys. Rev. B, vol. 52, 1995. 108

[147] G. Giovannetti, M. Casula, P. Werner, F. Mauri, and M. Capone, "Downfolding electron-phonon Hamiltonians from ab initio calculations: Application to K_3 picene," Phys. Rev. B, vol. 90, 2014. 108

[148] O. Madelung, W. von der Osten, and U. Rössler, Landolt-Börnstein. Numerical data and functional relationships in science and technology. New Series. Group III: Crystal and Solid State Physics. Vol. 22: Semiconductors. Subvolume a:Intrinsic Properties of Group IV Elements and III-V, II-VI and I-VII Compounds. Condensed Matter, Springer, 1986. 110

[149] R. Lazzari, N. Vast, J. M. Besson, S. Baroni, and A. Dal Corso, "Structural and vibrational properties of icosahedral B_4C boron carbide," Phys. Rev. Lett., vol. 83, 1999. 110

[150] R. Lazzari, N. Vast, J. Besson, S. Baroni, and A. D. Corso, "Erratum: structural and vibrational properties of icosahedral B_4 boron carbide," Phys. Rev. Lett., vol. 85, 2000. 110

[151] F. Mauri, N. Vast, and C. J. Pickard, "Atomic structure of icosahedral B_4C boron carbide from a *first-principles* analysis of NMR spectra," Phys. Rev. Lett., vol. 87, 2001. 110

[152] N. Vast, "Some *ab initio* studies of the physical properties of materials," HDR thesis, École Polytechnique, Palaiseau, France, 2009. 110

[153] L. He, F. Liu, G. Hautier, M. J. T. Oliveira, M. A. L. Marques, F. D. Vila, J. J. Rehr, G.-M. Rignanese, and A. Zhou, "Accuracy of generalized gradient approximation functionals for density-functional perturbation theory calculations," Phys. Rev. B, vol. 89, 2014. 119

Titre: Etude théorique des états électroniques à plusieurs corps des défauts dans le diamant : le cas du centre NV sous haute pression

Mots clés: Defauts ponctuels; Diamant, centre N V, Theorie de la fonctionnelle de la densite, Theorie des groups, Modele d'Hubbard, Magnetometrie, Pression hydrostatique

Résumé:
Ce travail de doctorat a pour objet l'étude, dans le diamant, de l'influence de la pression sur les transitions optiques entres l'état fondamental et les états excités du centre azote-lacune de carbone NV, sans paramètre ajustable. Le centre neutre NV^0 et le centre chargé négativement NV^- ont chacun été étudiés.
Le centre NV est un défaut à niveaux profonds, ses propriétés optiques et magnétiques sont liées aux niveaux sans dispersion dans la bande interdite électronique associés à des états électroniques fortement correllés et localisés. C'est pourquoi un traitement rigoureux, à l'échelle quantique, est nécessaire. La DFT est une approche puissante pour les calculs des propriétés de l'état fondamental des défauts ponctuels. Cependant, les états électroniques en DFT ont un caractère mono-déterminantal. La DFT seule ne permet pas de calculer certains états électroniques à N- corps qui caractérisent les défauts profonds. De plus, les fonctionnelles d'échange et corrélation (FXC) utilisées en DFT ont une précision limitée.
C'est pourquoi j'ai d'abord développé une approche combinée modèle d'Hubbard + DFT, où les valeurs des interactions dans le modèle d'Hubbard sont obtenues par une méthode de calcul à partir des principes premiers. La diagonalisation exacte soit, en termes de chimie quantique, le calcul d'interaction de configurations, du Hamiltonian de Hubbard dans la base à plusieurs électrons, construite à partir des niveaux localisé dans la bande interdite, permet d'accéder aux états fondamental et excités multi-configurationels. Cette technique a été comparée aux méthodes récentes de l'état de l'art.
La méthode développée est appliquée à l'étude de l'effet de la pression hydrostatique sur les niveaux triplets et singulets du centre NV^-, et sur les niveaux doublets et quadruplets du centre NV^0. Parmi les nombreux résultats, j'ai découvert un effet très intéressant lié à la transition singulet-singulet sous pression hydrostatique dans le centre NV^-. Les résultats obtenus dans ce travail n'ont jamais été ni calculé ni mesurés expérimentalement.
En perspective, j'ai développé un nouveau code de calcul qui peut être utilisé pour étudier d'autres défauts d'interêt dans les technologies quantiques.

Title: Theoretical study of the many-body electronic states of defects in diamond: the case of the NV center under high pressure

Keywords: Point defects, Diamond, NV center, Density Functional Theory, Hubbard model, Group Theory, Magnetometry, Hydrostatic pressure

Abstract:
The aim of this doctoral thesis is to study the influence of the pressure on the optical transitions between multi-determinant ground state and excited states of the NV center from the first-principles. In this work, I study both the neutral NV^0 and negatively charged NV^- centers.
The NV center is a deep-center defect, its optical and magnetic properties are related with strongly correlated localized levels in the electronic band-gap. Thus, an accurate quantum mechanical treatment is needed. DFT is a powerful approach for the calculation of the ground state properties of defects. However, the single Slater determinant nature of the DFT wave function does not allow for the calculation of some many-body levels. Moreover, exchange and correlation (XC) functionals used in DFT have a limited accuracy.
Therefore, in this PhD work, I first develop a combined DFT + Hubbard model technique, where the interaction parameters of the Hubbard model were calculated from the first-principles.
An exact diagonalization (or in quantum chemistry language full Configuration Interaction calculations) of the Hubbard Hamiltonian in the many-electron basis constructed of in-gap localized levels, allows to get access to multi-determinant ground and excited states. I benchmark this technique comparing it to the recent state of the art methods.
Finally, I apply the developed technique in order to study the effect of the hydrostatic pressure on NV^- and NV^0 centers. Among many results of my work, I discovered a very interesting effect related to the singlet-singlet transition in the NV^- center under hydrostatic pressure.
As a perspective, I developed a new code that can be applied to study other defect systems of interest in the quantum technologies.

Institut Polytechnique de Paris
91120 Palaiseau, France